Scrambling and recovery of quantum information in inhomogeneous quenches in two-dimensional conformal field theories

Kanato Goto,[1,2,3,*] Masahiro Nozaki,[3,4,†] Shinsei Ryu,[1,‡] Kotaro Tamaoka,[5,§] and Mao Tian Tan[6,‖]

[1]*Department of Physics, Princeton University, Princeton, New Jersey 08544, USA*
[2]*Center for Gravitational Physics and Quantum Information (CGPQI), Yukawa Institute for Theoretical Physics, Kyoto University, Kyoto 606-8501, Japan*
[3]*RIKEN Interdisciplinary Theoretical and Mathematical Sciences (iTHEMS), Wako, Saitama 351-0198, Japan*
[4]*Kavli Institute for Theoretical Sciences, University of Chinese Academy of Sciences, Beijing 100190, China*
[5]*Department of Physics, College of Humanities and Sciences, Nihon University, Sakura-josui, Tokyo 156-8550, Japan*
[6]*Asia Pacific Center for Theoretical Physics, Pohang, Gyeongbuk 37673, Korea*

(Received 28 June 2023; accepted 11 December 2023; published 1 April 2024)

We study various quantum quench processes induced by the Möbius/sine-square deformation of the Hamiltonian in two-dimensional conformal field theories starting from the thermofield double state in the two copies of the Hilbert space. These quantum quenches, some of which are directly related to the operator entanglement of the time-evolution operators, allow us to study scrambling and recovery of quantum information. In particular, under the sine-square deformed time evolution, we show from the time dependence of mutual information that the Bell pairs, initially shared by the subsystems of the two Hilbert spaces, may revive even after the mutual information for small subsystems is completely destroyed by quantum information scrambling dynamics. This mutual information is robust against the strong scrambling dynamics. As a consequence, the steady state has a nonlocal correlation shared not by any of two parties but by three parties. In the holographic dual description, a wormhole connecting the two Hilbert spaces may nonlinearly grow with time during the quantum quenches. We also propose effective pictures that describe the dynamics of mutual information during the time evolution by inhomogeneous Hamiltonians.

DOI: 10.1103/PhysRevResearch.6.023001

I. INTRODUCTION AND SUMMARY

Nonequilibrium dynamics in quantum many-body systems is a subject of intense research. One of the recurrent themes is how quantum entanglement is generated and propagates during nonequilibrium processes. It has been shown that complex ("chaotic") quantum many-body systems can scramble quantum information nonlocally. Quantum information scrambling entails the loss of the information of initial states at least locally and results in thermalization [1–5]. Experimental techniques to measure scrambling in laboratories have rapidly been developed in the past few years (e.g., [6–19]).

Nonequilibrium dynamics in the context of $(1+1)$-dimensional conformal field theory (CFT) have been widely studied in recent years [5,20–28]. In particular, recent studies constructed a series of solvable models of quantum quench and Floquet dynamics in $(1+1)$-dimensional CFT using a class of inhomogeneous Hamiltonians. These works provide rare examples where the dynamics of interacting many-body quantum systems can be solved exactly. The inhomogeneous Hamiltonians used in these studies include, in particular, the so-called sine-square deformation (SSD) and Möbius deformation of $(1+1)$-dimensional quantum many-body systems. In these deformations, evolution operators are given as a linear superposition of three Virasoro generators (L_0, $L_{\pm 1}$), which form an $sl(2,\mathbb{R})$ subalgebra of the Virasoro algebra. Not only being exactly solvable, these quantum quench and Floquet dynamics exhibit rich behaviors, such as dynamical "phase transitions" that separate heating and nonheating behaviors during time evolution [29–43]. For additional discussions on spatial inhomogeneity in nonequilibrium setting, see Refs. [44,45].

Reference [31] studied quantum quench problems in 2d CFT using these inhomogeneous Hamiltonians starting from the Gibbs state as an initial state. One of the main findings of Ref. [31] is that the time evolution generates an inhomogenous temperature profile. In particular, when the inhomogeneous postquench Hamiltonian is the SSD Hamiltonian, it heats up a spatial subregion near the point where the Hamiltonian density vanishes, while it cools down the rest of the system. (The idea of using inhomogeneous Hamiltonians to prepare low-temperature states has been

*kanato.goto@yukawa.kyoto-u.ac.jp
†mnozaki@ucas.ac.cn
‡shinseir@princeton.edu
§tamaoka.kotaro@nihon-u.ac.jp
‖maotian.tan@apctp.org

explored also outside the Möbius/sine-square deformation—see, for example, [46–51].) This heating process results in a local excitation that carries the (almost) entire entropy of the system, which we call a black-hole-like excitation (B.H.-like excitation). On the other hand, for the cooled region, nonlocal quantum correlations emerge under the inhomogeneous time evolution. The SSD Hamiltonian can thus be used to "simulate" the formation of a black hole.

In this paper, we further study inhomogeneous deformations of the CFT Hamiltonian and the associated nonequilibrium dynamics. To be concrete, we will discuss three setups presented in Sec. II. All these processes are quantum quenches starting from the thermofield double (TFD) state defined on two copies of the Hilbert space, $\mathcal{H}_1$ and $\mathcal{H}_2$.

There are three motivations for studying these setups (roughly one for each setup). First, in the previous papers almost all properties discussed (cooling/heating, the formation of B.H.-like excitations) are universal in the sense that they depend only on conformal symmetry. Little is known about the effects of the inhomogeneous deformations on the details of theories and quantum information scrambling [52]. Different CFTs can exhibit different kinds of dynamics, e.g., integrable, chaotic, or something in between. For these dynamics, effective descriptions of dynamics have been developed, namely the quasiparticle picture for integrable dynamics and the membrane picture (line-tension picture) for chaotic and holographic dynamics. As discussed in [53,54], quantum information scrambling can be detected by studying operator entanglement. In particular, the operator entanglement for undeformed CFT time-evolution operators was previously discussed in [54]. In this paper, we study the effect of the inhomogeneous temperature profile and B.H.-like excitations on quantum information scrambling. In the quantum quench setups starting from the TFD state, we will study bipartite and tripartite mutual information between subsystems in $\mathcal{H}_1$ and $\mathcal{H}_2$, which measures operator entanglement in disguise.

Second, by considering two-step time-evolution operators, we discuss the recovery of quantum information. In the past decades, information retrieval from a black hole has received considerable attention [15,55–57]. In the setups considered in these papers, quantum information is thrown into a black hole, scrambled in its interior, and then emitted as the Hawking radiation. These papers investigated efficient ways of retrieving the quantum state from the emitted Hawking radiations. Investigating the information retrieval from typical states, i.e., states in which information is scrambled, should lead to a deep understanding of quantum thermalization and black hole dynamics. Our setups using inhomogeneous time-evolution operators in 2d CFT that are rather different from those considered in the above papers, where quantum information theoretical models were considered. Nevertheless, we will demonstrate the recovery of quantum information in our setups: If we start from the TFD state or a typical state and then evolve the system with the SSD Hamiltonian acting on the single Hilbert space, then the mutual information between the subsystems on the different Hilbert spaces, $\mathcal{H}_1$ and $\mathcal{H}_2$, locally returns to its initial value. (Here, in our setups, the time-evolution operator acts solely on $\mathcal{H}_1$.) From this mutual information recovery, we can see the Bell pairs initially shared by the subsystems of $\mathcal{H}_1$ and $\mathcal{H}_2$ may be revived during the SSD time evolution. This recovered correlation may be robust against the scrambling effect of 2d holographic CFTs. Furthermore, under the evolution induced by the uniform holographic Hamiltonian, when the subsystems do not include the so-called fixed points, the system can develop a genuine tripartite correlation, i.e., a nonlocal correlation shared by three parties, but not by two parties only.

Finally, we are also interested in the dynamics of B.H.-like excitations. In Setup 3 presented in Sec. II, we once again consider two-step time evolution where the first step creates a pair of B.H.-like excitations while the second step induces nontrivial dynamics thereof.

We back up the above analyses for the specific setups by developing an effective description of the entanglement dynamics. In particular, we develop the line-tension picture for inhomogeneous time evolution. We also develop the holographic bulk description of these inhomogeneous quenches by keeping track of the spatiotemporal deformations of the bulk black hole horizon. Finally, we also discuss the wormhole connecting the two Hilbert spaces. Due to the nontrivial dynamics of the B.H.-like excitations, the size of the wormhole exhibits an oscillatory growth.

The results are quite remarkable and may pave the way for important developments in the simulation of quantum dynamics in near-term quantum simulators and quantum computers. To make it easier for the reader to grasp our findings in this study, let us mention four salient points:

(1) As detailed in Sec. IV, we found that during the SSD time evolution, the bipartite mutual information exhibits the recovery of the nonlocal correlations. This suggests that SSD unitary time evolution can be used as a unitary process, which recovers the nonlocal correlations of a system.

(2) In Sec. V, the system first undergoes time evolution with the SSD Hamiltonian before undergoing a subsequent time evolution with the maximally scrambling uniform holographic CFT Hamiltonian. The black hole-like excitations in the atypical state prepared by the initial SSD Hamiltonian is stable under the subsequent uniform holographic CFT Hamiltonian evolution, which suggests that the SSD Hamiltonian can be used to prepare atypical quantum states that have features that are robust against maximally scrambling dynamics. See Sec. V for more details.

(3) The production of genuine tripartite mutual information from an inhomogeneous quench of the holographic CFTs is, to the best of our knowledge, an example of the conversion of bipartite entanglement to tripartite entanglement in a field theory or a many-body system. This is explained in Sec. V B.

(4) By subsequently evolving the system with the uniform Hamiltonian after an initial SSD time evolution, these black hole-like excitations can be moved around the system, opening up the possibility of simulating the dynamics of black holes in actual experiments. This is explained in Sec. V.

The rest of the paper is organized as follows: In Sec. II, we will describe the inhomogeneously deformed Hamiltonians in 2d CFT, the three setups considered in this paper, and the measures of entanglement of our interest. In Secs. III and IV, we will present the time dependence of mutual information under the evolution by the inhomogeneous Hamiltonians, starting from the thermofield double and typical states. In the following three sections, we report the time dependence of

the entanglement measures in the three setups: In Sec. V, we will report the time dependence of entanglement entropy and mutual information when we start from the thermofield double state, evolve the system with the SSD Hamiltonian, and then subsequently evolve it with the uniform Hamiltonian. In Sec. VI, we will propose an effective model that describes the operator entanglement hydrodynamics of the Möbius/SSD time-evolution operators. In Sec. VII, we will report the dual geometries of the systems considered in this paper, and also present the growth of wormholes. Finally, in Sec. IX, we will discuss the possible applications of our results to experiments, and comment on a few future directions.

II. PRELIMINARIES

In this section, we describe the inhomogeneously deformed Hamiltonian, the setups of our interest, and the measures of entanglement considered in this paper.

A. Inhomogeneously deformed Hamiltonians

Inhomogeneously deformed Hamiltonians considered in this paper are defined by modulating the Hamiltonian density. Let us start from a homogeneous Hamiltonian $H_0 = \int_0^L h(x)dx$ defined on a one-dimensional circle of circumference L, i.e., the periodic spatial boundary condition is imposed. The integrand of the homogeneous Hamiltonian $h(x)$ is the Hamiltonian density. An inhomogeneous deformation of H_0 can be introduced as

$$H_{\rm Inho} = \int_0^L dx\, f(x)h(x), \tag{1}$$

where $f(x)$ is an envelope function. The envelope functions considered in this paper are

$$\begin{aligned} f_{\rm Möbius}(x) &= 1 - \tanh 2\theta \cos\left(\frac{2\pi x}{L}\right), \\ f_{\rm SSD}(x) &= 2\sin^2\left(\frac{\pi x}{L}\right), \\ f_{\rm CSD}(x) &= 2\cos^2\left(\frac{\pi x}{L}\right). \end{aligned} \tag{2}$$

Here, $f_{\rm Möbius}(x)$ reduces to $f_{\rm SSD}(x)$ and $f_{\rm CSD}(x)$ in the $\theta \to \pm\infty$ limits respectively. The inhomogeneously deformed Hamiltonians with the envelope functions $f(x) = f_{\rm Möbius}(x)$, $f_{\rm SSD}(x)$, $f_{\rm CSD}(x)$ are called Möbius, sine-square (SS) and cosine-square (CS) deformed Hamiltonians, respectively.

The SSD Hamiltonian was originally proposed as a simple way of removing the boundary effect in finite-size systems [58–66]. Subsequently, the SSD in 2d CFTs and its one-parameter deformation (Möbius deformation) were also discussed [67–72]. Recently, these deformations have been used to study thermalization and nonthermalization [29–31,41,42] and Floquet dynamics [32–40].

In these deformations, we naturally identify two special locations on the spatial circle, $x = 0 \equiv X_f^1$ and $x = L/2 \equiv X_f^2$. Being the minimum or maximum of the envelope functions, we expect the effect of the envelope functions on quantum dynamics is most significant around these points. We will soon show that these points play special roles under the inhomogeneous time evolution by looking at various quantities such as the Heisenberg time evolution of operators.

For the bulk of the paper, we mainly focus on the Möbius and SS deformations. The details of the analysis and calculations of the entanglement dynamics under the CSD time evolution are presented in Appendix C.

B. The systems evolved with the inhomogeneously deformed Hamiltonians

We consider the following three setups in this paper. In all setups, we consider the thermofield double (TFD) state

$$|{\rm TFD}\rangle = \mathcal{N} e^{-\frac{\epsilon(H_0^1+H_0^2)}{2}} \sum_a |a\rangle_1 \otimes |a\rangle_2, \tag{3}$$

as our initial state of time evolution. Here, the TFD state is defined in the doubled Hilbert space, $\mathcal{H} = \mathcal{H}_1 \otimes \mathcal{H}_2$, and $H_0^{i=1,2}$ and $|a\rangle_{i=1,2}$ denote the undeformed 2d CFT Hamiltonian, and its eigenstates respectively. The regulator ϵ is half of the inverse temperature, $\epsilon = \beta/2$. The square of the normalization factor $\mathcal{N}$ guarantees that $\langle {\rm TFD}|{\rm TFD}\rangle = 1$. We will mainly work with holographic CFTs, i.e., CFTs that admit holographic dual descriptions. However, we also study the 2d free fermion CFT as a representative of nonchaotic (integrable) CFTs and make comparisons between the two. The TFD state was previously used as a "convenient" initial condition in quantum quench problems [48]. The TFD state is a short-range entangled state, and can be considered as a ground state of a gapped Hamiltonian [73,74]. Our setups above are hence in a similar spirit to the seminal work by Calabrese and Cardy on quantum quench in 2d CFTs [5,20].

Setup 1. In the first setup, starting from the TFD state we consider the time evolution under the unitary operator $U_{\rm Möbius/SSD} = e^{-it_1 H^1_{\rm Möbius/SSD}} \otimes \mathbf{1}_2$, where $H^1_{\rm Möbius/SSD}$ and $\mathbf{1}_2$ denote the Möbius/SS deformed Hamiltonian acting on $\mathcal{H}_1$, and identity operator on $\mathcal{H}_2$, respectively. The evolved state is

$$|\Psi_1(t_1)\rangle = \left(e^{-it_1 H^1_{\rm Möbius/SSD}} \otimes \mathbf{1}_2\right)|{\rm TFD}\rangle. \tag{4}$$

Setup 2. In the second setup, we once again start from the TFD state, and then consider the two-step time-evolution first by $e^{-it_0 H_0}$ and then $e^{-it_1 H_{\rm Möbius/SSD}}$, both acting on $\mathcal{H}_1$,

$$|\Psi_2(t_1,t_0)\rangle = \left(e^{-iH^1_{\rm SSD}t_1} \otimes \mathbf{1}_2\right)\left(e^{-iH^1_0 t_0} \otimes \mathbf{1}_2\right)|{\rm TFD}\rangle. \tag{5}$$

Here, the first time evolution can be interpreted as creating an excited state, which is then time evolved during the second step of the time evolution.

Setup 3. Finally, in the third setup, we exchange the ordering of the two time-evolution operators in Setup 2, and consider

$$|\Psi_3(t_1,t_0)\rangle = \left(e^{-iH^1_0 t_0} \otimes \mathbf{1}_2\right)\left(e^{-iH^1_{\rm SSD}t_1} \otimes \mathbf{1}_2\right)|{\rm TFD}\rangle. \tag{6}$$

Let us now elaborate on the motivations for studying these setups and provide an overview of our results.

We first note that, in addition to the interpretation as quantum quench, we can give an interpretation of these states (and entanglement measures for these states) from the perspective of operator entanglement. Consider, for a unitary time-evolution operator $U_{\rm unitary}$, an effective unitary time-evolution operator $U_{\rm effective} = U_{\rm unitary} e^{-\epsilon H_0}$. By using the

channel-state map [53,75], define the dual state of $U_{\text{effective}}$ as the state on the doubled Hilbert space, $\mathcal{H}_1 \otimes \mathcal{H}_2$,

$$|U_{\text{effective}}\rangle = \mathcal{N} \sum_a U_{\text{unitary}} e^{-\frac{\xi}{2}(H^1+H^2)} |a\rangle_1 \otimes |a^*\rangle_2, \tag{7}$$

where $|\cdot^*\rangle$ is CPT conjugate of $|\cdot\rangle$, and $|a\rangle_i$ is an eigenstate of H_i [76] The definition of dual state is not unique. The unitary time-evolution operator acts only on $\mathcal{H}_1$. The dynamical properties of $U_{\text{effective}}$ are represented as the entanglement structure of the dual state. Thus, the above states can be interpreted as the dual states of the effective unitary time-evolution operators. In particular, by considering the state (4) and its entanglement structure, we can discuss the operator entanglement of the Möbius/SS deformed time-evolution operator and the effect of the inhomogeneous deformation on quantum information scrambling. For the case of regular, homogeneous Hamiltonian H_0 of 2d CFTs, the operator entanglement and quantum information scrambling were studied in [54].

In Setup 2 and 3, we have two-step time evolution operators. In Setup 2, the first time evolution under H_0 is expected to scramble quantum information (for holographic CFTs). Our interest here is the effect of the second time evolution on the scrambled information. As we will see, the SSD evolution recovers the nonlocal correlation between subsystems A and B in $\mathcal{H}_1$ and $\mathcal{H}_2$ when the subsystem A includes X_f^1. Namely, by the SSD evolution, we can retrieve the information from the typical state, the state where the information is fully scrambled. The motivation for Setup 2 is thus in line with information retrieval from a black hole [15,55–57]. In these papers, quantum information is first thrown into a black hole, scrambled in its interior, and then emitted as Hawking radiation. They investigated efficient ways of retrieving the quantum state from the emitted Hawking radiations.

In Setup 3, the first part of the two-step time evolution (with the SSD Hamiltonian on $\mathcal{H}_1$) can be interpreted as preparing a pair of black-hole-like excitations (B.H.-like excitations) [31]. The created B.H.-like excitations are then subject to the second step of the time evolution under the regular Hamiltonian H_0^1. Setup 3 can thus be used to study the dynamics of the B.H.-like excitations. As we will show, the second time evolution induces an interesting dynamics of the B.H.-like excitations that can be detected by monitoring various entanglement measures. Also, the wormhole growth measured by the geodesic length is described by the propagation of the B.H.-like excitations. From this perspective, it would also be interesting to consider a similar time evolution,

$$|\Phi(t_1,t_2)\rangle = \left(e^{-iH^1_{\text{CSD}}t_2} \otimes \mathbf{1}_2\right)\left(e^{-iH^1_{\text{SSD}}t_1} \otimes \mathbf{1}_2\right)|\text{TFD}\rangle. \tag{8}$$

Here, the first step of the time evolution is the same and still creates a pair of B.H.-like excitations. The second time evolution is, however, given by H_{CSD}, instead of H_0, whose envelope function profile is complimentary to H_{SSD}. The details of the entanglement dynamics for (8) are presented in Appendix C.

C. Entanglement entropies, and the twist operator formalism

1. Entanglement entropies, bipartite, and tripartite mutual information

The main quantities of interest in this paper are entanglement entropies for various subsystems as well as the bipartite and tripartite mutual information (BMI and TMI, respectively). Below, we consider a subsystem (sub-Hilbert space) of $\mathcal{H}_2$, which we call A. Similarly, we consider a sub-Hilbert space B of $\mathcal{H}_1$. When discussing TMI, we consider two subsystems of $\mathcal{H}_2$, denoted as B_1 and B_2. More specifically, subsystem A is a spatial interval with its left and right ends located at X_1 and X_2, and, similarly, B is an interval with its left and right ends located at Y_1 and Y_2. Here, $0 < X_2 < X_1$ and $0 < Y_2 < Y_1$. (B_1 and B_2 are also intervals—their geometries are specified in the following.) Starting from the total density matrix $|\Psi\rangle\langle\Psi|$, we consider the reduced density matrix $\rho_{\mathcal{V}}$ ($\mathcal{V} = A, B, A \cup B, \cdots$), and the corresponding von Neumann and/or Rényi entropies. They are denoted by $S_{\mathcal{V}}$ and $S_{\mathcal{V}}^{(n)}$, respectively.

Bipartite mutual information (BMI) for A and B is defined as the linear combination of the entanglement entropies,

$$I_{A,B} = S_A + S_B - S_{A\cup B}. \tag{9}$$

We note that $I_{A,B}$ is independent of the lattice spacing. Since the universal pieces of entanglement entropies cancel out, $I_{A,B}$ depends on only the nonuniversal pieces of these entropies.

To define tripartite mutual information (TMI) we consider three subsystems A, B_1, and B_2. Then, the TMI for A, B_1, and B_2 is defined as a linear combination of BMI,

$$I_{A,B_1,B_2} = I_{A,B_1} + I_{A,B_2} - I_{A,B_1\cup B_2}. \tag{10}$$

As in [53,54,77–83], the TMI for operator entanglement can be a measure of scrambling. The time dependence of TMI may detect how the Bell pairs initially shared by A and $\mathcal{H}_1$ are delocalized and become nonlocally hidden in $\mathcal{H}_1$ under the time evolution.

2. Parameter regimes of interest

For the bulk of the paper, we are interested in the above entanglement quantities in the coarse-grained regime. This regime is defined as follows. Let $\hat{\mathcal{V}}$ denote the subsystem consisting of the spatial intervals, and then let $\hat{L}$, $\hat{l}_{\mathcal{V}}$, $\hat{a}$, $\hat{\epsilon}$, and $\hat{t}$ denote a system size, a subsystem size, a lattice spacing, a regularization parameter that guarantees the norm of states considered in this paper is one, and the times associated to some Hamiltonian considered. Here, $\hat{*}$ denotes a dimensionful parameter, and $*$ is the dimensionless one defined as $\frac{\hat{*}}{\hat{a}}$. In the following, we will use only dimensionless parameters. The parameter region considered is

$$L \gg l_{\mathcal{V}}, \quad t \gg \epsilon \gg 1. \tag{11}$$

The interest in this regime comes from the expectation that in this regime we can potentially use effective descriptions of entropy propagation such as the quasiparticle picture or the line-tension (membrane) picture.

D. Path integral formulation and twist operators

To develop the path-integral formalism, let us define Euclidean density operators as

$$\rho_E = \mathcal{N}_E^2 \sum_{a,b} e^{-\epsilon(E_a+E_b)} \big(U_E^1 |a\rangle\langle b|_1 \tilde{U}_E^1 \otimes |a^*\rangle\langle b^*|_2\big), \quad (12)$$

where $\mathcal{N}_E^{-2} = \mathrm{tr} e^{-2\epsilon H_0}$ guarantees that $\mathrm{tr}\rho_E = 1$. These density operators may be obtained from the ones defined in Sec. II B by analytically continuing to imaginary time. Here, the Euclidean evolution operator is given, depending on the setups above,

$$U_E^1 = \begin{cases} e^{-H^1_{\text{Möbius}}\tau_1} \\ e^{-H^1_{\text{SSD}}\tau_1} e^{-H^1_0\tau_0}, \\ e^{-H^1_0\tau_0} e^{-H^1_{\text{SSD}}\tau_1} \end{cases} \quad \tilde{U}_E^1 = \begin{cases} e^{H^1_{\text{Möbius}}\tau_1} \\ e^{H^1_0\tau_0} e^{H^1_{\text{SSD}}\tau_1}. \\ e^{H^1_{\text{SSD}}\tau_1} e^{H^1_0\tau_0} \end{cases} \quad (13)$$

We now define the reduced Euclidean density operators for $\mathcal{V}$ as $\rho_{E,\mathcal{V}} = \mathrm{tr}_{\overline{\mathcal{V}}}\rho_E$. They are given explicitly as

$$\rho_{E,\mathcal{V}} = \begin{cases} \mathcal{N}_E^2 \,\mathrm{tr}_{\bar{A}}(e^{-2\epsilon H_0}) & \mathcal{V} = A, \\ \mathcal{N}_E^2 \,\mathrm{tr}_{\bar{B}}\big(U_E^1 e^{-2\epsilon H_0}\tilde{U}_E^1\big) & \mathcal{V} = B, \\ \mathcal{N}_E^2 \sum_{a,b} e^{-\epsilon(E_a+E_b)} \mathrm{tr}_{\bar{B}}\big(U_E^1|a\rangle\langle b|_1\tilde{U}_E^1\big) \otimes \mathrm{tr}_{\bar{A}}(|a^*\rangle\langle b^*|_2) & \mathcal{V} = A\cup B, \end{cases} \quad (14)$$

where $\bar{A}$ denotes the complement of A. Let us define Euclidean entanglement entropy associated with $\rho_{E,\mathcal{V}}$ as von Neumann entropy for this reduced density matrix,

$$S_{E,\mathcal{V}} = -\mathrm{tr}_{\mathcal{V}}(\rho_{E,\mathcal{V}}\log\rho_{E,\mathcal{V}}) = \lim_{n\to 1}\tfrac{1}{1-n}\log \mathrm{tr}_{\mathcal{V}}(\rho_{E,\mathcal{V}})^n. \quad (15)$$

Thus, in the von Neumann limit $n \to 1$, the nth Rényi entropy, $S^{(n)}_{E,\mathcal{V}} = \frac{1}{1-n}\log \mathrm{tr}_{\mathcal{V}}(\rho_{E,\mathcal{V}})^n$, reduces to the Euclidean entanglement entropy. In the path-integral formalism, $S^{(n)}_{E,\mathcal{V}}$ is given by $S^{(n)}_{E,\mathcal{V}} = \frac{1}{1-n}\log\frac{Z_n}{Z_1^n}$, where Z_n is the partition function on an n-sheeted geometry defined by sewing $\mathcal{V}$ together in a cyclic fashion as in [84,85]. At the end of the calculations, we analytically continue $\tau_{i=0,1,2}$ to $it_{i=0,1,2}$ to obtain the time evolution of entanglement entropies. With this procedure in mind, from now on, we drop the subscript "E" and simply write $S_{E,\mathcal{V}} \to S_{\mathcal{V}}$.

To compute $S_{\mathcal{V}}$, let us now employ the twist-operator formalism where $\mathrm{tr}_{\mathcal{V}}(\rho_{\mathcal{V}})^n$ is given by the $2m_{\mathcal{V}}$-point functions arising from insertion of the twist and antitwist operators on the torus. Here, $\mathcal{V}$ is composed of $m_{\mathcal{V}}$ intervals. Consequently, the Rényi entropies can be expressed as

$$\begin{aligned} S_A^{(n)} &= \frac{1}{1-n}\log\big\{\langle\overline{\sigma}_n(w_{X_1},\overline{w}_{X_1})\sigma_n(w_{X_2},\overline{w}_{X_2})\rangle_{2\epsilon}\big\}, \\ S_B^{(n)} &= \frac{1}{1-n}\log\big\{\mathcal{N}_E^2\,\mathrm{tr}\big[\tilde{U}_E^1\,\sigma_n(w_{Y_1},\overline{w}_{Y_1}) \\ &\quad\times\overline{\sigma}_n(w_{Y_2},\overline{w}_{Y_2})U_E^1\,e^{-2\epsilon H_0}\big]\big\}, \\ S_{A\cup B}^{(n)} &= \frac{1}{1-n}\log\big\{\mathcal{N}_E^2\,\mathrm{tr}\big[e^{-\epsilon H_0}\,\tilde{U}_E^1\,\sigma_n(w_{Y_1},\overline{w}_{Y_1})\overline{\sigma}_n(w_{Y_2},\overline{w}_{Y_2}) \\ &\quad\times U_E^1\,e^{-\epsilon H_0}\,\overline{\sigma}_n(w_{X_1},\overline{w}_{X_1})\sigma_n(w_{X_2},\overline{w}_{X_2})\big]\big\}, \end{aligned} \quad (16)$$

where $\langle\cdot\rangle_{2\epsilon}$ denotes the expectation value on the thermal torus where thermal and spatial circumstances are 2ϵ and L, respectively. The complex coordinate is defined as $(w_x, \overline{w}_x) = (ix, -ix)$, and $h_n = \frac{c(n^2-1)}{24n}$ denotes the conformal dimension of twist and antitwist operators. By using the identities, $\tilde{U}_E^1 U_E^1 = U_E^1\tilde{U}_E^1 = \mathbf{1}$ and $e^{-\epsilon H_0}e^{\epsilon H_0} = e^{\epsilon H_0}e^{-\epsilon H_0} = \mathbf{1}$, we can rewrite $2m_{\mathcal{V}}$-point functions in (16) as the ones in Heisenberg picture. In the Heisenberg picture, the evolution of the twist and antitwist operators in Euclidean time is given by

$$e^{\epsilon H_0}\,\tilde{U}_E^1\,\sigma_n(w_x,\overline{w}_x)\,U_E^1\,e^{-\epsilon H_0} = \left|\frac{dw^{\text{New}}_{x,\epsilon}}{dw_x}\right|^{2h_n}\sigma_n\big(w^{\text{New}}_{x,\epsilon},\overline{w}^{\text{New}}_{x,\epsilon}\big). \quad (17)$$

Some details of $w^{\text{New}}_{x,\epsilon}$ and $\overline{w}^{\text{New}}_{x,\epsilon}$ are presented in Appendix A. During the evolution by $U_E^1 e^{-\epsilon H_0}$, the location of the operators is mapped to $w^{\text{New}}_{x,\epsilon}$, $\overline{w}^{\text{New}}_{x,\epsilon}$. As a consequence, $S^{(n)}_{\mathcal{V}}$ is written as

$$\begin{aligned} S_A^{(n)} &= \frac{1}{1-n}\log\big[\langle\overline{\sigma}_n(w_{X_1},\overline{w}_{X_1})\sigma_n(w_{X_2},\overline{w}_{X_2})\rangle_{2\epsilon}\big], \\ S_B^{(n)} &= \frac{1}{1-n}\log\left[\Pi_{i=1,2}\left|\frac{dw^{\text{New}}_{Y_i,\epsilon}}{dw_{Y_i}}\right|^{2h_n}\right] \\ &\quad+\frac{1}{1-n}\log\langle\sigma_n(w^{\text{New}}_{Y_1,\epsilon},\overline{w}^{\text{New}}_{Y_1,\epsilon})\overline{\sigma}_n(w^{\text{New}}_{Y_2,\epsilon},\overline{w}^{\text{New}}_{Y_2,\epsilon})\rangle_{2\epsilon}, \\ S_{A\cup B}^{(n)} &= \frac{1}{1-n}\log\left[\Pi_{i=1,2}\left|\frac{dw^{\text{New}}_{Y_i,\epsilon}}{dw_{Y_i}}\right|^{2h_n}\right] \\ &\quad+\frac{1}{1-n}\log\langle\sigma_n(w^{\text{New}}_{Y_1,\epsilon},\overline{w}^{\text{New}}_{Y_1,\epsilon})\overline{\sigma}_n(w^{\text{New}}_{Y_2,\epsilon},\overline{w}^{\text{New}}_{Y_2,\epsilon}) \\ &\quad\times\overline{\sigma}_n(w_{X_1},\overline{w}_{X_1})\sigma_n(w_{X_2},\overline{w}_{X_2})\rangle_{2\epsilon}. \end{aligned} \quad (18)$$

We note that $|\frac{dw^{\text{New}}_{x,\epsilon}}{dw_{x,\epsilon}}|^{2h_n}$ is independent of the details of 2d CFTs. We hence call this factor the universal piece. On the other hand, the two- and four-point functions of the twist fields on the torus depend on the details of 2d CFTs, and we call them the nonuniversal pieces. These variables, $w^{\text{New}}_{x,\epsilon}$ and $\overline{w}^{\text{New}}_{x,\epsilon}$, depend on the imaginary times $\tau_{i=0,1,2}$. After we analytically continue $\tau_{i=0,1,2}$ to $it_{i=0,1,2}$, only these imaginary parts of $w^{\text{New}}_{x,\epsilon}$ and $\overline{w}^{\text{New}}_{x,\epsilon}$ depend on these real times. In other words, during the evolution by $U_E^1 e^{-\epsilon H_0}$, the twist and antitwist operators spatially move with time as in Appendix A 1. Under the evolution by $H_{\text{SSD/CSD}}$, the primary operators at $x = X_1^f = 0$ or $x = X_2^f = \frac{L}{2}$ does not spatially move. We call X_1^f and X_2^f fixed points.

1. Nonuniversal pieces in 2d holographic CFTs

Let us have a closer look at the nonuniversal pieces of the entanglement entropy for the single and double intervals in 2d holographic CFTs. To compare the results on 2d holographic CFTs with the ones in the 2d free fermion CFT, we also calculated the nonuniversal pieces in the free fermion CFT. The results and calculations for the free fermion CFT are reported in Appendix D 1.

Single interval. Here, we present the nonuniversal piece of entanglement entropy for the single interval in the coarse-grained regime. In this regime, the gravity dual of the system on the torus is the BTZ black hole [86]. Therefore, in the von Neumann limit when $n \to 1$, the nonuniversal piece is given by the geodesic length in the BTZ black hole [87,88]. Let $\mathcal{V}$ denote the subsystem, and also v_1 and v_2 denote the endpoints of $\mathcal{V}$. Here, we assume that $v_1 > v_2 > 0$. The nonuniversal piece of entanglement entropy for the reduced density matrix associated with $\mathcal{V}$ is holographically given by

$$\lim_{n\to 1}\frac{1}{1-n}\log\left\langle\sigma_n\left(w^{\rm New}_{v_1,\epsilon},\overline{w}^{\rm New}_{v_1,\epsilon}\right)\overline{\sigma}_n\left(w^{\rm New}_{v_2,\epsilon},\overline{w}^{\rm New}_{v_2,\epsilon}\right)\right\rangle_{2\epsilon}$$
$$\approx\frac{c}{3}\log\left(\frac{2\epsilon}{\pi}\right)+\begin{cases}\mathrm{Min}\left[\frac{c}{6}\log\left|\sin\left(\frac{\pi}{2\epsilon}\left(w^{\rm New}_{v_1,\epsilon}-w^{\rm New}_{v_2,\epsilon}\pm iL\right)\right)\right|^2,\ \frac{c}{6}\log\left|\sin\left(\frac{\pi}{2\epsilon}\left(w^{\rm New}_{v_1,\epsilon}-w^{\rm New}_{v_2,\epsilon}\right)\right)\right|^2+\frac{c\pi L}{6\epsilon}\right] & \text{if } x=X^1_f\in\mathcal{V}\\ \mathrm{Min}\left[\frac{c}{6}\log\left|\sin\left(\frac{\pi}{2\epsilon}\left(w^{\rm New}_{v_1,\epsilon}-w^{\rm New}_{v_2,\epsilon}\pm iL\right)\right)\right|^2+\frac{c\pi L}{6\epsilon},\ \frac{c}{6}\log\left|\sin\left(\frac{\pi}{2\epsilon}\left(w^{\rm New}_{v_1,\epsilon}-w^{\rm New}_{v_2,\epsilon}\right)\right)\right|^2\right] & \text{if } x=X^1_f\notin\mathcal{V}\end{cases}. \tag{19}$$

Double intervals. Let us turn to the nonuniversal piece of the entanglement entropy for a union of double intervals. In 2d holographic CFTs, the nonuniversal piece for a pair of intervals is given by

$$\lim_{n\to 1}\frac{1}{1-n}\log\left\langle\sigma_n\left(w^{\rm New}_{Y_1,\epsilon},\overline{w}^{\rm New}_{Y_1,\epsilon}\right)\overline{\sigma}_n\left(w^{\rm New}_{Y_2,\epsilon},\overline{w}^{\rm New}_{Y_2,\epsilon}\right)\right.$$
$$\left.\times\,\overline{\sigma}_n\left(w_{X_1},\overline{w}_{X_1}\right)\sigma_n\left(w_{X_2},\overline{w}_{X_2}\right)\right\rangle_{2\epsilon}$$
$$\approx\frac{2c}{3}\log\left(\frac{2\epsilon}{\pi}\right)+\mathrm{Min}[S_{\rm dis},S_{\rm con}], \tag{20}$$

where $S_{\rm dis}$ is determined by the length of geodesic that connects the endpoints of intervals at the same Euclidean time slices, while $S_{\rm con}$ is determined by that of geodesics connecting points on different Euclidean time slices. Some details of $S_{\rm dis}$ and $S_{\rm con}$ are reported in Appendix B 1. The Euclidean temporal and spatial locations, $\tau^{\rm New}_{x,\epsilon}$ and $X^{\rm New}_{x,\epsilon}$, of endpoints are defined as

$$\tau^{\rm New}_{x,\epsilon}=\frac{w^{\rm New}_{x,\epsilon}+\overline{w}^{\rm New}_{x,\epsilon}}{2},\quad X^{\rm New}_{x,\epsilon}=\frac{w^{\rm New}_{x,\epsilon}-\overline{w}^{\rm New}_{x,\epsilon}}{2i}. \tag{21}$$

III. SETUP 1

Let us now turn to the analysis of the time dependence of BMI and TMI in Setup 1, (4). One of the main findings is Fig. 2 (see below) where we plot BMI as a function of time for various choices of θ. This plot should be compared with, e.g., Fig. 11 in Ref. [54] where BMI (or bipartite operator mutual information) of the regular, homogeneous time-evolution operator for holographic CFTs was studied. Interestingly, we find a threshold value of θ that separates the two types of behaviors of BMI presented in the left and right panels of Fig. 2 (see below), respectively. We also compare holographic CFTs and the free fermion CFT described by the quasiparticle picture.

A. Analysis of the geodesic length

We first discuss the time dependence of geodesics corresponding to the nonuniversal pieces of S_A, S_B, and $S_{A\cup B}$ in the Heisenberg picture. For simplicity, let us suppose that the center of B is at $x = X^f_1$. The twist and antitwist operators associated with ρ_A are stationary, so that in the coarse-grained region, the entanglement entropy is approximated by a stationary constant,

$$S_A\approx\frac{c\pi\, l_A}{6\epsilon}, \tag{22}$$

where l_A is the subsystem size of A. Let us look closely at the time dependence of the nonuniversal pieces of S_B and $S_{A\cup B}$. The twist and antitwist operators associated with B evolve under $H_{\rm Möbius/SSD}$ and periodically move between the two fixed points $x = X^f_1$ and $x = X^f_2$ with period $L\cosh 2\theta$. In the SSD limit $\theta\to\infty$, the oscillation disappears, and these operators move asymptotically toward one of the fixed points, $x = X^f_2$. The traveling speed of these operators depends on their locations and θ. According to the time evolution of the twist and antitwist operators, the size of the subsystem associated with these operators grows and shrinks with time. Consequently, the geodesic length associated with this subsystem increases and decreases.

For the nonuniversal piece of $S_{A\cup B}$, in the small-t_1 regime, the nonuniversal piece of $S_{A\cup B}$ may be given by the lengths of geodesics connecting the endpoints of A and B, $S_{\rm con}$, while in the large-t_1 regime, it may be given by the ones connecting the endpoints on the same Euclidean time slices $S_{\rm dis}$. Therefore, for large t_1, the nonuniversal pieces of S_B and $S_{A\cup B}$ may be determined by the lengths of the geodesics connecting the endpoints of the subsystems on the same Euclidean time slices as in Fig. 1. More specifically, for the t_1 regime where $(w^{\rm New}_{Y_1,\epsilon}-w^{\rm New}_{Y_2,\epsilon})/(i\epsilon)\gg 1$, $(\overline{w}^{\rm New}_{Y_1,\epsilon}-\overline{w}^{\rm New}_{Y_2,\epsilon})/(i\epsilon)\gg 1$, $[iL-(w^{\rm New}_{Y_1,\epsilon}-w^{\rm New}_{Y_2,\epsilon})]/(i\epsilon)\gg 1$ and $[iL+(\overline{w}^{\rm New}_{Y_1,\epsilon}-\overline{w}^{\rm New}_{Y_2,\epsilon})]/(i\epsilon)\gg 1$, $S_{A\cup B}$ should be approximated by

$$S_{A\cup B}\approx\mathrm{Min}[\hat{S}_1,\hat{S}_2]$$
$$=\frac{c\pi}{6\epsilon}\times\mathrm{Min}\left[L+\left(X^{\rm New}_{Y_1,\epsilon}-X^{\rm New}_{Y_2,\epsilon}-l_A\right),\right.$$
$$\left.L-\left(X^{\rm New}_{Y_1,\epsilon}-X^{\rm New}_{Y_2,\epsilon}\right)+l_A\right], \tag{23}$$

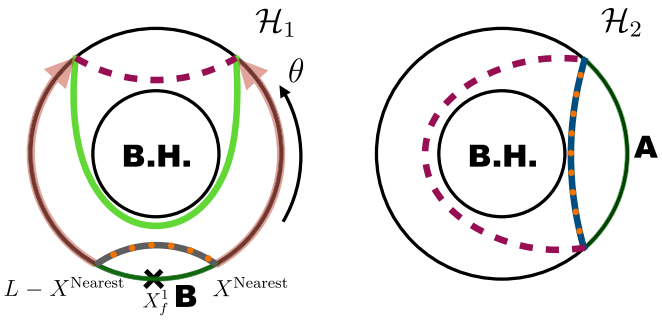

[a] The geodesics associated with B in $\mathcal{H}_1$.

[b] The geodesics associated with A in $\mathcal{H}_2$.

FIG. 1. The Möbius evolution of the subsystem in the Heisenberg picture. The green lines illustrate the subsystems, A and B. The blue solid line illustrates the nonuniversal piece of S_A. The gray solid line illustrates the nonuniversal pieces of S_B for small θ, while the light green solid line illustrates that of S_B for large θ. For $0 \leqslant \theta \leqslant \theta_C$, the nonuniversal piece of $S_{A\cup B}$ is the orange dashed line, while for $\theta_C < \theta$, it is given by the purple dotted lines. The red arrow illustrates the growth of $X^{\text{Nearest}}_{i=Y_1,Y_2}$ with the increase of θ. The details of θ_C is reported in Appendix B 2.

where $\hat{S}_2$ is the same as the nonuniversal piece of S_B in this time regime.

Which of these contributions, $\hat{S}_1$ and $\hat{S}_2$, is dominant depends on θ and there is a threshold value θ_C separating the two cases. In the small-θ regime, $0 \leqslant \theta \leqslant \theta_C$, S_{dis} is given by $\hat{S}_2$, so that for small θ but large t_1, $I_{A,B}$ is zero. On the other hand, in the large-θ regime, $\theta_C < \theta$, S_{dis} is given by $\hat{S}_1$. In this time regime, S_A and S_B are approximated by (22) and $\frac{c\pi[L-(X^{\text{New}}_{Y_1,\epsilon}-X^{\text{New}}_{Y_2,\epsilon})]}{6\epsilon}$, respectively, so that $I_{A,B}$ is approximated by

$$I_{A,B} \approx \frac{c\pi\left[l_A - \left(X^{\text{New}}_{Y_1,\epsilon} - X^{\text{New}}_{Y_2,\epsilon}\right)\right]}{3\epsilon}. \tag{24}$$

The critical value θ_C separating these two cases depends on $Y_{i=1,2}$, $X_{i=1,2}$, and L and can be determined as follows. Let us suppose that $\overline{\sigma}_n(w^{\text{New}}_{Y_2,\epsilon}, \overline{w}^{\text{New}}_{Y_2,\epsilon})$ moves with time between $x = X^{\text{Nearest}}_{Y_2}$ and $x = X^{\text{Furthest}}_{Y_2}$ where $0 < X^{\text{Furthest}}_{Y_2} < X^{\text{Nearest}}_{Y_2} < L/2$, while $\sigma_n(w^{\text{New}}_{Y_1,\epsilon}, \overline{w}^{\text{New}}_{Y_1,\epsilon})$ moves between $x = X^{\text{Nearest}}_{Y_1}$ and $x = X^{\text{Furthest}}_{Y_1}$ where $L/2 < X^{\text{Nearest}}_{Y_1} < X^{\text{Furthest}}_{Y_1} < L$. If θ becomes larger, then $X^{\text{Nearest}}_{i=Y_1,Y_2}$ gets closer to X^f_2. Let $t_{1,\text{Max}}$ denote the time for the effective size of B to reach its maximum. This time, $t_{1,\text{Max}}$, depends on θ, Y_1, and Y_2. Let θ_C denote the value of inhomogeneous parameter, for which $L - (X^{\text{New}}_{Y_1,\epsilon} - X^{\text{New}}_{Y_2,\epsilon})$ is equal to $X^{\text{New}}_{Y_1,\epsilon} - X^{\text{New}}_{Y_2,\epsilon}$ at $t_1 = t_{1,\text{Max}}$. The details of the analysis of θ_C are reported in Appendix B 2.

For H_{SSD}, in the time regime when the B.H.-like excitations, with each of them having half of the thermal entropy on $\mathcal{H}_1$, emerge around $x = X^f_1$ [31], $I_{A,B}$ is approximated by

$$I_{A,B} \approx \frac{2c\pi l_A}{6\epsilon}, \tag{25}$$

where $l_A = X_1 - X_2$. One possible interpretation for $I_{A,B}$ after the emergence of the B.H.-like excitations is that $I_{A,B}$ may measure the Bell pairs initially shared by A and $\mathcal{H}_1$.

If B does not include $x = X^1_f$, then for the large-t_1 regime under the SSD evolution, the nonuniversal piece of $S_{A\cup B}$ is given by that of $S_A + S_B$ where S_B is approximated by the entanglement entropy of the vacuum state. As a consequence, $I_{A,B}$ is zero at late times. This means that the reduced density matrix on $A \cup B$ approximately factorizes as

$$\rho_{A\cup B}(t_1 \gg 1) \approx \rho_{\text{Thermal},A} \otimes \rho_{\text{Vacuum},B}, \tag{26}$$

where $\rho_{\text{Thermal},A}$ is the reduced density matrix of a thermal state at inverse temperature 2ϵ for subsystem A, and $\rho_{\text{Vacuum},B}$ the reduced density matrix of the vacuum state for subsystem B.

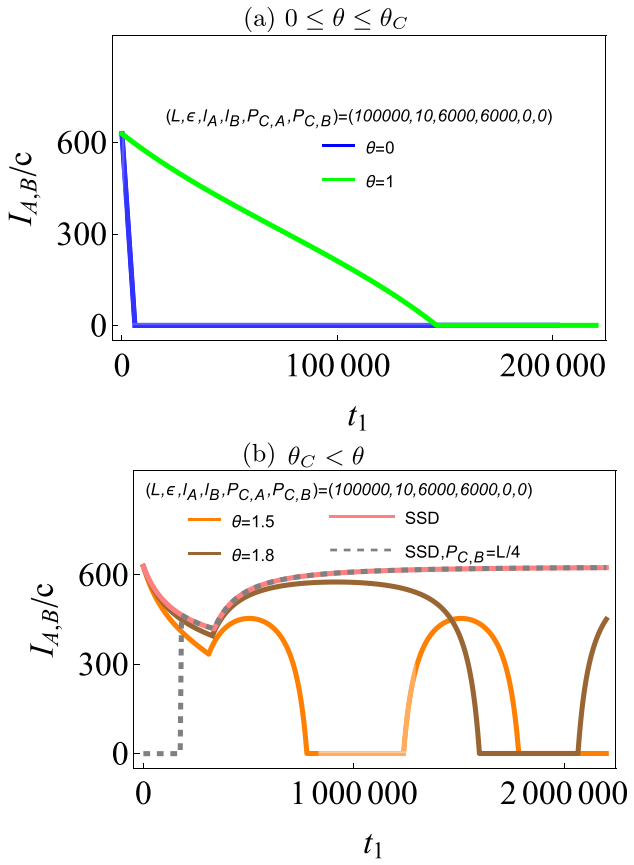

FIG. 2. The time dependence of $I_{A,B}$ for (a) $0 \leqslant \theta \leqslant \theta_C$ and (b) $\theta_c < \theta$ as a function of t_1. Here, $l_{\alpha=A,B}$ and $P_{C,\alpha=A,B}$ denote the size and the center of α.

1. The θ and position dependence of $I_{A,B}$

The behavior of the geodesic and the time evolution of the subsystems in the Heisenberg picture described above is directly translated into the time dependence of $I_{A,B}$. In Fig. 2, we plot $I_{A,B}$ for various choices of θ as a function of t_1. In this plot, the center of B is $x = X^f_1$. The solid lines illustrate the time dependence of $I_{A,B}$ for A, the center of which is $x = X^f_1$, while the dashed line illustrates that for A, the center of which is $x = \frac{L}{4}$. In Fig. 2(a), we show the time dependence of $I_{A,B}$ for the small θ region where $0 \leqslant \theta \leqslant \theta_C$, while in (b), we show that for the large θ region where $\theta_C < \theta$.

As discussed in Sec. III A, in the late time regime, $I_{A,B}$ for $0 \leqslant \theta \leqslant \theta_C$ is practically zero, while that for $\theta_C < \theta$ becomes positive. For $0 \leqslant \theta \leqslant \theta_C$, $I_{A,B}$ monotonically decreases with t_1 up to $t_{1,*}$, and then is practically zero. Here, $t_{1,*}$ is the

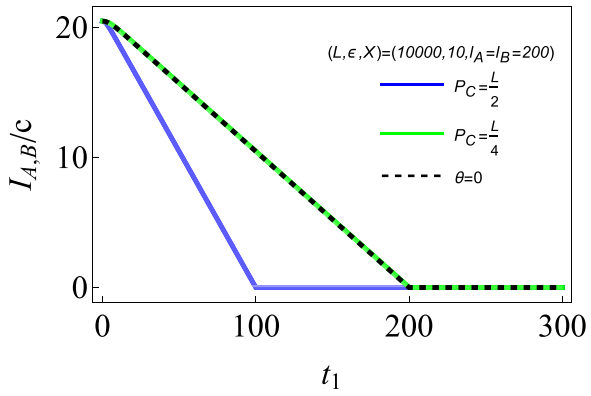

FIG. 3. The time dependence of $I_{A,B}$ for $P_C = \frac{L}{4}, \frac{L}{2}$ for $\theta = 0$ (dashed line) and in the SSD limit (solid lines) as a function of t_1. Here, we choose $l_A = l_B$ and $P_{C,A} = P_{C,B} = P_C$. The solid lines illustrate the t_1 dependence of $I_{A,B}$ for $P_C = \frac{L}{4}, \frac{L}{2}$ in the SSD limit. For $\theta = 0$, the time dependence of $I_{A,B}$ is independent of P_C.

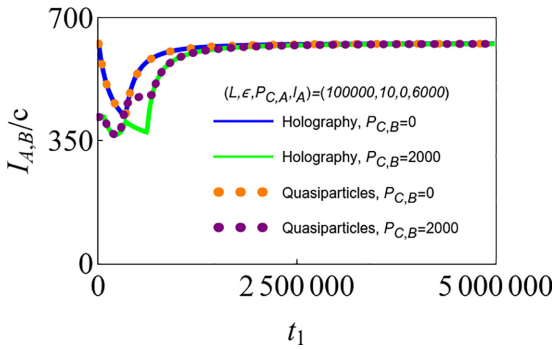

FIG. 4. The time dependence of $I_{A,B}$ in the SSD limit as a function of t_1. Here, we compare the t_1 dependence of $I_{A,B}$ that follows from the propagation of quasiparticles (dotted lines) with that of $I_{A,B}$ in 2d holographic CFTs (solid lines). In this figure, $P_{C,J=A,B}$ and $l_{J=A,B}$ denote the centers and sizes of $J = A$ and B, respectively.

phase-transition time where $S_{\rm con}$ exchanges dominance with $S_{\rm dis}$. The details of early time decay depends on θ: For larger θ, the early time decay is slower ($t_{1,*}$ is bigger). This behavior for $\theta \leqslant \theta_C$ is similar to what was found for bipartite operator mutual information of the regular homogeneous time-evolution operator of holographic CFTs in Ref. [54].

On the other hand, the behavior for $\theta_C < \theta$ is markedly different. Except for the SSD limit, $I_{A,B}$ first monotonically decreases with t_1 up to $t_{1,*}$, and then oscillates with periodicity $L\cosh 2\theta$. For larger θ (closer to the SSD limit), the early time decay is slower, and $I_{A,B}$ at $t_1 = t_{1,*}$ is larger. In the SSD limit, after $t_1 = t_{1,*}$ $I_{A,B}$ grows with t_1, and saturates to a value that is proportional to the size of A. We will revisit this behavior in Sec. VI by developing the line-tension picture (membrane picture) for inhomogeneous chaotic time-evolution operators.

Let us turn to the analysis of the position dependence of $I_{A,B}$. For simplicity, let us consider the SSD limit, and $l_A = l_B$, and $P_{C,A} = P_{C,B} = P_C$. We can see from the time dependence of $I_{A,B}$ how scrambling may destroy the nonlocal correlation between A and B. Also, we can see the times when $\rho_{A\cup B}$ may approximately factorize into ρ_A and ρ_B,

$$\rho_{A\cup B} \approx \rho_A \otimes \rho_B. \tag{27}$$

In Fig. 3, we depict $I_{A,B}$ for various P_C as the function of t_1. In this figure, we take P_C to be $\frac{L}{4}$ and $\frac{L}{2}$. From the time dependence of $I_{A,B}$ in Fig. 3, we can see that when θ becomes larger, the early time decay of $I_{A,B}$ for $P_C = \frac{L}{2}$ becomes faster and the time for $\rho_{A\cup B}$ to factorize into ρ_A and ρ_B may become smaller. For $P_C = \frac{L}{4}$, the t_1 dependence of $I_{A,B}$ may be independence of θ. One possible explanation for the t_1 dependence is that the inhomogeneous deformation may promote scrambling to destroy the nonlocal correlation around $P_C = X_f^2$, while this deformation may make scrambling destroy it around $P_C = X_f^1$ slower, and then prevent $\rho_{A\cup B}$ from factorizing into ρ_A and ρ_B.

2. *Theory dependence of $I_{A,B}$ under evolution*

We have so far focused on holographic CFTs. However, as one of our motivations is to understand quantum information scrambling behaviors and their theory dependence, we now make a comparison, for the time dependence of $I_{A,B}$, between 2d holographic CFTs with the 2d free fermion CFT. First, as we show in Appendix D, for the free fermion CFT with inhomogeneous time evolution, we can establish that its entanglement dynamics is described by the quasiparticle picture, just like the standard case of homogeneous time evolution. In this picture, the time dependence of $I_{A,B}$ follows the propagation of quasiparticles at speeds given by $H_{\rm Möbius/SSD}$. Some details of the calculations of $I_{A,B}$ in the 2d free fermion CFT and a detailed description of the quasiparticle picture can be found in Appendix D. The upshot is that the BMI in the 2d free fermion CFT is carried separately by left- and right-moving quasiparticles that move independently of one another. These quasiparticles are localized packets of information and their number is conserved. In Fig. 4, we plot $I_{A,B}$ in the SSD limit as a function of t_1. We see that if the size and center of A are the same as B, then the time dependence of $I_{A,B}$ in 2d holographic CFTs follows the quasiparticle picture. This is, however, not the case otherwise. We will propose an effective picture that describes the t_1 dependence of $I_{A,B}$ in the 2d holographic CFTs in Sec. VI.

B. Tripartite mutual information

Let us turn to TMI. Suppose that we divide $\mathcal{H}_2$ into A and its complement, and also $\mathcal{H}_1$ into B_1 and B_2, and then define TMI as $I_{A,B_1,B_2} = I_{A,B_1} + I_{A,B_2} - I_{A,B_1\cup B_2}$. Here, we also assume that $l_A = l_{B_1}$ and $P_{C,A} = P_{C,B} = X_f^1$. Then, the time dependence of I_{A,B_1} is the same as that of $I_{A,B}$ reported in Sec. III A 1, while I_{A,B_2} is independent of t_1 and approximately zero. In the coarse-grained regime, $I_{A,B_1\cup B_2}$ is also independent of t_1 and approximated by (25). During the evolution by $H_{\rm Möbius}$ with $0 \leqslant \theta \leqslant \theta_C$, I_{A,B_1,B_2} is a stationary constant in (25), while for $\theta_C < \theta$, I_{A,B_1,B_2} is a periodic function of t_1 with period $T = L\cosh 2\theta$. The range of $I_{A,B}$ is between zero and (25). In the SSD limit, the time dependence of I_{A,B_1,B_2} is approximated by $I_{A,B_1,B_2} \approx I_{A,B} - \frac{2c\pi l_A}{6\epsilon}$, where $I_{A,B}$ is reported in Sec. III A 1. For large-t_1 regime, I_{A,B_1,B_2} saturates to zero. One possible explanation for the late-time value of I_{A,B_1,B_2} is that the correlation initially shared by A and B_1 may not be scrambled in the whole $\mathcal{H}_1$, and this correlation between A and B_1 may be revived.

IV. SETUP 2

In this section, we present the time dependence of BMI and TMI for Setup 2, (5). Recall that in (5) the state is first time evolved by the homogeneous Hamiltonian and then by the SSD Hamiltonian. In holographic CFTs, the first step of the time evolution scrambles quantum information of the initial state and produce a typical state (the Page state) [89,90]. Our focus here is the effect of the second step of the time evolution on the scrambled information.

Let us focus on the analysis of the lengths of geodesics corresponding to $I_{A,B}$. Let $\mathcal{V}_1$ and $\mathcal{V}_2$ denote the subregions on $\mathcal{H}_1$ and $\mathcal{H}_2$, respectively, and also let $l_{\mathcal{V}_{i=1,2}}$ denote the size of $\mathcal{V}_{i=1,2}$, respectively. For large t_0, $t_0 \gg \mathcal{O}(L)$, the 2d holographic CFTs Hamiltonian evolves the system to the Page state, so that for all $\mathcal{V}_{i=1,2}$ where $\sum_{i=1,2} l_{\mathcal{V}_i} < L$, $I_{\mathcal{V}_1,\mathcal{V}_2}$ should be completely destroyed. Subsequently, we evolve it with $H_{\rm SSD}$. In the large-t_1 regime, $S_{\rm con}$ should be larger than $S_{\rm dis}$. For simplicity let us assume that A and B include $x = X_f^1$. In this case, $w_{x,\epsilon}^{\rm New}$ and $\bar{w}_{x,\epsilon}^{\rm New}$ in this setup are obtained from those in Setup 1 by shifting by it_0, $w_{x,\epsilon}^{\rm New} \to it_0 + w_{x,\epsilon}^{\rm New}$ and $\overline{w}_{x,\epsilon}^{\rm New} \to it_0 + \overline{w}_{x,\epsilon}^{\rm New}$. For $S_{\rm dis}$ and S_B, the shifts by it_0 are canceled, so that $S_{A\cup B}$ and S_B in this setup is the same as those in Setup 1. Since for small t_1, $S_{A\cup B} = S_A + S_B$, the early time $I_{A,B}$ is zero. For large t_1, excluding the t_1 regime when $X_{Y_1,\epsilon}^{\rm New} - X_{Y_2,\epsilon}^{\rm New} \ll \epsilon$, the t_1 dependence of $S_{A\cup B}$ should be given by

$$S_{A\cup B} \approx \frac{c\pi}{6\epsilon}\left[X_{Y_1,\epsilon}^{\rm New} - X_{Y_2,\epsilon}^{\rm New} + (X_1 - X_2)\right]. \tag{28}$$

The distance between $X_{Y_1,\epsilon}^{\rm New}$ and $X_{Y_2,\epsilon}^{\rm New}$ decreases with t_1, so that $I_{A,B}$ may grow with t_1 and saturate to (25).

In fact, as in Fig. 5, for $P_{C,A} = P_{C,B} = 0$ and $l_A = l_B$, even in the large-t_0 regime, the $I_{A,B}$ grows with t_1, and then saturates at the value in (25). One possible interpretation for the t_1 dependence of $I_{A,B}$ in this figure is that the SSD evolution may recover the nonlocal correlation between A and the subsystem including $x = X_f^1$ even when the system is in the typical state. The SSD time evolution is able to recover the mutual information from the typical state.

The above recovery of quantum information is analogous to the one discussed in quantum circuit models of quantum information scrambling and black holes, e.g., the Hayden-Preskill thought experiment [15,55] where the authors considered the retrieval of the quantum information from a black hole. To make a comparison, we can describe Setup 2 in the quantum circuit language as in Fig. 5. Here, in the parameter region considered in this paper [see (11)], the TFD state may be approximated by the product of Bell states, $|{\rm TFD}\rangle \approx \prod_{x=0}^{L} |{\rm Bell}; x\rangle$, where $|{\rm Bell}, x\rangle$ denotes the Bell state at the spatial location x. For example, if the dimension of the local Hilbert space at x is d, then the definition of a single Bell state is given by $|{\rm Bell}; x\rangle = \frac{1}{\sqrt{d}} \sum_{q=1}^{d} |q\rangle_1 \otimes |q\rangle_2$. Let us divide these Bell pairs into two groups, G_1 and G_2. Let R and E denote the subregions associated with G_1 of $\mathcal{H}_1$ and $\mathcal{H}_2$, respectively, while let B and N denote the subregions associated with G_2 of $\mathcal{H}_1$ and $\mathcal{H}_2$. In Fig. 5, $U_{\rm SSD}$ and $U_{\rm Hol.}$ denote the time evolution induced by the holographic uniform Hamiltonian and $H_{\rm SSD}$, respectively. The process under the dashed line is the same as the one considered in the Hayden-Preskill thought experiment. If we interpret $U_{\rm SSD}$ as a unitary decoder, the location where this decoder acts is different from that discussed in the Hayden-Preskill thought experiment. Therefore, it would be interesting to consider the information retrieval in the system where the $U_{\rm SSD}$ acts on E and R. This is left for future work.

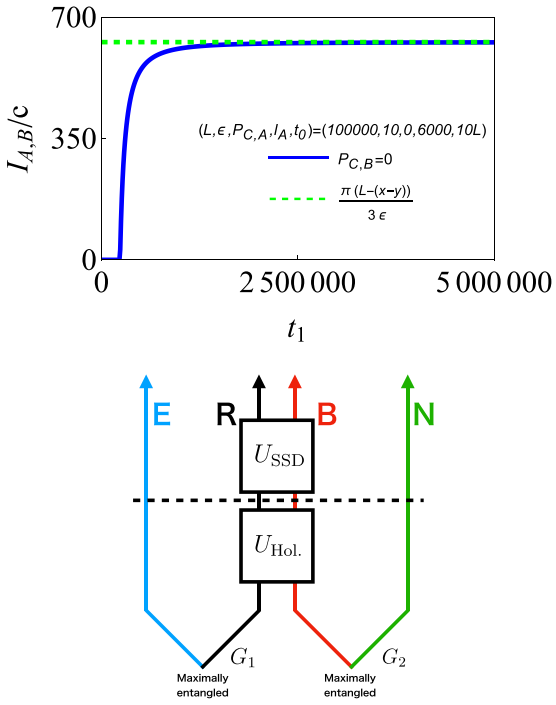

FIG. 5. (Top) The time dependence of $I_{A,B}$ in the SSD limit as a function of t_1. The solid line illustrates the t_1 dependence of $I_{A,B}$ for $t_0 = 10L$. The dashed line is the asymptotic value in (25). In this figure, $P_{C,J=A,B}$ and $l_{J=A,B}$ denote the centers and sizes of $J = A$ and B, respectively. (Bottom) Quantum circuit description of Setup 2.

V. SETUP 3

In this section, we study the entanglement dynamics of the state (6). Here, the first part of the two-step time evolution (with the SSD Hamiltonian on $\mathcal{H}_1$, $H_{\rm SSD}^1$) can be interpreted as preparing a pair of B.H.-like excitations. The created B.H.-like excitations are then subject to the second step of the time evolution under H_0^1 (Fig. 7, see below). As we will show below, the propagating B.H.-like excitations lead to periodic behaviors of entanglement quantities. Furthermore, in this setup, the system acquires genuine tripartite entanglement due to the strong scrambling effect of the dynamics. On the contrary, in the 2d free fermion CFT, the B.H.-like excitations are just the clusters of quasiparticle, and no such tripartite entanglement arises.

A. Entanglement entropy

Let us first study S_B. In particular, we present the t_0 dependence of S_B in three cases: (a) $x = X_f^1 \in B$; (b) $\frac{L}{2} > Y_1 > Y_2 > 0$; (c) $x = X_f^2 \in B$. In Fig. 6, we plot S_B for various t_1 as a function of t_0. The t_0 dependence of S_B is periodic with period L. This periodic behavior follows from the evolution

of twist and antitwist operators reported in Appendix A 1. The larger t_1 is, the larger the amplitude of the oscillation of S_B is, and the system deviates further from the typical state. The time dependence of S_B for the single interval can be understood by the quasiparticle picture (we provide the details in Appendix D). For $t_1 \gg 1$, the t_0 dependence of S_B is approximated by

$$
\begin{aligned}
\text{For (a)},\ S_B \approx \begin{cases} \frac{c\pi L}{6\epsilon} \\ \frac{c\pi L}{12\epsilon} \\ \frac{c}{3}\log\left[\frac{L}{\pi}\sin\left[\frac{\pi(Y_1-Y_2)}{L}\right]\right] \\ \frac{c\pi L}{12\epsilon} \end{cases} & \begin{matrix} nL+Y_2 > t_0 > nL-Y_2 \\ (n+1)L-Y_1 > t_0 > nL+Y_2 \\ nL+Y_1 > t_0 > (n+1)L-Y_1 \\ (n+1)L-Y_2 > t_0 > nL+Y_1 \end{matrix} \\
\text{For (b)},\ S_B \approx \begin{cases} \frac{c}{3}\log\left[\frac{L}{\pi}\sin\left[\frac{\pi(Y_1-Y_2)}{L}\right]\right] \\ \frac{c\pi L}{12\epsilon} \\ \frac{c}{3}\log\left[\frac{L}{\pi}\sin\left[\frac{\pi(Y_1-Y_2)}{L}\right]\right] \\ \frac{c\pi L}{12\epsilon} \end{cases} & \begin{matrix} nL+Y_2 > t_0 > nL-Y_2 \\ nL+Y_1 > t_0 > nL+Y_2 \\ (n+1)L-Y_1 > t_0 > nL+Y_1, \\ (n+1)L-Y_2 > t_0 > (n+1)L-Y_1 \end{matrix} \\
\text{For (c)},\ S_B \approx \begin{cases} \frac{c}{3}\log\left[\frac{L}{\pi}\sin\left[\frac{\pi(Y_1-Y_2)}{L}\right]\right] \\ \frac{c\pi L}{12\epsilon} \\ \frac{c\pi L}{6\epsilon} \\ \frac{c\pi L}{12\epsilon} \end{cases} & \begin{matrix} nL+Y_2 > t_0 > nL-Y_2 \\ (n+1)L-Y_1 > t_0 > nL+Y_2 \\ nL+Y_1 > t_0 > (n+1)L-Y_1 \\ (n+1)L-Y_2 > t_0 > nL+Y_1 \end{matrix}
\end{aligned}
\tag{29}
$$

where n is an integer.

The periodic behavior (29) can be understood from the relativistic propagation of the two local objects that have a huge amount of information, i.e., B.H.-like excitations. Here, we introduce an effective model that describes the time evolution of S_B induced by H_0 for the large-t_1 regime. This model describes the leading behavior of S_B in the coarse-grained regime. At $t_1 = t_0 = 0$, in the coarse-grained regime, the leading behavior of the TFD state (3) may be approximated by the state consisting of the product of Bell pairs,

$$
|\text{TFD}\rangle \approx \prod_{\tilde{x}} |\text{Bell};\tilde{x}\rangle_L |\text{Bell};\tilde{x}\rangle_R, \tag{30}
$$

where $\tilde{x}$ is defined as $\tilde{x} \equiv \frac{x}{\epsilon}$, and $|\text{Bell};\tilde{x}\rangle_{L,R}$ denote the Bell pairs consisting of the two quasiparticles at $\tilde{x}$ in $\mathcal{H}_1$ and $\mathcal{H}_2$ respectively as in Fig. 7. During the unitary time evolution by H_0^1 or H_{SSD}^1, the quasiparticles on $\mathcal{H}_1$ of $|\text{Bell};\tilde{x}\rangle_L$ and $|\text{Bell};\tilde{x}\rangle_R$ correspond to the left- and right-moving particles respectively. These particles move to the left and right at the speed determined by H^1 or H_{SSD}^1. During the evolution by H_{SSD}^1, all particles on $\mathcal{H}_1$ move to $x = X_f^1$ and accumulate around $x = X_f^1$ [31]. For large t_1, two B.H.-like excitations emerge around $x = X_f^1$. After these excitations emerge, the entanglement entropy for the subsystem including $x = X_f^1$ is approximated by $\frac{c\pi L}{6\epsilon}$. Subsequently, we evolve this system with H_0, and then one of the B.H.-like excitation moves to the left and the other moves to the right at the speed of light. In the time regime where one of these excitations is in B, S_B is approximated by $\frac{c\pi L}{12\epsilon}$, while in the time regime where both are in B, S_B is approximated by $\frac{c\pi L}{6\epsilon}$. In the time regime where no excitations are in B, S_B is approximated by $\frac{c}{3}\log[\frac{L}{\pi}\sin[\frac{\pi(Y_1-Y_2)}{L}]]$.

B. Bipartite and tripartite mutual information, and genuine tripartite entanglement

In the previous sections, we have developed an effective picture in terms of B.H.-like excitations to describe the time evolution of entanglement entropy for a single interval. We note that the above behavior is universal for any CFT. We now generalize it to the time evolution of BMI and TMI. Here, the distinction between integrable (e.g., the free fermion theory) and chaotic theories (holographic theories) becomes important. In the free fermion theory, the B.H.-like excitations are just clusters of quasiparticles. On the other hand, this is not the case in holographic CFTs and the interior of B.H.-like excitations should have a strong scrambling effect.

1. Bipartite mutual information

Let us first consider BMI $I_{A,B}$ for the time-evolved state (6). Here A and B are the subregions (single intervals) of $\mathcal{H}_1$ and $\mathcal{H}_2$. BMI $I_{A,B}$ can be thought of as measuring the number of Bell pairs shared by A and B. Let us consider extracting a Bell pair from the B.H.-like excitations. At $t_0 = t_1 = 0$, the system is in the TFD state approximated by (30). Consider a single Bell pair shared by quasiparticles, $q_{1,D}^i$ and $q_{2,D}^i$. Here, $q_{j=1,2,D=L,R}^i$ denote a quasiparticle on ith site of $\mathcal{H}_j$, and $D = L/R$ refers left/right-moving quasiparticles. When evolved with H_{SSD}^1, the B.H.-like excitations emerge around $x = X_f^1$. Then, we attempt to extract from the B.H.-like

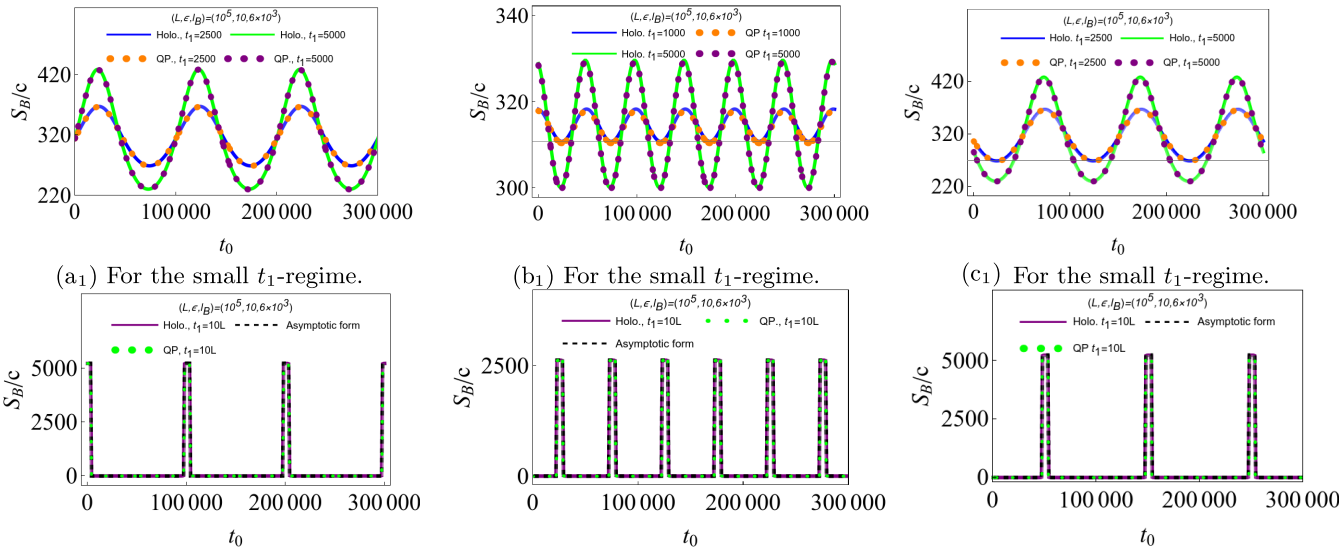

FIG. 6. The entanglement entropy S_B as a function of t_0 for various choices of t_1 for three configurations (a) $x = X_f^1 \in B$, (b) $\frac{L}{2} > Y_1 > Y_2 > 0$, and (c) $x = X_f^2 \in B$. The subscript in $(a_{i=1,2})$ distinguishes the small and large-t_1 regimes (top and bottom rows, respectively). The dashed line illustrates the asymptotic behavior of S_B in (29) in the large-t_1 limit.

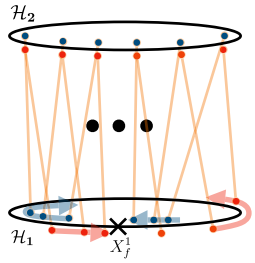

(a) The propagation of quasiparticles on $\mathcal{H}_1$ during the SSD time-evolution.

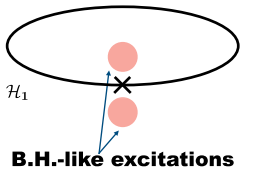

(b) The emergence of B.H.-like excitations.

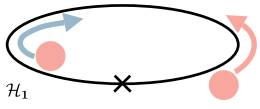

(c) The relativistic propagation of the B.H.-like excitations during the evolution by H_0.

FIG. 7. The emergence and the time evolution of the two B.H.-like excitations.

excitations the Bell pair that $q^i_{1,D}$ and $q^i_{2,D}$ initially share. In the free fermion theory, if a single B.H.-like excitation includes $q^i_{1,L}$, then we can extract the Bell pair shared by $q^i_{1,L}$ and $q^i_{2,L}$ from this excitation [Fig. 8(a)]. The situation is crucially different for 2d holographic CFTs; we cannot extract this Bell pair from only the single B.H.-like excitation [Fig. 7(b)]. This is because quasiparticles in $\mathcal{H}_1$ are locally hidden in the two B.H.-like excitations by the scrambling effect. In fact, as we will show momentarily, when only a single B.H.-like excitation is in B, $I_{A,B}$ is zero. On the other hand, when both of the B.H.-like excitations are in B, A and B share the Bell pairs initially shared by A and $\mathcal{H}_1$.

In Fig. 9, we plot $I_{A,B}$ as a function of t_0 for various choices of t_1, A and B. Here, for the configurations of A and B, we consider the following three cases: (a) $x = X_f^1 \in B$; (b) $\frac{L}{2} > Y_1 > Y_2 > 0$; (c) $x = X_f^2 \in B$. For (b), we assume that A and B are the disjoint intervals for simplicity. Then, $I_{A,B}$ is approximately zero. For (a) and (c), for large t_1, $I_{A,B}$ is approximated by the following periodic function of t_0 with period L,

For (a) :

$$I_{A,B} \approx \begin{cases} \frac{c\pi l_A}{3\epsilon} & \text{for } (n+1)L - Y_1 > t_0 > nL - Y_2 \\ 0 & \text{for } (n+1)L - Y_2 > t_0 > (n+1)L - Y_1, \end{cases}$$

For (c) :

$$I_{A,B} \approx \begin{cases} 0 & \text{for } (n+1)L - Y_1 > t_0 > nL - Y_2 \\ \frac{c\pi l_A}{3\epsilon} & \text{for } nL + Y_1 > t_0 > (n+1)L - Y_1 . \\ 0 & \text{for } (n+1)L - Y_2 > t_0 > nL + Y_1 \end{cases} \quad (31)$$

The dashed lines in Fig. 9 illustrate these asymptotic behaviors. In these cases, there are the t_0 regimes where both

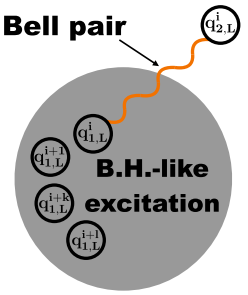

(a) 2d free fermion.

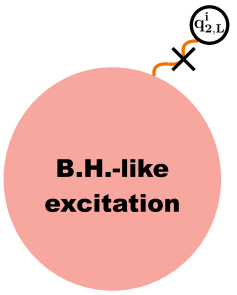

(b) 2d holographic CFTs.

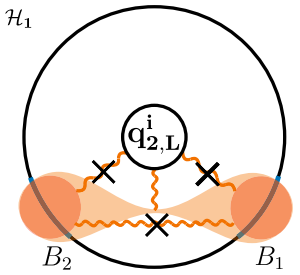

(c) Extraction from both B.H.-like excitations.

FIG. 8. Retrieval of a single Bell pair from B.H.-like excitations in the 2d free fermion theory (a) and 2d holographic CFTs (b). Panel (c) illustrates the retrieval of a single Bell pair from both B.H.-like excitations in 2d holographic CFTs. The subsystems, B_1 and B_2, are the symmetric intervals in (32). The red-shadowed region is the region where quantum information is scrambled. The orange-shadowed region illustrates $q^i_{1,L}$ is shared by two B.H.-like excitations.

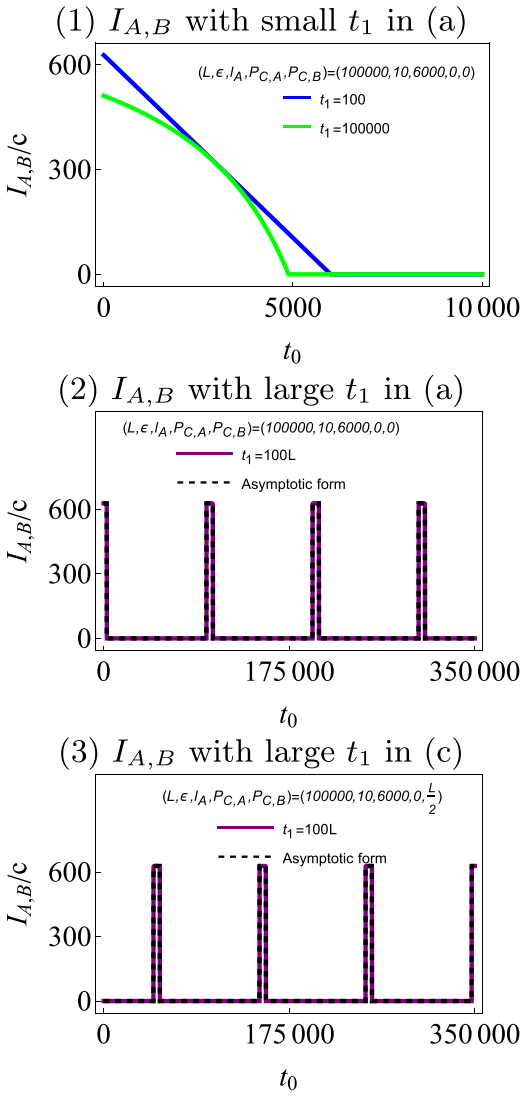

FIG. 9. The BMI $I_{A,B}$ of (6) as a function of t_0 for various choices of t_1. For simplicity, we take l_A to be the same as l_B. In (2) and (3), the dashed lines are the asymptotic behavior in (31).

B.H.-like excitations are in B, and in these regimes, $I_{A,B}$ is approximated by $\frac{c\pi l_A}{3\epsilon}$, while in (b), there are no such t_0 regimes.

2. *Tripartite mutual information*

In summary, the two B.H.-like excitations in 2d holographic CFTs should be (local) excitations, each of which has half the entropy of a black hole, and information inside this excitation should be scrambled. We cannot extract Bell pairs from a single B.H.-like excitation, while we can extract them from both excitations [Fig. 8(c)]. To further discuss this, let us now consider the case where B consists of two intervals, B_1 and B_2, $B = B_1 \cup B_2$. Specifically, we consider the case where B is given by a union of symmetric double intervals,

$$B_1 = \left\{ x \middle| L > L - Y_2 > x > L - Y_1 > \frac{L}{2} \right\},$$
$$B_2 = \left\{ x \middle| \frac{L}{2} > Y_1 > x > Y_2 > 0 \right\}, \tag{32}$$

where $\frac{L}{2} > Y_1 > Y_2 > 0$. In Fig. 10, we take $Y_1 > Y_2 > X_1 > X_2 > 0$. In this case, for small t_1, $I_{A,B=B_1\cup B_2}$ is practically zero, while for large t_1 the t_0 dependence of $I_{A,B}$ is approximated by the following periodic function of t_0 with L,

$$I_{A,B=B_1\cup B_2} \approx \begin{cases} 0 & nL + Y_2 > t_0 > nL - Y_2 \\ \frac{c\pi l_A}{3\epsilon} & nL + Y_1 > t_0 > nL + Y_2 \\ 0 & (n+1)L - Y_1 > t_0 > nL + Y_1 \\ \frac{c\pi l_A}{3\epsilon} & (n+1)L - Y_2 > t_0 > (n+1)L - Y_1 \end{cases}. \tag{33}$$

In this case, there are t_0 regimes where both the B.H.-like excitations are in $B = B_1 \cup B_2$. In these t_0 regimes, the $I_{A,B_1\cup B_2}$

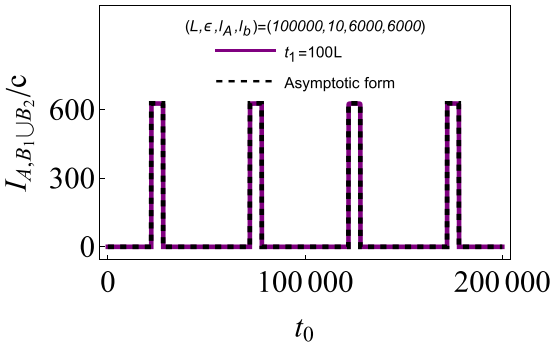

FIG. 10. The BMI $I_{A,B_1\cup B_2}$ in the large-t_1 regime as a function of t_0. The solid line illustrates the t_1 dependence of $I_{A,B_1\cup B_2}$ for $t_1 = 10^2 L$. In this figure, $l_{B_1} = l_{B_2} = l_b$, $P_{C,B_1} = \frac{3L}{4}$, and $P_{C,B_2} = \frac{L}{4}$. The center of A is $x = X_1^f$. The dashed line illustrates the t_0 dependence of $I_{A,B_1\cup B_2}$ in (33).

is approximated by $\frac{c\pi l_A}{3\epsilon}$. This suggests that we may be able to reconstruct $I_{A,B}$ from all quasiparticles in A and $\mathcal{H}_1$ even under the 2d holographic time evolution. Also, we can see from the t_0 dependence of $I_{A,B}$ for large t_1 that the time evolution of $I_{A,B}$ may follow the relativistic propagation of the local excitations as in [24,25,91].

By combining BMI for single intervals A, B, and for a single interval A and double interval $B = B_1 \cup B_2$, we can discuss TMI. By considering local and global TMI defined below, let us show that the amount of information scrambled by the dynamics depends on the observers. Define local TMI for (32) as

$$I_{A,B_1,B_2} = I_{A,B_1} + I_{A,B_2} - I_{A,B_1\cup B_2}, \tag{34}$$

where A denotes the subsystem of $\mathcal{H}_2$. (Here, let us the t_0 dependence of TMI in the large-t_1 regime.) In the large-t_1 regime, $I_{A,B_{i=1,2}}$ is approximated by zero, while the t_0 dependence of $I_{A,B_1\cup B_2}$ is given by (33). Thus, the local TMI, I_{A,B_1,B_2} in the large-t_1 regime is zero for $nL + Y_2 > t_0 > nL - Y_2$ or $(n+1)L - Y_1 > t_0 > nL + Y_1$, while it is approximated by $-\frac{c\pi l_A}{3\epsilon}$ for $nL + Y_1 > t_0 > nL + Y_2$ or $(n+1)L - Y_2 > t_0 > (n+1)L - Y_1$. The negativity of I_{A,B_1,B_2} is the signature of scrambling. On the other hand, define global TMI as

$$I_{A,B,\overline{B}} = I_{A,B} + I_{A,\overline{B}} - I_{A,B\cup\overline{B}}, \tag{35}$$

where $\overline{B}$ is the complement to B in $\mathcal{H}_1$. This global TMI is a stationary constant value and zero. One possible interpretation for the t_0 dependence of local and global TMI is that when two B.H.-like excitations are in B, the quasiparticles on $\mathcal{H}_1$ of the Bell pairs initially shared by A and $\mathcal{H}_1$ may be locally hidden in B, while there may be no quasiparticles locally hidden in $\mathcal{H}_1$.

By contrast, the local and global TMI for free fermions is zero for the double interval setup in Fig. 10 in agreement with the quasiparticle picture.

3. Genuine tripartite entanglement

Let us also note the following behavior of BMI in the large-t_1 regime. For the symmetric double intervals in (32), $I_{A,B_{i=1,2}}$ and I_{B_1,B_2} are approximately zero. On the other hand, the t_0 dependence of $I_{A,B_1\cup B_2}$ is given by (33). One possible interpretation for these BMI is that the system in its steady state may have only tripartite entanglement, which we call genuine tripartite entanglement. This genuine tripartite entanglement may be a characteristic property of the system in the steady state during the 2d SSD holographic time evolution. In contrast, in the 2d free fermion theory, there are the t_0 regimes where $I_{A,B_{i=1,2}}$ and I_{B_1,B_2} becomes positive (see Appendix D 3). The reduced density of the system in this steady state may be given by

$$\rho_{A,B_1,B_2} \approx \rho_A \otimes \rho_{B_1} \otimes \rho_{B_2} + \sigma_{A,B_1,B_2}, \tag{36}$$

where σ_{A,B_1,B_2} is Hermitian and traceless, $\mathrm{tr}_A \sigma_{A,B_1,B_2} = \mathrm{tr}_{B_{i=1,2}} \sigma_{A,B_1,B_2} = 0$. The periodic behavior of $I_{A,B_1\cup B_2}$ in t_0 may come from the periodicity of σ_{A,B_1,B_2}, $\sigma_{A,B_1,B_2}(t+L) = \sigma_{A,B_1,B_2}(t)$.

TABLE I. Summary of the properties in Setup 3.

t_1	$\rho_{A\cup B}$	S_B	$I_{A,B}$
Small	$\rho_A \otimes \rho_B$	Approximately stationary	Chaotic
Large	not factorized	Quantum revival	Quantum revival

4. An atypical state

At the end of this section, let us consider the entanglement structure of the steady state under the evolution by H^1. In Table I, we summarize the entanglement property of the system with various t_1 and large t_0. From Table I, we can see that if the system is highly inhomogeneous, then we can not evolve it with even 2d holographic Hamiltonian to the typical state. This atypical state may have a quantum nature because the t_0 dependence of S_B and $I_{A,B}$ is periodic (quantum revival).

VI. LINE TENSION PICTURE

In Sec. III, we studied the time dependence of BMI after quantum quench with the inhomogeneous Hamiltonian as the post quench Hamiltonian. We observed that the BMI is not fully described by the quasiparticle picture. In this section, we propose a generalization of the so-called line-tension picture to a random unitary circuit with the SSD time evolution. In a chaotic system, the entanglement production is effectively described by the line-tension picture introduced in [92–96]. To explain the basic idea of the line-tension picture, here we assume that the spatial direction is homogeneous and infinite. For simplicity, we assume that the system is time evolved by the unitary operator $U(t_1)$ from $t = 0$ to $t = t_1$. We divide the infinite line where the system lives into two pieces at position x at $t = t_1$. We also divide the line at position y at $t = 0$. Now the entanglement entropy $S_U(x, y, t_1)$ of the unitary operator is computed as

$$S_U(x, y, t_1) = \min_{\mathcal{C}} \int_{\mathcal{C}} dt\, \mathcal{T}(v), \tag{37}$$

where the minimization is taken over all the possible curves $\mathcal{C}$ that connects the point (x, t_1) and $(y, 0)$. The symbol $\mathcal{T}(v)$ is

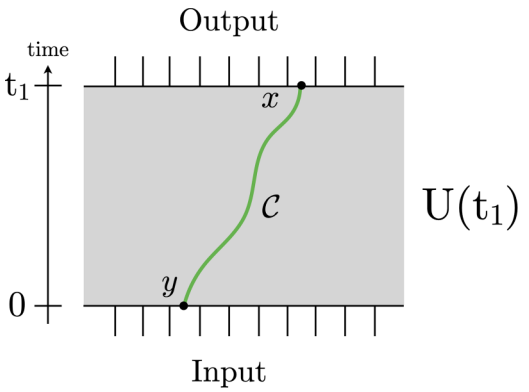

FIG. 11. A curve $\mathcal{C}$ that divides the unitary circuit into two parts. In the line-tension picture, the entanglement entropy $S_U(x, y, t_1)$ is given by the integral of the line tension $\mathcal{T}(v)$ along the curve $\mathcal{C}$.

the line tension associated to a curve $\mathcal{C}$ that connects the point (x, t_1) and $(y, 0)$ as in Fig. 11. The curve $\mathcal{C}$ in spacetime has a velocity $v = dx/dt$ and a line tension $\mathcal{T}(v)$ that depends on v. In our case, when the spacetime is uniform, the minimal curve is given by a straight line with a constant velocity $v = (x - y)/t_1$.

The details of the function $\mathcal{T}(v)$ depend on the system and are estimated in a chaotic system using random unitary circuits, which illustrate the phenomenon of quantum information scrambling. In the scaling limit and in the limit of large bond dimension q, the line tension is simply given by counting the number of bonds cut, which is

$$\mathcal{T}(v) = \begin{cases} \log q & v < 1 \\ v \log q & v > 1. \end{cases} \tag{38}$$

To compute the entanglement of the unitary operator in a holographic CFTs using the line-tension picture, we need to identify the bond dimension (the local Hilbert space dimension) q in the random unitary circuit. This can be accomplished by comparing the rates at which the information gets scrambled. While the entanglement entropy grows at a rate of $\log q$ in random unitary circuits, it is known that in holographic CFTs the entanglement of the unitary operator (computed as the entanglement between two CFTs in the time-evolved thermofield double state) grows at a rate of $\frac{c\pi}{6\epsilon}$. Here, ϵ is dimensionless as it has been written in units of the lattice spacing. Therefore, we make the identification

$$q \sim e^{\frac{c\pi}{6\epsilon}}. \tag{39}$$

Notice that $\log q$ is simply equal to the entropy density given by the Cardy formula $S_{\text{Cardy}}/(2\pi R) = \frac{c\pi}{6\epsilon}$. Using this, one can correctly reproduce the growth of the entanglement in holographic CFTs, which is

$$S_U(x, y, t_1) \sim \frac{c\pi}{6\epsilon} t_1. \tag{40}$$

A. Line tension picture with inhomogenity

In the above we assumed the homogeneity and infiniteness of the space direction. Here, we describe how to generalize the line-tension picture to the situation where the spatial direction is inhomogeneous and compact, which fits the SSD time

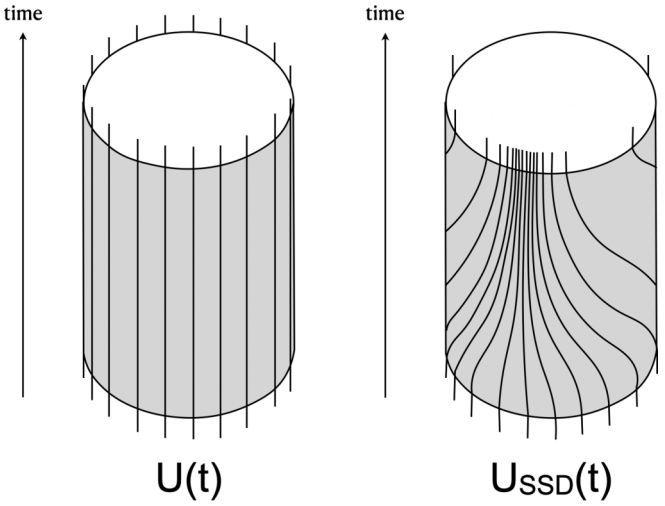

FIG. 12. SSD time evolution deforms the spacetime in the line-tension picture nonuniformly.

evolution in a compact space discussed in our paper. One can make similar arguments in the cases of other inhomogeneous Hamiltonians, and we will briefly comment on these in the last part of this section. The main idea is as follows. The aforementioned line-tension picture was based on a geometric representation of a random unitary circuit consisting of quantum gates uniformly arranged in the spatial direction. In the Schrödinger picture, the spatial direction is deformed nonuniformly by the SSD time evolution, and to give a line-tension picture that captures the dynamics of entanglement by the SSD time evolution, we should consider line-tension picture in a deformed inhomogeneous spacetime, see Fig. 12. We look for an appropriate spacetime generated by the SSD time evolution. We are especially interested in the coordinate whose metric is conformally flat. As in [31], we introduce new coordinates in which action of the SSD Hamiltonian is simple. The evolution under the SSD Hamiltonian is simplified by introducing the Poincaré coordinate $(z_P, \bar{z}_P)$. The boundary global coordinate $(w, \bar{w})$ and the boundary Poincaré coordinate $(z_P, \bar{z}_P)$ are related as

$$z_P = L \cot\left(\frac{i\pi w}{L}\right), \quad \bar{z}_P = -L \cot\left(\frac{i\pi \bar{w}}{L}\right), \tag{41}$$

where $z_P = x_P - i\tau_P$ and $\bar{z}_P = x_P + i\tau_P$ are the complex coordinates in the Poincaré coordinate. The symbol τ_P is the Euclidean time coordinate, and x_P is the spatial coordinate $(-\infty < x_P < \infty)$ in the plane where the Poincaré coordinate is defined. Notice that in this Poincaré coordinate, the two fixed points of the SSD Hamiltonian are located at the origin and the spatial infinity.

Now let us see how the Poincaré coordinate simplifies the translation under the SSD Hamiltonian. The flow of the Poincaré time is generated by the following Hamiltonian:

$$H_P = \int_{-\infty}^{\infty} dx_P T_{\tau_P \tau_P}(x_P) = -\int dz_P T(z_P) - \int d\bar{z}_P \overline{T}(\bar{z}_P). \tag{42}$$

We use the usual transformation rule for the energy-momentum tensor

$$\left(\frac{dz_P}{dw}\right)^2 T(z_P) = T(w) - \frac{c}{24\pi}\mathrm{Sch}(z_P, w) = T(w) + \frac{\pi c}{12L^2}, \tag{43}$$

with $\frac{dz_P}{dw} = -\frac{i\pi}{\sin^2(\frac{i\pi w}{L})}$, $\frac{d\bar{z}_P}{d\bar{w}} = \frac{i\pi}{\sin^2(\frac{i\pi \bar{w}}{L})}$ and move to the original global coordinate $(w, \bar{w})$ as

$$\begin{aligned} H_P &= -\oint dw\left(\frac{dw}{dz_P}\right)\left(T(w) + \frac{\pi c}{12L^2}\right) \\ &\quad - \oint d\bar{w}\left(\frac{d\bar{w}}{d\bar{z}_P}\right)\left(\overline{T}(\bar{w}) + \frac{\pi c}{12L^2}\right) \\ &= \int \frac{dx}{2\pi} 2\sin^2\left(\frac{\pi x}{L}\right) T_{\tau\tau}(x) + \frac{c}{12L} \\ &= \frac{1}{2\pi}\left(H_{\mathrm{SSD}} + \frac{c\pi}{6L}\right). \end{aligned} \tag{44}$$

Therefore, the SSD Hamiltonian generates the time flow in the Poincaré coordinate defined as (41). This indicates that the line-tension picture in the Poincaré coordinate appropriately captures the entanglement dynamics under the SSD time evolution. The metric is given by

$$ds^2 = dw d\bar{w} = \frac{dz_P d\bar{z}_P}{\pi^2\left|1 + z_P^2/L^2\right|^2}. \tag{45}$$

We propose the entanglement entropy computed in the line-tension picture in a curved spacetime with metric $g_{z\bar{z}}$ is given by the following line integral:

$$S_A = \min_{\partial\gamma_A = \partial A} \int_{\gamma_A} ds \mathcal{T}(v), \tag{46}$$

where γ_A is the curve anchored at the edges of the subregion A and homologous to A.

Specifically, using a pair of coordinates $[z(s), \bar{z}(s)]$ on the two-dimensional spacetime, we obtain

$$S_A = \min_{\partial\gamma_A = \partial A} \int_{\gamma_A} \frac{dz}{z'}\mathcal{T} + \int_{\gamma_A} \frac{d\bar{z}}{\bar{z}'}\mathcal{T}, \tag{47}$$

where $z' = dz/ds$ and $\bar{z}' = d\bar{z}/ds$.

In our case, we have a curved metric (45) with line tension (38). Let us compute the entanglement entropy by simply taking a subregion as $A = [Y_1, Y_2]$ at time t after the SSD time evolution. The entanglement: S_A^1 is given by the space-like (or light-like) curve with $\mathcal{T}(v) = \log q = \frac{c}{6\epsilon}$ as Fig. 13. Segments of the curve γ_1 and γ_2 intersects at the point $(z_P^M, \bar{z}_P^M)$. The entanglement entropy for the subregion A is computed as

$$\begin{aligned} S_A &= \int_{\gamma_2} \frac{dz}{z'}\mathcal{T} + \int_{\gamma_1} \frac{d\bar{z}}{\bar{z}'}\mathcal{T} \\ &= \frac{c}{6\epsilon}\left[\int_{z_P^M}^{iL\cot\frac{\pi Y_2}{L} - 2\pi t} \frac{dz_P}{1 + (z_P/L)^2}\right. \\ &\quad \left. + \int_{-iL\cot\frac{\pi Y_1}{L} + 2\pi t}^{\bar{z}_P^M} \frac{d\bar{z}_P}{1 + (\bar{z}_P/L)^2}\right], \end{aligned} \tag{48}$$

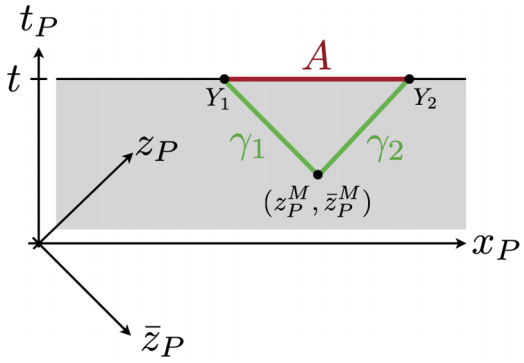

FIG. 13. Configuration of the minimal curve in the line-tension picture.

This can be simplified to the new coordinate system $(w^{\mathrm{New}}, \bar{w}^{\mathrm{New}})$ with flat metric defined by pulling the curved coordinate $(z_P, \bar{z}_P)$ back to w coordinate after the SSD (= Poincaré) time evolution [97]

$$\begin{aligned} z_P + 2\pi t &= L\cot\left(\frac{i\pi w^{\mathrm{New}}}{L}\right), \\ \bar{z}_P - 2\pi t &= L\cot\left(\frac{i\pi \bar{w}^{\mathrm{New}}}{L}\right). \end{aligned} \tag{49}$$

That is, w^{New} and $\bar{w}^{\mathrm{New}}$ are related by the original w and $\bar{w}$ as

$$\begin{aligned} w^{\mathrm{New}} &= \frac{L}{i\pi}\cot^{-1}\left[\cot\frac{i\pi w}{L} - \frac{2\pi}{L}t\right], \\ \bar{w}^{\mathrm{New}} &= \frac{L}{i\pi}\cot^{-1}\left[\cot\frac{i\pi \bar{w}}{L} + \frac{2\pi}{L}t\right]. \end{aligned} \tag{50}$$

w^{New} and $\bar{w}^{\mathrm{New}}$ are nothing but $w_{x,\epsilon}^{\mathrm{New},\alpha}$ and $\bar{w}_{x,\epsilon}^{\mathrm{New},\alpha}$ with $\alpha = 1, \epsilon = 0, \tau_0 = 0$ and $\tau_1 = it$. This can be explicitly checked by the formula $\cot^{-1}(z) = \frac{i}{2}\log[(z-i)/(z+i)]$ with $z = \cot\frac{i\pi w}{L} - \frac{2\pi}{L}t$.

Since we can treat t just as a parameter in the integral, we have $dw^{\mathrm{New}} = dw$, thus we can compute the integral as

$$\begin{aligned} S_A &= \frac{c\pi}{6\epsilon}\left[-i\int_{iX_M^{\mathrm{New}}}^{iX_{Y_2}^{\mathrm{New}}} dw^{\mathrm{New}} + i\int_{-iX_{Y_1}^{\mathrm{New}}}^{-iX_M^{\mathrm{New}}} d\bar{w}^{\mathrm{New}}\right] \\ &= \frac{c\pi}{6\epsilon}\left[X_{Y_2}^{\mathrm{New}} - X_{Y_1}^{\mathrm{New}}\right], \end{aligned} \tag{51}$$

where X_M^{New} is the intersection point $(z_P^M, \bar{z}_P^M)$ in the X^{New} coordinate. This correctly reproduces the result obtained by the holographic computations (19) in the leading order of the coarse-grained limit.

We have more interesting configurations for the entanglement entropy for double intervals A and B placed at $t = 0$ and time t respectively. Let us consider a sufficiently late time when the disconnected configuration dominates over the connected ones as Fig. 14. Two candidates for the curve that would give the entanglement entropy are drawn in Fig. 14. In the case of the uniform Hamiltonian (see the left panel in Fig. 12), if you take small enough regions, the left configuration in Fig. 14 always dominates, and we have the trivial mutual information, i.e., $S_{A\cup B} = S_A + S_B$. This is not the case for the SSD Hamiltonian. As you can see in Fig. 14, if the subregion contains the fixed point X_f^1 of the SSD

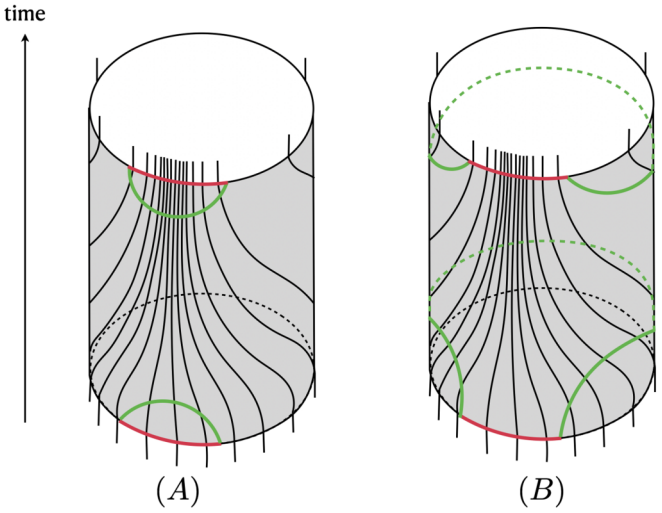

FIG. 14. Two candidates for the minimal curve that computes $S_{A\cup B}$.

Hamiltonian, the vertical lines representing "gates" originally aligned uniformly are condensed around X_f^1. The amount of the entanglement counts the number of the lines cut by the minimal curve. Therefore no matter how small a subregion is taken, at sufficiently late times, it is more efficient to take a curve like the right one in Fig. 14 that is not homologous to subregions A and B respectively (while the union of each curve is homologous to $A \cup B$) than to take the right one. Such curves give nontrivial mutual information. This is the characteristic entanglement behavior of systems driven by Hamiltonians with fixed points, such as the SSD Hamiltonian. It correctly reproduces the holographic calculations.

This prescription of the line-tension picture proposed in this section can be generalized to other inhomogeneous time evolutions. In the case of the cosine-square deformation, an appropriate coordinate system that simplifies the action of its Hamiltonian is given by the coordinate transformation

$$\tilde{z}_P = L\tan\left(\frac{i\pi w}{L}\right), \quad \bar{\tilde{z}}_P = L\tan\left(\frac{i\pi \bar{w}}{L}\right). \tag{52}$$

and the $w_\theta^{\rm New}$ and $\bar{w}_\theta^{\rm New}$ are defined as

$$\begin{aligned}\tilde{z}_P + 2\pi t &= L\tan\left(\frac{i\pi w^{\rm New}}{L}\right),\\ \bar{\tilde{z}}_P - 2\pi t &= L\tan\left(\frac{i\pi \bar{w}^{\rm New}}{L}\right).\end{aligned} \tag{53}$$

As we pointed out in [31], in the case of the general Möbius Hamiltonian, we can find an appropriate coordinate system by the coordinate transformation

$$\begin{aligned}\tan\frac{z_\theta}{2L\cosh 2\theta} &= e^{-2\theta}\cot\left(\frac{i\pi w}{L}\right),\\ \tan\frac{\bar{z}_\theta}{2L\cosh 2\theta} &= -e^{-2\theta}\cot\left(\frac{i\pi \bar{w}}{L}\right),\end{aligned} \tag{54}$$

instead of (41) in the case of the SSD Hamiltonian. The Möbius Hamiltonian generates the simple time translation in the $(z_\theta, \bar{z}_\theta)$ coordinate. The $(w_\theta^{\rm New}, \bar{w}_\theta^{\rm New})$ coordinates analogous to (48) is defined as

$$\begin{aligned}\tan\frac{z_\theta + 2\pi t}{2L\cosh 2\theta} &= e^{-2\theta}\cot\left(\frac{i\pi w_\theta^{\rm New}}{L}\right),\\ \tan\frac{\bar{z}_\theta - 2\pi t}{2L\cosh 2\theta} &= -e^{-2\theta}\cot\left(\frac{i\pi \bar{w}_\theta^{\rm New}}{L}\right),\end{aligned} \tag{55}$$

which simplifies the integral that computes the entanglement. One can check that $w_\theta^{\rm New}$ and $\bar{w}_\theta^{\rm New}$ are nothing but $w_{x,\epsilon}^{{\rm New},\alpha}$ and $\bar{w}_{x,\epsilon}^{{\rm New},\alpha}$ with $\alpha = 0$, $\epsilon = 0$ and $\tau_1 = it$.

VII. GRAVITATIONAL DESCRIPTION

Let us now turn to the gravitational dual descriptions of Setups 1, 2, and 3. As in [98,99], these dual geometries are constructed from the expectation value of energy density under the evolution by the Hamiltonians considered. Equivalently, these geometries are given by a map from the BTZ-black hole in $w_{x,\epsilon}^{\rm New}$ and $\overline{w}_{x,\epsilon}^{\rm New}$ to the time-dependent one in terms of $t_{i=0,1,2}$. The dual geometry of the reduced density matrix associated with $\mathcal{H}_2$ is a stationary BTZ-black hole. Since $\rho_{\mathcal{H}_1}$ is a mixed state, its gravity dual should be a black hole geometry. The details of the complicated metric associated with $\rho_{\mathcal{H}_1}$ are reported in Appendix E 1. Here, we describe the spacetime profile of the black hole horizon in these dual geometries. Let us introduce the radial coordinate r' that guarantees the asymptotic geometry near the AdS boundary is given by the pure AdS_3 or the modified geometry, the metric of which is given by replacing the time component of the pure AdS_3 with $g_{tt} = -4L^2 r'^2 \sin^4(\pi X/L)$. Then, the spatial and temporal dependence of the black hole horizon in the dual geometries for Setup 1 and 2 is almost the same as that in [31]. In Fig. 15, we plot the black hole horizon corresponding to Setup 3 for various t_0 and t_1 as a function of x. The spacetime dependence of the black hole horizon for Setup 4 is reported in Appendix E.

The extremes in the spatial direction of the black hole horizon for $\alpha = 2$ are given by

$$r'_{\alpha=2,{\rm Horizon}} = \frac{r_0\sqrt{L^2 + \pi^2 t_1^2}}{\left|L\cos\left(\frac{2\pi t_0}{L}\right) - \pi t_1 \sin\left(\frac{2\pi t_0}{L}\right)\right|}. \tag{56}$$

The details of the analysis on the black hole horizon are reported in Appendix E 1 a. In the large-t_1 regime, $r'_{\alpha=2,{\rm Horizon}}$ is extremized along the trajectories of the B.H.-like excitations. These extremes along these trajectories are approximated by

$$r'_{\alpha=2,{\rm Horizon}} \approx \begin{cases} \frac{r_0}{\left|\sin\left(\frac{2\pi t_0}{L}\right)\right|} & \text{for } t_0 \neq \frac{nL}{2} \\ \frac{\pi r_0 t_1}{L} & \text{for } t_0 = \frac{nL}{2} \end{cases}. \tag{57}$$

Thus, if the B.H.-like excitations are at $x \neq X_f^{i=1,2}$, then $r'_{\alpha=2,{\rm Horizon}}$ depends on only t_0, while if these excitations are at $x = X_f^{i=1,2}$, then $r'_{\alpha=2,{\rm Horizon}}$ depends on only t_1, and it linearly increases with t_1.

VIII. WORMHOLE GROWTH

In addition to the horizon, another geometrical object of our interest is a wormhole connecting the two Hilbert spaces.

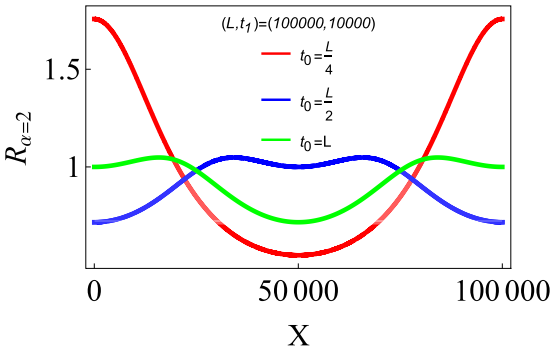

(a) Small t_1-regime.

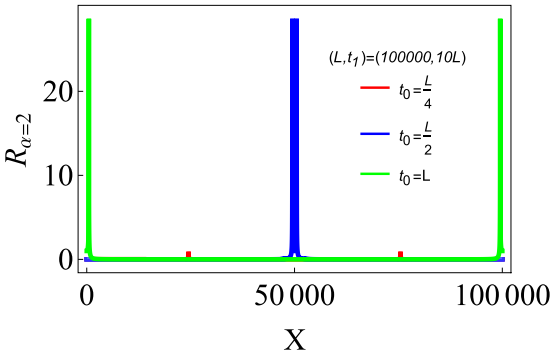

(b) Large t_1-regime.

FIG. 15. The spatial dependence of the black hole horizon for various t_1 and t_0 as a function of X. Here, $R_{\alpha=2}$ is defined by $r_{\alpha=2,\text{Horizon}}/r_0$. For the large t_1, the spatial locations where the peaks of $R_{\alpha=2}$ emerge are approximately equal to the locations of the B.H.-like excitations.

Here, as a measure of wormhole growth, we use the "free" energy defined from a two-point function as

$$F(X_1, Y_1) = -\log\left[\langle \mathcal{O}_1(Y_1)\mathcal{O}_2(X_1)\rangle\right], \tag{58}$$

where $\mathcal{O}_{i=1,2}$ are local primary operators in $\mathcal{H}_{i=1,2}$ with conformal dimension $(h_\mathcal{O}, h_\mathcal{O})$. In the Heisenberg picture, this free energy is given by the universal and nonuniversal pieces as

$$F(X_1, Y_1) = -h_\mathcal{O}\log\left[\frac{dw^{\text{New}}_{Y_1,\epsilon}}{dw_{Y_1}}\frac{d\overline{w}^{\text{New}}_{Y_1,\epsilon}}{d\overline{w}_{Y_1}}\right] + 2h_\mathcal{O}G(X_1, Y_1). \tag{59}$$

Here, we consider light operators with $c \gg h_\mathcal{O} \gg 1$. In this regime, the nonuniversal piece G is determined by the length of geodesics in the stationary BTZ black hole.

A. Setup 1

Let us begin by analyzing the free energy in (59) for Setup 1. We consider the t_1 dependence of (59) with general Y_1. We assume that $\frac{L}{2} > X_1 > Y_1 > 0$. Under the evolution by $H^1_{\text{Möbius}}$ with $\theta \neq \infty$, the imaginary parts of $w^{\text{New}}_{Y_1,\epsilon}$ and $\overline{w}^{\text{New}}_{Y_1,\epsilon}$ of (59) monotonically increase with t_1. In the large-t_1 regime, $F(X_1, Y_1)$ is approximately given by a monotonically increasing function of t_1,

$$F(X_1, Y_1) \approx \frac{h_\mathcal{O}\pi}{\epsilon}\left(\text{Im}\left[w^{\text{New}}_{Y_1,\epsilon}\right] + \text{Im}\left[\bar{w}^{\text{New}}_{Y_1,\epsilon}\right]\right) + 4h_\mathcal{O}\log\left(\frac{2\epsilon}{\pi}\right). \tag{60}$$

In small-t_1 regime where $0 > \text{Im}\,[w^{\text{New}}_{Y_1,\epsilon}] - X_1 > -X_1$, $L > \text{Im}\,[\overline{w}^{\text{New}}_{Y_1,\epsilon}] > 0$, and $\frac{L}{2} > X_1 - X^{\text{New}}_{Y_1,\epsilon}$, $F(X_1, Y_1)$ is approximately given by a function following the trajectory of the local operator,

$$F(X_1, Y_1) \approx \frac{h_\mathcal{O}\pi\left(X_1 - X^{\text{New}}_{Y_1,\epsilon}\right)}{\epsilon} + 4h_\mathcal{O}\log\left(\frac{2\epsilon}{\pi}\right). \tag{61}$$

In this t_1 regime, $F(X_1, Y_1)$ may decrease with t_1.

In the SSD limit $\theta \to \infty$, if $Y_1 = 0$, $F(Y_1 = 0, X_1)$ is a stationary constant, and approximated as $F(Y_1 = 0, X_1) \approx \frac{h_\mathcal{O}\pi X_1}{\epsilon}$. Unless $Y_1 = 0$, for large t_1, the imaginary parts of $w^{\text{New}}_{Y_1,\epsilon}$ and $\bar{w}^{\text{New}}_{Y_1,\epsilon}$ reduce to $\text{Im}\,[w^{\text{New}}_{Y_1,\epsilon}] \approx L$ and $\text{Im}\,[\overline{w}^{\text{New}}_{Y_1,\epsilon}] \approx 0$. Consequently, the t_1 dependence of $F(X_1, Y_1)$ in this limit is approximated by

$$F(X_1, Y_1) \approx 4h_\mathcal{O}\log\left[\frac{2\pi t_1}{L}\sin\left(\frac{\pi Y_1}{L}\right)\right] + \frac{\pi h_\mathcal{O} L}{\epsilon} + 4h_\mathcal{O}\log\left(\frac{2\epsilon}{\pi}\right). \tag{62}$$

Thus, $F(X_1, Y_1)$ is approximately stationary except for the logarithmic growth with t_1.

From these analyses, we can see that Möbius/SS deformation may prevent the wormhole from growing with t_1. In Fig. 16, we plot $F(X_1, Y_1)$ in Setup 1 as a function of t_1. We can see for larger θ, the growth of $F(X_1, Y_1)$ is slower.

B. Setup 2

In Setup 2, $F(X_1, Y_1)$ grows linearly with t_0 under the evolution by H^1, and then grows with t_1 under the evolution by $H^1_{\text{Möbius}}$ as in the previous section.

C. Setup 3

Let turn to the analysis on $F(X_1, Y_1)$ in Setup 3. We, as before, assume $\frac{L}{2} > X_1 > Y_1 > 0$. As in Setup 1, for various t_1, the imaginary parts of $w^{\text{New}}_{Y_1,\epsilon}$ and $\overline{w}^{\text{New}}_{Y_1,\epsilon}$ of (59) monotonically increase with t_0. Therefore, the early time behavior of $F(X_1, Y_1)$ may be approximated by (61), while the late-time t_0 dependence is approximated by (60). For large t_1, the t_0 dependence of $F(X_1, Y_1)$ is given by the asymptotic form,

$$\begin{aligned} &F(X_1, Y_1) \\ &\approx 4h_\mathcal{O}\log\left(\frac{2\epsilon}{\pi}\right) + h_\mathcal{O}\log\left[\frac{16\pi^4 t_1^4}{L^4}\sin^2\left(\frac{\pi(t_0 - Y_1)}{L}\right)\right. \\ &\quad \left.\times \sin^2\left(\frac{\pi(t_0 + Y_1)}{L}\right)\right] \\ &\quad + \begin{cases} \frac{\pi h_\mathcal{O}(2m+1)L}{\epsilon}, & mL + Y_1 > t_0 > mL - Y_1 \\ \frac{2\pi h_\mathcal{O}(m+1)L}{\epsilon}, & (m+1)L - Y_1 > t_0 > mL + Y_1 \end{cases}, \end{aligned} \tag{63}$$

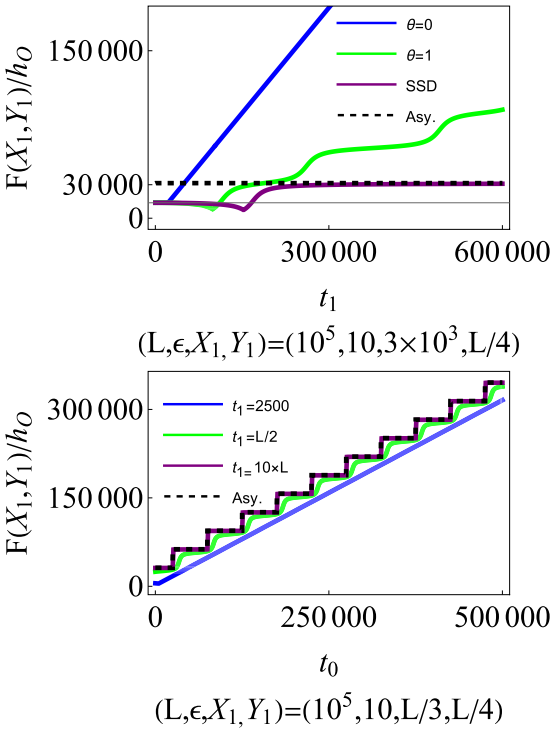

FIG. 16. (Top) The t_1 dependence of $F(X_1, Y_1)$ for various θ in Setup 1. The dashed line illustrates the t_1 dependence of $F(X_1, Y_1)/h_{\mathcal{O}}$ in (62). (Bottom) The t_1 dependence of $F(X_1, Y_1)$ for various t_1 in Setup 3. The dashed line illustrates the asymptotic behavior of $F(X_1, Y_1)/h_{\mathcal{O}}$ in (63).

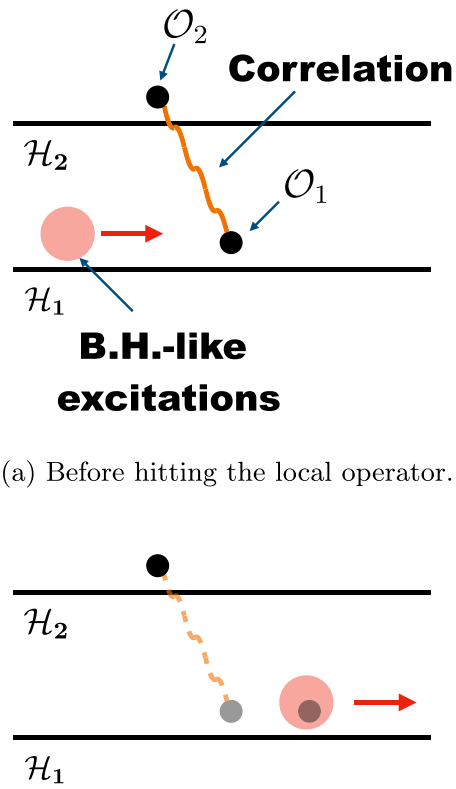

(a) Before hitting the local operator.

(b) After hitting the local operator.

FIG. 17. The destruction of the nonlocal correlation between $\mathcal{O}_1$ and $\mathcal{O}_2$ by the B.H.-like excitations.

where m is an integer. In Fig. 16, we plot $F(X_1, Y_1)$ of Setup 3 for various t_1 as a function of t_0. We can see that for larger t_1, $F(X_1, Y_1)$ is not given by the simple linear growth, but approximated by a sequence of step functions.

The asymptotic behavior (63) can be interpreted by using the description in Sec. V B 1. For large t_1, at $t_0 = 0$, two B.H.-like excitations emerge near $x = X_f^1$ and move towards the left and right at the speed of light under the evolution by H^1 (Fig. 17). Here, we assume that the size of these excitations is $\mathcal{O}(\epsilon)$. Then, in the coarse-grained region, these excitations are approximated as the local excitations. Recall that we have operators $\mathcal{O}_{i=1,2}$ on $\mathcal{H}_{i=1,2}$ that are inserted as at Y_1 and X_1, respectively. At $t_0 \approx mL \pm Y_1$ where m is an integer, the left- and right-moving B.H.-like excitations hit $\mathcal{O}_1$, and simultaneously the information about $\mathcal{O}_1$ is scrambled in the interior of the B.H.-like excitations. As a consequence, the correlation between $\mathcal{O}_1$ and $\mathcal{O}_2$ is weakened each time these B.H.-like excitations pass $\mathcal{O}_1$. The information about $\mathcal{O}_1$ may be delocalized and encoded in these B.H.-like excitations.

IX. DISCUSSIONS AND FUTURE DIRECTIONS

In this paper, we studied three quantum quench processes with the inhomogeneously deformed Hamiltonians in 2d CFT. Of particular interest for us is interested in the interplay between inhomogeneous deformation and quantum information scrambling. With these setups, we discussed the operator entanglement, the recovery of quantum information, and the dynamics of B.H.-like excitations. As mentioned in Ref. [31], these inhomogeneously deformed Hamiltonians may be engineered both in digital and analog quantum simulators, such as cold atoms and Rydberg atoms. Simulating our quench processes in these systems opens up the possibility of studying quantum aspects of black holes in the laboratory. In particular, from the findings in our paper, among others, it would be interesting to look into the following aspects:

(i) *Quantum black hole.* The t_0 dependence of the correlation function may be described by the propagation of the B.H.-like excitation (see Sec. VIII C). In the frame where one of the B.H.-like excitations is stationary, a local operator falls into and is radiated from this excitation. As in [55], this excitation has the almost same amount of entropy as the black hole and its interior may have a strong scrambling effect. Therefore, if we can create these excitations in the experimental systems, then we may simulate the dynamics of black holes in the laboratories.

(ii) *Genuine tripartite entanglement.* Let us consider the application of the genuine tripartite entanglement obtained in this paper. In 2d holographic CFTs, for the large-t_1 regime, the local BMI is approximately zero, while the global BMI can be $\mathcal{O}(\frac{1}{\epsilon})$ in the certain t_1 intervals (see Sec. V B 3). One possible

interpretation for this entanglement property of the steady state is that in the t_1 regime where only $I_{A,B_1\cup B_2}$ is $\mathcal{O}(\frac{1}{\epsilon})$, three persons belonging to A, B_1, and B_2, respectively, may be able to share the quantum information, while only two of them may not. In the other words, without the cooperation of these three people, they may never get the quantum information correctly. This entanglement property may be applied to secure quantum communications.

Finally, we conclude by listings some of the future directions:

(i) *Multipartite entanglement*. It would be interesting to create a system where the local MI is effectively zero, while the global BMI that is shared by $n(>3)$-parties is $\mathcal{O}(\frac{1}{\epsilon})$. If the number of fixed points increases [35], then the number of parties sharing the global BMI might increase.

(ii) *Quantum scars*. In this paper, we discovered the systems, which are not evolved to the typical state with a $2d$ homogeneous holographic Hamiltonian. These states may be interpreted as quantum scar states. It would be interesting to establish the relationship between these states considered in this paper and the quantum scar states [100–108].

ACKNOWLEDGMENTS

K.G. is supported by JSPS KAKENHI Grant-in-Aid for Early-Career Scientists (Grant No. 21K13930)and Research Fellowships of Japan Society for the Promotion of Science for Young Scientists (Grant No. 22J00663). M.N. is supported by funds from the University of Chinese Academy of Sciences (UCAS), funds from the Kavli Institute for Theoretical Sciences (KITS). S.R. is supported by the National Science Foundation under Award No. DMR-2001181, and by a Simons Investigator Grant from the Simons Foundation (Award No. 566116). This work is supported by the Gordon and Betty Moore Foundation through Grant GBMF8685 toward the Princeton theory program. K.T. is supported by JSPS KAKENHI Grant No. 21K13920 and MEXT KAKENHI Grant No. 22H05265. This material is based upon work supported by the National Science Foundation under Grant No. NSF-DMR 2018358 and by an appointment to the YST Program at the APCTP through the Science and Technology Promotion Fund and Lottery Fund of the Korean Government, as well as the Korean Local Governments - Gyeongsangbuk-do Province and Pohang City (M.T.T.).

APPENDIX A: EVOLUTION OF OPERATORS INDUCED BY $U^1_{E,\alpha}e^{-\epsilon H}$

The Euclidean time-evolution operators considered in the main text and Appendices are [see (13) and (8)]

$$U_E^1=\begin{cases} e^{-H^1_{\text{Möbius}}\tau_1} & \alpha=0\\ e^{-H^1_{\text{SSD}}\tau_1}e^{-H^1_0\tau_0} & \alpha=1\\ e^{-H^1_0\tau_0}e^{-H^1_{\text{SSD}}\tau_1} & \alpha=2\\ e^{-H^1_{\text{CSD}}\tau_2}e^{-H^1_{\text{SSD}}\tau_1} & \alpha=3\end{cases},\quad \tilde{U}_E^1=\begin{cases} e^{H^1_{\text{Möbius}}\tau_1} & \alpha=0\\ e^{H^1_0\tau_0}e^{H^1_{\text{SSD}}\tau_1} & \alpha=1\\ e^{H^1_{\text{SSD}}\tau_1}e^{H^1_0\tau_0} & \alpha=2\\ e^{H^1_{\text{SSD}}\tau_1}e^{H^1_{\text{CSD}}\tau_2} & \alpha=3\end{cases}. \tag{A1}$$

In these appendices, we use the index $\alpha=0,1,2,3$ to distinguish these cases. The new complex variables $(w^{\text{New},\alpha}_{x,\epsilon}, \overline{w}^{\text{New},\alpha}_{x,\epsilon})$ in (17) are given by

$$\begin{aligned}
w^{\text{New},0}_{x,\epsilon}&=\epsilon+\frac{L}{2\pi}\log\left[\frac{[(1-\lambda_1)\cosh(2\theta)-(\lambda_1+1)]z_x+(\lambda_1-1)\sinh(2\theta)}{(1-\lambda_1)\sinh(2\theta)z_x+[(\lambda_1-1)\cosh(2\theta)-(\lambda_1+1)]}\right],\\
\bar{w}^{\text{New},0}_{x,\epsilon}&=\epsilon+\frac{L}{2\pi}\log\left[\frac{[(1-\lambda_1)\cosh(2\theta)-(\lambda_1+1)]\bar{z}_x+(\lambda_1-1)\sinh(2\theta)}{(1-\lambda_1)\sinh(2\theta)\bar{z}_x+[(\lambda_1-1)\cosh(2\theta)-(\lambda_1+1)]}\right],\\
w^{\text{New},1}_{x,\epsilon}&=\epsilon+\tau_0+\frac{L}{2\pi}\log\left[\frac{\pi\tau_1(1-z_x)-Lz_x}{\pi\tau_1(1-z_x)-L}\right],\\
\overline{w}^{\text{New},1}_{x,\epsilon}&=\epsilon+\tau_0+\frac{L}{2\pi}\log\left[\frac{\pi\tau_1(1-\bar{z}_x)-L\bar{z}_x}{\pi\tau_1(1-\bar{z}_x)-L}\right],\\
w^{\text{New},2}_{x,\epsilon}&=\epsilon+\frac{L}{2\pi}\log\left[\frac{\pi\tau_1(1-e^{\frac{2\pi\tau_0}{L}}z_x)-e^{\frac{2\pi\tau_0}{L}}Lz_x}{\pi\tau_1(1-e^{\frac{2\pi\tau_0}{L}}z_x)-L}\right],\\
\overline{w}^{\text{New},2}_{x,\epsilon}&=\epsilon+\frac{L}{2\pi}\log\left[\frac{\pi\tau_1(1-e^{\frac{2\pi\tau_0}{L}}\bar{z}_x)-e^{\frac{2\pi\tau_0}{L}}L\bar{z}_x}{\pi\tau_1(1-e^{\frac{2\pi\tau_0}{L}}\bar{z}_x)-L}\right],\\
w^{\text{New},3}_{x,\epsilon}&=\epsilon+\frac{L}{2\pi}\log\left[\frac{z_x(L^2+\pi L(\tau_1+\tau_2)+2\pi^2\tau_1\tau_2)+\pi(L(\tau_2-\tau_1)+2\pi\tau_1\tau_2)}{L^2-\pi L\tau_1-\pi L\tau_2+\pi z_x(L(\tau_1-\tau_2)+2\pi\tau_1\tau_2)+2\pi^2\tau_1\tau_2}\right],\\
\overline{w}^{\text{New},3}_{x,\epsilon}&=\epsilon+\frac{L}{2\pi}\log\left[\frac{\bar{z}_x(L^2+\pi L(\tau_1+\tau_2)+2\pi^2\tau_1\tau_2)+\pi(L(\tau_2-\tau_1)+2\pi\tau_1\tau_2)}{L^2-\pi L\tau_1-\pi L\tau_2+\pi\bar{z}_x(L(\tau_1-\tau_2)+2\pi\tau_1\tau_2)+2\pi^2\tau_1\tau_2}\right],
\end{aligned} \tag{A2}$$

where the variables and parameters, z, $\bar{z}$, and λ_1, are defined by

$$z_x = e^{\frac{2\pi w_x}{L}}, \quad \bar{z}_x = e^{\frac{2\pi \overline{w}_x}{L}}, \quad \lambda_1 = \exp\left(\frac{2\pi\tau_1}{L\cosh(2\theta)}\right). \tag{A3}$$

1. Real-time evolution of operators

After the analytic continuation, $\tau_{i=0,1,2} = it_{i=0,1,2}$, only the imaginary parts of $w^{\mathrm{New},\alpha}_{x,\epsilon}$ and $\overline{w}^{\mathrm{New},\alpha}_{x,\epsilon}$ depend on $t_{i=0,1,2}$. The dependence of $w^{\mathrm{New},\alpha}_{x,\epsilon}$ and $\overline{w}^{\mathrm{New},\alpha}_{x,\epsilon}$ on $t_{i=0,1,2}$ is given by

$$\begin{aligned}
w^{\mathrm{New},0}_{x,\epsilon} &= \epsilon + i\frac{L\varphi_{x,0}}{\pi}, \quad \overline{w}^{\mathrm{New},0}_{x,\epsilon} = \epsilon + i\frac{L\overline{\varphi}_{x,0}}{\pi},\\
w^{\mathrm{New},1}_{x,\epsilon} &= \epsilon + it_0 + i\frac{L\varphi_{x,1}}{\pi}, \quad \overline{w}^{\mathrm{New},1}_{x,\epsilon} = \epsilon + it_0 + \frac{L\overline{\varphi}_{x,1}}{\pi},\\
w^{\mathrm{New},2}_{x,\epsilon} &= \epsilon + i\frac{L\varphi_{x,2}}{\pi}, \quad \overline{w}^{\mathrm{New},2}_{x,\epsilon} = \epsilon + i\frac{L\overline{\varphi}_{x,2}}{\pi},\\
w^{\mathrm{New},3}_{x,\epsilon} &= \epsilon + i\frac{L\varphi_{x,3}}{\pi}, \quad \overline{w}^{\mathrm{New},3}_{x,\epsilon} = \epsilon + i\frac{L\overline{\varphi}_{x,3}}{\pi},
\end{aligned} \tag{A4}$$

where the variables, $\varphi_{x,\alpha}$, $\overline{\varphi}_{x,\alpha}$, $r_{x,\alpha}$, and $\overline{r}_{x,\alpha}$, are defined by

$$\begin{aligned}
r_{x,0} &= \left[\left(-\cos\left(\frac{\pi t_1}{L\cosh 2\theta}\right)\cos\left(\frac{\pi x}{L}\right) + \sin\left(\frac{\pi t_1}{L\cosh 2\theta}\right)\sin\left(\frac{\pi x}{L}\right)e^{2\theta}\right)^2\right.\\
&\quad \left.+\left(\cos\left(\frac{\pi t_1}{L\cosh 2\theta}\right)\sin\left(\frac{\pi x}{L}\right) + \sin\left(\frac{\pi t_1}{L\cosh 2\theta}\right)\cos\left(\frac{\pi x}{L}\right)e^{-2\theta}\right)^2\right]^{\frac{1}{2}},\\
\cos\varphi_{x,0} &= \frac{\cos\left(\frac{\pi t_1}{L\cosh 2\theta}\right)\cos\left(\frac{\pi x}{L}\right) - \sin\left(\frac{\pi t_1}{L\cosh 2\theta}\right)\sin\left(\frac{\pi x}{L}\right)e^{2\theta}}{r_{x,0}},\\
\sin\varphi_{x,0} &= \frac{\cos\left(\frac{\pi t_1}{L\cosh 2\theta}\right)\sin\left(\frac{\pi x}{L}\right) + \sin\left(\frac{\pi t_1}{L\cosh 2\theta}\right)\cos\left(\frac{\pi x}{L}\right)e^{-2\theta}}{r_{x,0}},\\
\overline{r}_{x,0} &= \left[\left(\cos\left(\frac{\pi t_1}{L\cosh 2\theta}\right)\cos\left(\frac{\pi x}{L}\right) + \sin\left(\frac{\pi t_1}{L\cosh 2\theta}\right)\sin\left(\frac{\pi x}{L}\right)e^{2\theta}\right)^2\right.\\
&\quad \left.+\left(\cos\left(\frac{\pi t_1}{L\cosh 2\theta}\right)\sin\left(\frac{\pi x}{L}\right) - \sin\left(\frac{\pi t_1}{L\cosh 2\theta}\right)\cos\left(\frac{\pi x}{L}\right)e^{-2\theta}\right)^2\right]^{\frac{1}{2}},\\
\cos\overline{\varphi}_{x,0} &= \frac{\cos\left(\frac{\pi t_1}{L\cosh 2\theta}\right)\cos\left(\frac{\pi x}{L}\right) + \sin\left(\frac{\pi t_1}{L\cosh 2\theta}\right)\sin\left(\frac{\pi x}{L}\right)e^{2\theta}}{\overline{r}_{x,0}},\\
\sin\overline{\varphi}_{x,0} &= \frac{-\cos\left(\frac{\pi t_1}{L\cosh 2\theta}\right)\sin\left(\frac{\pi x}{L}\right) + \sin\left(\frac{\pi t_1}{L\cosh 2\theta}\right)\cos\left(\frac{\pi x}{L}\right)e^{-2\theta}}{\overline{r}_{x,0}},
\end{aligned} \tag{A5}$$

$$\begin{aligned}
r_{x,2} &= \sqrt{4\pi^2 t_1^2\sin^2\left(\frac{\pi(t_0+x)}{L}\right) - 4\pi L t_1\sin\left(\frac{\pi(t_0+x)}{L}\right)\cos\left(\frac{\pi(t_0+x)}{L}\right) + L^2},\\
\cos\varphi_{x,2} &= \frac{-2\pi t_1\sin\left(\frac{\pi(t_0+x)}{L}\right) + L\cos\left(\frac{\pi(t_0+x)}{L}\right)}{r_{x,2}}, \quad \sin\varphi_{x,2} = \frac{L\sin\left(\frac{\pi(t_0+x)}{L}\right)}{r_{x,2}}.\\
\overline{r}_{x,2} &= \sqrt{4\pi^2 t_1^2\sin^2\left(\frac{\pi(t_0-x)}{L}\right) - 4\pi L t_1\sin\left(\frac{\pi(t_0-x)}{L}\right)\cos\left(\frac{\pi(t_0-x)}{L}\right) + L^2},\\
\cos\overline{\varphi}_{x,2} &= -\frac{2\pi t_1\sin\left(\frac{\pi(t_0-x)}{L}\right) - L\cos\left(\frac{\pi(t_0-x)}{L}\right)}{\overline{r}^1_x}, \quad \sin\overline{\varphi}_{x,2} = \frac{L\sin\left(\frac{\pi(t_0-x)}{L}\right)}{\overline{r}_{x,2}},\\
\varphi_{x,1} &= \varphi_{x,2}|_{t_0=0}, \quad \overline{\varphi}_{x,1} = \overline{\varphi}_{x,2}|_{t_0=0},
\end{aligned} \tag{A6}$$

$$
\begin{aligned}
r_{x,3} &= \left[\left((L^2-4\pi^2 t_1 t_2)\cos\left(\frac{\pi x}{L}\right)-2\pi L t_1 \sin\left(\frac{\pi x}{L}\right)\right)^2+\left(L^2\sin\left(\frac{\pi x}{L}\right)+2\pi L t_2\cos\left(\frac{\pi x}{L}\right)\right)^2\right]^{\frac{1}{2}},\\
\bar{r}_{x,3} &= \left[\left((L^2-4\pi^2 t_1 t_2)\cos\left(\frac{\pi x}{L}\right)+2\pi L t_1 \sin\left(\frac{\pi x}{L}\right)\right)^2+\left(-L^2\sin\left(\frac{\pi x}{L}\right)+2\pi L t_2\cos\left(\frac{\pi x}{L}\right)\right)^2\right]^{\frac{1}{2}},\\
\cos\varphi_{x,3} &= \frac{1}{r_{x,3}}\left[(L^2-4\pi^2 t_1 t_2)\cos\left(\frac{\pi x}{L}\right)-2\pi L t_1\sin\left(\frac{\pi x}{L}\right)\right],\\
\sin\varphi_{x,3} &= \frac{2\pi L\cos\left(\frac{\pi x}{L}\right)}{r_{x,3}}\left[t_2+\frac{L}{2\pi}\tan\left(\frac{\pi x}{L}\right)\right],\\
\cos\overline{\varphi}_{x,3} &= \frac{1}{\bar{r}_{x,3}}\left[(L^2-4\pi^2 t_1 t_2)\cos\left(\frac{\pi x}{L}\right)+2\pi L t_1\sin\left(\frac{\pi x}{L}\right)\right],\\
\sin\overline{\varphi}_{x,3} &= \frac{2\pi L\cos\left(\frac{\pi x}{L}\right)}{\bar{r}_{x,3}}\left[t_2-\frac{L}{2\pi}\tan\left(\frac{\pi x}{L}\right)\right].
\end{aligned}
\tag{A7}
$$

APPENDIX B: THE DETAILS OF CALCULATIONS AND RESULTS IN 2D HOLOGRAPHIC CFTs

Let us present the details of the calculations and results in 2d holographic CFTs.

1. Nonuniversal piece of OEE in 2d holographic CFTs

We now present the details of the nonuniversal pieces, $S_{\rm dis}$ and $S_{\rm con}$, of the entanglement entropy. Let us concentrate on $S_{\rm dis}$. This nonuniversal piece $S_{\rm dis}$ is given by

$$
S_{\rm dis} = {\rm Min}\left[S^1_{\rm dis}, S^{2,\pm}_{\rm dis}, S^{3,\pm}_{\rm dis}, S^{4,\pm}_{\rm dis}\right],
\tag{B1}
$$

where $\tilde{S}^i_{\rm dis}$ are defined by

$$
\begin{aligned}
\tilde{S}^1_{\rm dis} &= \frac{c}{6}\log\left[\left|\sin\left[\frac{\pi}{2\epsilon}\left(w^{{\rm New},\alpha}_{Y_1,\epsilon}-w^{{\rm New},\alpha}_{Y_2,\epsilon}\right)\right]\right|^2\left|\sin\left[\frac{\pi}{2\epsilon}\left(w_{X_1}-w_{X_2}\right)\right]\right|^2\right],\\
\tilde{S}^{2,\pm}_{\rm dis} &= \frac{c}{6}\log\left[\left|\sin\left[\frac{\pi}{2\epsilon}\left(\pm iL-\left(w^{{\rm New},\alpha}_{Y_1,\epsilon}-w^{{\rm New},\alpha}_{Y_2,\epsilon}\right)\right)\right]\right|^2\left|\sin\left[\frac{\pi}{2\epsilon}\left(\pm iL-\left(w_{X_1}-w_{X_2}\right)\right)\right]\right|^2\right],\\
\tilde{S}^{3,\pm}_{\rm dis} &= \frac{c}{6}\log\left[\left|\sin\left[\frac{\pi}{2\epsilon}\left(w^{{\rm New},\alpha}_{Y_1,\epsilon}-w^{{\rm New},\alpha}_{Y_2,\epsilon}\right)\right]\right|^2\left|\sin\left[\frac{\pi}{2\epsilon}\left(\pm iL-\left(w_{X_1}-w_{X_2}\right)\right)\right]\right|^2\right],\\
\tilde{S}^{4,\pm}_{\rm dis} &= \frac{c}{6}\log\left[\left|\sin\left[\frac{\pi}{2\epsilon}\left(\pm iL-\left(w^{{\rm New},\alpha}_{Y_1,\epsilon}-w^{{\rm New},\alpha}_{Y_2,\epsilon}\right)\right)\right]\right|^2\left|\sin\left[\frac{\pi}{2\epsilon}\left(w_{X_1}-w_{X_2}\right)\right]\right|^2\right]
\end{aligned}
\tag{B2}
$$

Then, let us turn to $S_{\rm con}$. This contribution from the geodesics connecting the endpoints of the subsystems on the different Euclidean time slices is given by

$$
S_{\rm con} = {\rm Min}\left[\tilde{S}^1_{\rm con}, \tilde{S}^{2,\pm}_{\rm con}, \tilde{S}^{3,\pm}_{\rm con}, \tilde{S}^{4,\pm}_{\rm con}\right]
\tag{B3}
$$

where $\tilde{S}^i_{\rm con}$ are defined by

$$
\begin{aligned}
\tilde{S}^1_{\rm con} &= \frac{c}{6}\log\left[\left|\sin\left[\frac{\pi}{2\epsilon}\left(w^{{\rm New},\alpha}_{Y_1,\epsilon}-w_{X_1}\right)\right]\right|^2\left|\sin\left[\frac{\pi}{2\epsilon}\left(w^{{\rm New},\alpha}_{Y_2,\epsilon}-w_{X_2}\right)\right]\right|^2\right],\\
\tilde{S}^{2,\pm}_{\rm con} &= \frac{c}{6}\log\left[\left|\sin\left[\frac{\pi}{2\epsilon}\left(\pm iL-\left(w^{{\rm New},\alpha}_{Y_1,\epsilon}-w_{X_1}\right)\right)\right]\right|^2\left|\sin\left[\frac{\pi}{2\epsilon}\left(\pm iL-\left(w^{{\rm New},\alpha}_{Y_2,\epsilon}-w_{X_2}\right)\right)\right]\right|^2\right],\\
\tilde{S}^{3,\pm}_{\rm con} &= \frac{c}{6}\log\left[\left|\sin\left[\frac{\pi}{2\epsilon}\left(w^{{\rm New},\alpha}_{Y_1,\epsilon}-w_{X_1}\right)\right]\right|^2\left|\sin\left[\frac{\pi}{2\epsilon}\left(\pm iL-\left(w^{{\rm New},\alpha}_{Y_2,\epsilon}-w_{X_2}\right)\right)\right]\right|^2\right],\\
\tilde{S}^{4,\pm}_{\rm con} &= \frac{c}{6}\log\left[\left|\sin\left[\frac{\pi}{2\epsilon}\left(\pm iL-\left(w^{{\rm New},\alpha}_{Y_1,\epsilon}-w_{X_1}\right)\right)\right]\right|^2\left|\sin\left[\frac{\pi}{2\epsilon}\left(w^{{\rm New},\alpha}_{Y_2,\epsilon}-w_{X_2}\right)\right]\right|^2\right].
\end{aligned}
\tag{B4}
$$

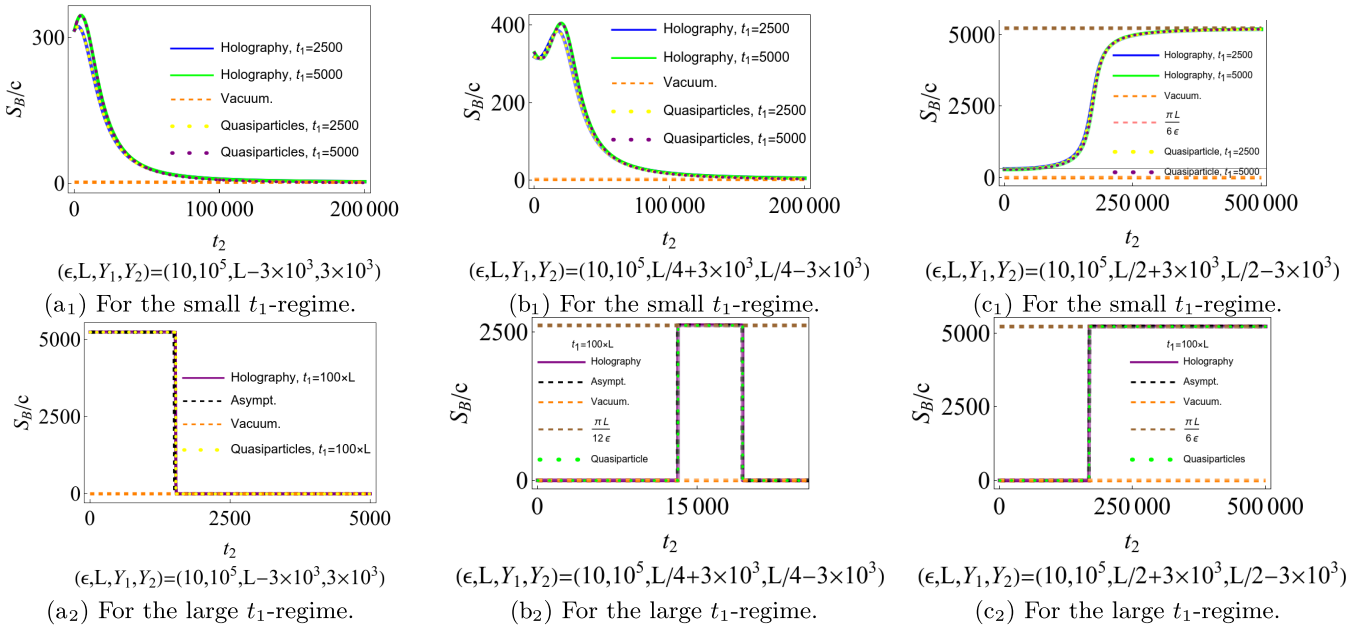

FIG. 18. The entanglement entropy S_B for various t_1 as the function of t_2. The panels $(a_{i=1,2})$ show the t_2 dependence of S_B for case (a), (b_i) show the one for (b), and (c_i) show the one for (c). In the top panels, we show the t_2 dependence of S_B for the small-t_1 regime, while in the bottom panels, we show the t_2 dependence of S_B for the large-t_1 regime. The black dashed line illustrates the asymptotic behavior of S_B in (C1) in the large-t_1 limit. The orange, brown, and dashed lines illustrate the entanglement entropy for the vacuum state, thermal entropy, and half of it, respectively.

2. The definition of θ_C

Here, we describe the definition of θ_C that is introduced in Sec. III A 1. Let B be a subsystem including X_f^1 of $\mathcal{H}_1$, and also let A be a subsystem including the origin of $\mathcal{H}_2$. Furthermore, let us assume that $S_{\rm dis}$ for the small t_1 is given by

$$S_{\rm dis}=\frac{c\pi}{6\epsilon}\left[2L-\left(X_{Y_1,\epsilon}^{{\rm New},\alpha=1}-X_{Y_2,\epsilon}^{{\rm New},\alpha=1}+(X_1-X_2)\right)\right] \tag{B5}$$

The time for (B5) to be maximized is determined by $\partial_{t_1}[-(X_{Y_1,\epsilon}^{{\rm New},\alpha=1}-X_{Y_2,\epsilon}^{{\rm New},\alpha=1})]=0$. Let $t_{1,{\rm Max}}$ denote this time, and this time depends on θ, Y_1, Y_2, and L. Let us define θ_C as the θ satisfying $(X_{Y_1,\epsilon}^{{\rm New},\alpha=1}-X_{Y_2,\epsilon}^{{\rm New},\alpha=1})=L-(X_1-X_2)=l_A$ at $t=t_{1,{\rm Max}}$.

APPENDIX C: THE ENTANGLEMENT DYNAMICS FOR (8)

1. The t_2 dependence of entanglement entropy

Let us consider the state (8). We report the t_2 dependence of entanglement entropy of (8). for the subsystems considered in Sec. V A. In Fig. 18, we depict S_B for various t_1 as a function of t_2. In the t_1 limit, the t_2 dependence of S_B is approximated by

$$\text{If } x=X_f^1\in B,\quad S_B\approx\begin{cases}\frac{c\pi L}{6\epsilon} & \text{for}\\ ;\ \frac{L}{2\pi}\left|\tan\left(\frac{\pi Y_2}{L}\right)\right|>t_2>0 & \\ \frac{c\pi L}{12\epsilon} & \text{for } \frac{L}{2\pi}\left|\tan\left(\frac{\pi Y_1}{L}\right)\right|>t_2>\frac{L}{2\pi}\left|\tan\left(\frac{\pi Y_2}{L}\right)\right|,\\ \frac{c}{3}\log\left[\sin\left[\frac{\pi(Y_1-Y_2)}{L}\right]\right] & \text{for } t_2>\left|\frac{L}{2\pi}\tan\left(\frac{\pi Y_1}{L}\right)\right|\end{cases}$$

$$\text{If } \frac{L}{2}>Y_1>x>Y_2>0,\quad S_B\approx\begin{cases}\frac{c}{3}\log\left[\sin\left[\frac{\pi(Y_1-Y_2)}{L}\right]\right] & \text{for } \frac{L}{2\pi}\left|\tan\left(\frac{\pi Y_2}{L}\right)\right|>t_2>0\\ \frac{c\pi L}{12\epsilon} & \text{for } \frac{L}{2\pi}\left|\tan\left(\frac{\pi Y_1}{L}\right)\right|>t_2>\frac{L}{2\pi}\left|\tan\left(\frac{\pi Y_2}{L}\right)\right|,\\ \frac{c}{3}\log\left[\sin\left[\frac{\pi(Y_1-Y_2)}{L}\right]\right] & \text{for } t_2>\frac{L}{2\pi}\left|\tan\left(\frac{\pi Y_1}{L}\right)\right|\end{cases}$$

$$\text{If } x=X_f^2\in B,\quad S_B\approx\begin{cases}\frac{c}{3}\log\left[\sin\left[\frac{\pi(Y_1-Y_2)}{L}\right]\right] & \text{for } \frac{L}{2\pi}\left|\tan\left(\frac{\pi Y_2}{L}\right)\right|>t_2>0\\ \frac{c\pi L}{12\epsilon} & \text{for } \frac{L}{2\pi}\left|\tan\left(\frac{\pi Y_1}{L}\right)\right|>t_2>\frac{L}{2\pi}\left|\tan\left(\frac{\pi Y_2}{L}\right)\right|,\\ \frac{c\pi L}{6\epsilon} & \text{for } t_2>\frac{L}{2\pi}\left|\tan\left(\frac{\pi Y_1}{L}\right)\right|\end{cases} \tag{C1}$$

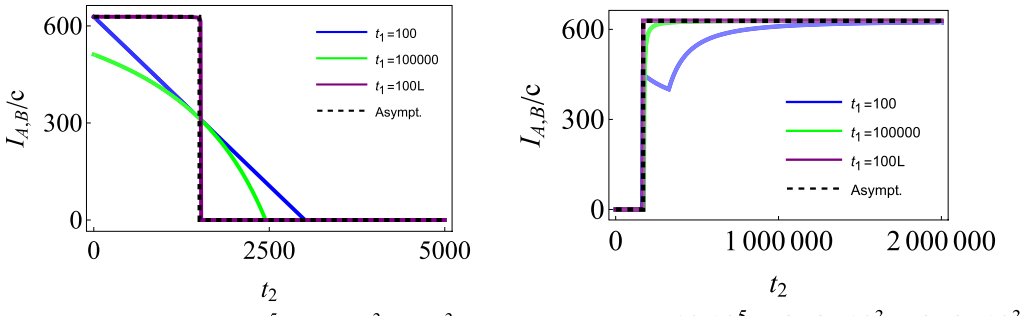

(a) t_2-dependence of $I_{A,B}$ in (A). (b) t_2-dependence of $I_{A,B}$ in (C).

FIG. 19. BMI, $I_{A,B}$, of (8) for various t_1 as the function of t_2. For simplicity, $l_A = l_B$. In (a), the solid lines illustrate the t_2 dependence of $I_{A,B}$ with $t_1 = 10, 1000, 10^6$ for (A). In (b), the solid lines illustrate the t_2 dependence of $I_{A,B}$ with $t_1 = 10, 1000, 10^6$ for (C). The dashed line illustrates the asymptotic behavior in (C2).

where $\frac{L}{2} > L - Y_1 > Y_2 > 0$. We can see from the t_2 dependence of S_B that except for the vacuum entropy, it may be described by the propagation of quasiparticles at the velocities, $v_{L,R}(x) = \pm 2\cos^2(\frac{\pi x}{L})$. Here $v_{L,R}(x)$ denote the speeds of left- and right-moving quasiparticles, respectively.

2. The t_2 dependence of BMI

Now, we report the t_2 dependence of BMI for the subsystems discussed in Sec. V B.

a. The single interval

For the single intervals considered in Sec. V B 1, we depict the $I_{A,B}$ for various t_1 as a function of t_2 in Fig. 19. For (C), $I_{A,B}$ is approximately zero. In the large-t_1 limit, the asymptotic behavior of $I_{A,B}$ for the single interval is given by

$$\text{If } x = X_f^1 \in B, \quad I_{A,B} \underset{t_1 \gg 1}{\approx} \begin{cases} \frac{c\pi l_A}{3\epsilon} & \frac{L}{2\pi}\left|\tan\left(\frac{\pi Y_2}{L}\right)\right| > t_2 > 0 \\ 0 & t_2 > \frac{L}{2\pi}\left|\tan\left(\frac{\pi Y_2}{L}\right)\right| \end{cases},$$

$$\text{If } x = X_f^2 \in B, \quad I_{A,B} \underset{t_1 \gg 1}{\approx} \begin{cases} 0 & \frac{L}{2\pi}\left|\tan\left(\frac{\pi Y_1}{L}\right)\right| > t_2 > 0 \\ \frac{c\pi l_A}{3\epsilon} & t_2 > \frac{L}{2\pi}\left|\tan\left(\frac{\pi Y_1}{L}\right)\right| \end{cases}, \tag{C2}$$

where $L - Y_1 > Y_2 > 0$. For (A) and (C), there are t_2 regimes where both B.H.-like excitations introduced in Sec. V B 1 are in B, while for (B), there are none.

b. The double intervals

Let us now turn to the t_2 dependence of $I_{A,B_1\cup B_2}$ for the subsystems in (32). In Fig. 20, we depict $I_{A,B_1\cup B_2}$ for large t_1 as a function of t_2. The asymptotic behavior of $I_{A,B=B_1\cup B_2}$ for the t_1 regime is given by

$$I_{A,B=B_1\cup B_2} \approx \begin{cases} 0 & \frac{L}{2\pi}\left|\tan\left(\frac{\pi Y_2}{L}\right)\right| > t_2 > 0 \\ \frac{c\pi l_A}{3\epsilon} & \frac{L}{2\pi}\left|\tan\left(\frac{\pi Y_1}{L}\right)\right| \geqslant t_2 \geqslant \frac{L}{2\pi}\left|\tan\left(\frac{\pi Y_2}{L}\right)\right| \\ 0 & t_2 > \frac{L}{2\pi}\left|\tan\left(\frac{\pi Y_1}{L}\right)\right| \end{cases}, \tag{C3}$$

where $\frac{L}{2} > Y_1 > Y_2 > 0$. In this case, there is a time regime where both of the black-hole-like excitations can be in $B = B_1 \cup B_2$. However, there is no time regime where both of the black-hole-like excitations are in only B_1 or B_2.

3. The t_2 dependence of TMI

We present the asymptotic behavior of TMI in the large-t_1 limit. The TMI, which we consider are $I_{A,B,\overline{B}}$ and I_{A,B_1,B_2}. They are defined by (34) and (35), respectively. The value of the global TMI for the large t_1 is zero. In the early t_2 regime, $\frac{L}{2\pi}|\tan(\frac{\pi Y_2}{L})| > t_2 > 0$, the local MI is zero, in the intermediate t_2 interval, $\frac{L}{2\pi}|\tan(\frac{\pi Y_1}{L})| > t_2 > \frac{L}{2\pi}|\tan(\frac{\pi Y_2}{L})|$, it is approximated by $-2S_A^{\text{Reg.}}$, and then, in the late t_2 regime, $t_2 > \frac{L}{2\pi}|\tan(\frac{\pi Y_1}{L})|$, it is zero. We can see from the t_2 dependence of the global TMI that as in the case of (6), there is no nonlocally hidden correlation between A, B, and $\overline{B}$. Furthermore, we can see the time t_2 dependence of the local TMI that there may exist the nonlocally hidden correlation shared by A, B_1, and B_2.

By contrast, both the local and global TMI for the setup in Fig. 20 vanishes for both physical spin structures $\nu = 3, 4$ in the free fermion CFT as expected. This is because the entanglement is carried by bell pairs in the free theory and hence there is no tripartite entanglement.

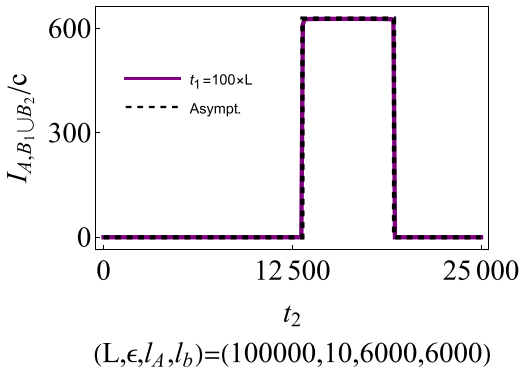

FIG. 20. The BMI, $I_{A,B_1\cup B_2}$, in the large-t_1 regime as the function of t_2. The solid line illustrates the t_2 dependence of $I_{A,B_1\cup B_2}$ for $t_1 = 10^7$. In this figure, $l_{B_1} = l_{B_2} = l_b$, $P_{C,B_1} = \frac{3L}{4}$ and $P_{C,B_2} = \frac{L}{4}$, and $P_{C,A} = X_f^1$. The dashed line illustrates the t_2 dependence of $I_{A,B_1\cup B_2}$ in (C3).

4. Growth of wormhole for (8)

Let us present the t_2 dependence of $F(X_1, Y_1)$ for the various t_1 for (8). In Fig. 21, we depict $F(X_1, Y_1)$ for the various t_1 as a function of t_2. For the large-t_1 regime, the t_2 dependence of $F(X_1, Y_1)$ is given by

$$F(X_1,Y_1)\approx 4h_{\mathcal{O}}\log\left(\frac{2\epsilon}{\pi}\right)+h_{\mathcal{O}}\log\left(\frac{16\pi^4t_1^4\left(L^2\sin^2\left(\frac{\pi Y_1}{L}\right)-4\pi^2t_2^2\cos^2\left(\frac{\pi Y_1}{L}\right)\right)^2}{L^8}\right)+\begin{cases}\frac{h_{\mathcal{O}}L\pi}{\epsilon} & \text{for } \frac{L}{2\pi}\tan\left(\frac{\pi Y_1}{L}\right)>t_2>0\\ \frac{2\pi h_{\mathcal{O}}L}{\epsilon} & \text{for } t_2>\frac{L}{2\pi}\tan\left(\frac{\pi Y_1}{L}\right)\end{cases}. \tag{C4}$$

APPENDIX D: NONCHAOTIC THEORIES

Let us present the details of the calculations and results in 2d free fermion CFT.

1. The entanglement entropy in 2d free fermion CFT

In this section, we outline the technique for calculating entanglement entropy for free Dirac fermions using bosonization as explained in [109]. There are two possible boundary conditions one can impose on the fermions along each cycle of the torus, namely, the periodic (R) or anti-periodic (NS) boundary conditions,

$$\psi\left(\frac{w}{2\epsilon}+1\right)=e^{2i\pi\nu_1}\psi\left(\frac{w}{2\epsilon}\right),$$
$$\psi\left(\frac{w}{2\epsilon}+\tau\right)=e^{2i\pi\nu_2}\psi\left(\frac{w}{2\epsilon}\right). \tag{D1}$$

The four possibilities are summarized in Table II. In this coordinate system, the cycle along $\tau = iL/2\epsilon$ corresponds to the spatial direction.

Let A and B denote the subsystems of $\mathcal{H}_2$ and $\mathcal{H}_1$, respectively. The edges of A are denoted by X_1 and X_2. while those of B are denoted by Y_1 and Y_2. Here, we assume that $X_1 > X_2 > 0$ and $Y_1 > Y_2 > 0$. The Rényi entanglement entropy is given by a two-point function of the twist operators on the 2-torus. This is equivalent to the partition function on the orbifolded theory with a branch cut running along the entanglement cut. Such a partition function can be computed using bosonization [109]. The resulting operator entanglement entropy can be divided into one piece that depends on the spin structure and another that does not. For a subsystem $\mathcal{V}$, the former shall be referred to as the nonuniversal piece $S^{(n)}_{\mathcal{V},\nu,\text{non-univ.}}$ while the latter will be referred to as the universal piece $S^{(n)}_{\mathcal{V},\text{univ.}}$ so that $S^{(n)}_{V,\nu}=S^{(n)}_{\mathcal{V},\text{univ.}}+S^{(n)}_{\mathcal{V},\nu,\text{non-univ.}}$. For an interval B in the first Hilbert space and A in the second Hilbert space as well as their union, the universal and nonuniversal pieces are given by

$$S^{(n)}_{A,\text{univ.}}=\frac{n+1}{12n}\log\left|\frac{2\epsilon\theta_1\left(\frac{w_{X_1}-w_{X_2}}{2\epsilon}|\tau\right)}{\partial_z\theta_1(0|\tau)}\right|^2,$$

$$S^{(n)}_{A,\nu,\text{non-univ.}}=\frac{1}{1-n}\sum_{k=-\frac{n-1}{2}}^{\frac{n-1}{2}}\log\left|\frac{\theta_\nu\left(\frac{k}{N}\frac{w_{X_1}-w_{X_2}}{2\epsilon}|\tau\right)}{\theta_\nu(0|\tau)}\right|^2,$$

$$S^{(n)}_{B,\text{univ.}}=-\frac{c(n+1)}{24n}\log\left[\prod_{i=1,2}\left|\frac{dw^{\text{New},\alpha}_{Y_i}}{dw_{Y_i}}\frac{d\bar{w}^{\text{New},\alpha}_{Y_i}}{d\bar{w}_{Y_i}}\right|\right]$$
$$+\frac{n+1}{12n}\log\left|\frac{2\epsilon\theta_1\left(\frac{w^{\text{New},\alpha}_{Y_1}-w^{\text{New},\alpha}_{Y_2}}{2\epsilon}|\tau\right)}{\partial_z\theta_1(0|\tau)}\right|^2,$$

$$S^{(n)}_{B,\nu,\text{non-univ.}}=\frac{1}{1-n}\sum_{k=-\frac{n-1}{2}}^{\frac{n-1}{2}}\log\left|\frac{\theta_\nu\left(\frac{k}{N}\frac{w^{\text{New},\alpha}_{Y_1}-w^{\text{New},\alpha}_{Y_2}}{2\epsilon}|\tau\right)}{\theta_\nu(0|\tau)}\right|^2, \tag{D2}$$

$$S^{(n)}_{A\cup B,\text{univ.}}=S^{(n)}_{A,\text{univ.}}+S^{(n)}_{B,\text{univ.}}+\frac{n+1}{12n}$$
$$\times\log\left|\frac{\theta_1\left(\frac{w_{X_2}-w^{\text{New},\alpha}_{Y_2}}{2\epsilon}|\tau\right)\theta_1\left(\frac{w^{\text{New},\alpha}_{Y_1}-w_{X_1}}{2\epsilon}|\tau\right)}{\theta_1\left(\frac{w_{X_1}-w^{\text{New},\alpha}_{Y_2}}{2\epsilon}|\tau\right)\theta_1\left(\frac{w_{X_2}-w^{\text{New},\alpha}_{Y_1}}{2\epsilon}|\tau\right)}\right|^2,$$

$$S^{(n)}_{A\cup B,\nu,\text{non-univ.}}=\frac{1}{1-n}\sum_{k=-\frac{n-1}{2}}^{\frac{n-1}{2}}$$
$$\times\log\left|\frac{\theta_\nu\left(\frac{k}{n}\frac{w_{X_2}-w_{X_1}+w^{\text{New},\alpha}_{Y_1}-w^{\text{New},\alpha}_{Y_2}}{2\epsilon}|\tau\right)}{\theta_\nu(0|\tau)}\right|^2, \tag{D3}$$

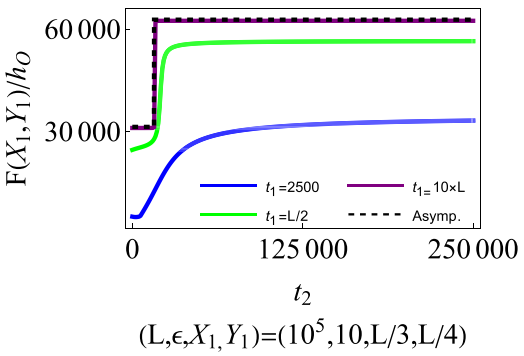

FIG. 21. The t_2 dependence of $F(X_1, Y_1)$ for various t_1 for (8). The dashed line illustrates the t_2 dependence of $F(X_1, Y_1)/h_{\mathcal{O}}$ in (8).

TABLE II. Spin structures of the fermion on a torus.

ν	Sector	(ν_1, ν_2)
1	(R,R)	(0,0)
2	(R,NS)	$(0,\frac{1}{2})$
3	(NS,NS)	$(\frac{1}{2},\frac{1}{2})$
4	(NS,R)	$(\frac{1}{2},0)$

where the $\log 2\epsilon$ terms come from rescaling the torus coordinates to have periodicities 1 and τ. Note also that when applying the bosonization formulas in [109], the coordinates of the twist operators in the different Hilbert spaces are swapped relative to one another as explained in [54].

2. Quasiparticle picture

Suppose that we prepare the systems considered in the thermofield double state, and then evolve them with the Hamiltonians acting on only $\mathcal{H}_1$. In the infinite-temperature limit, the thermofield double state can be written as a product of Bell pairs of quasiparticles as in (30). The quasiparticles that live on the Hilbert space that is being acted upon by the Hamiltonians move according to inhomogeneous velocity fields $f(x)$ and $-f(x)$ for the right-moving and left-moving quasiparticles, respectively. These quasiparticles describe the dynamics of entanglement in nonchaotic theories. When the Hamiltonian changes as in the case where different unitary operators are composed, the velocity field simply gets replaced by the envelope of the new Hamiltonian that governs the time evolution.

In the uniform case where $f(x) = 1$, the quasiparticles simply propagate with unit speed as explained in [54]. In the SSD limit, the speed vanishes at the fixed point X_f^1. Therefore, the quasiparticles tend to cluster around the fixed point X_f^1 as shown in [31], giving rise to black hole-like excitations.

a. System 1

Let us begin by looking at the case where a single inhomogeneous Hamiltonian acts on the first Hilbert space. Denote the density of the right- and left-moving quasiparticles at position x at time t by $\rho_R^{(n)}(x,t)$ and $\rho_L^{(n)}(x,t)$. The superscript n denotes the Rényi index, which determines the density of quasiparticles. Assuming that the quasiparticles are conserved, the corresponding densities have to obey the continuity equation

$$\frac{\partial \rho_i^{(n)}(x,t)}{\partial t} = \pm\left(f(x)\frac{\partial \rho_i^{(n)}(x,t)}{\partial x} + \rho_i^{(n)}(x,t)\frac{df(x)}{dx}\right) \quad \text{(D4)}$$

where the $+(-)$ sign is for the $i = L(R)$ chiralities. Since the quasiparticles are moving with a speed $f(x)$, a quasiparticle initially located at x_0 at time t_0 will be located at position x at a later time t as determined by

$$dt = \pm\frac{dx}{f(x)} \Rightarrow t - t_0 = \pm\int_{x_0}^{x}\frac{dx'}{1-\tanh 2\theta\cos\frac{2\pi x'}{L}} \quad \text{(D5)}$$

where "+" refers to right-moving quasiparticles while "−" refers to the left-moving quasiparticles. The integral is straightforward to perform and yields the trajectories $x_i(t)$ for $i = L, R$. This trajectory can also be inverted to give the initial position of $x_{i,0}(x,t)$ of a quasiparticle that is at position x at time t. Since the number of quasiparticles is conserved, the number of particles initially located in the interval $dx_{i,0}$, $\rho^{(n)}(x_{i,0}(x,t),0)dx_{i,0}$, is the same as the number of quasiparticles in dx at time t, $\rho^{(n)}(x,t)dx$. Hence, the solution to the continuity equation (D4) for a constant velocities $\pm f(x)$ is [110]

$$\rho_i^{(n)}(x,t) = \rho_i^{(n)}(x_{i,0}(x,t),0)\frac{\partial x_{i,0}(x,t)}{\partial x} \quad \text{(D6)}$$

for $i = L, R$. Since the trajectory, $x_{i,0}(x,t)$, is a periodic function with period $L\cosh 2\theta$, the corresponding quasiparticle densities also possess the same periodicity.

Now, we turn to the computation of entanglement entropy and mutual information using the quasiparticle picture. In this paper, the unitaries only act on one Hilbert space, so only the quasiparticles in that Hilbert space move while their immobile partners remain fixed at position x_0. Each such Bell pair contributes to the correlation between the point x in $\mathcal{H}_1$ and the point x_0 in $\mathcal{H}_2$. The methods for computing the mutual information and entanglement entropy in the quasiparticle picture are very similar but not identical so we explain the technique for computing each quantity separately.

Entanglement entropy. The entanglement entropy of a pure state measures the amount of correlation between the subsystem and its complement. Therefore, the entanglement entropy for a subsystem B is proportional to the number of bell pairs shared by subsystem B and its complement. Since the Bell pair partner of any quasiparticle in B lives in the other Hilbert space, any Bell pair with a quasiparticle that winds up in B at a certain time t contributes to the entanglement entropy $S_B(t)$. Therefore, the initial quasiparticle density in (D6) is a simple constant that can be fixed by equating the quasiparticle prediction for the entanglement entropy to the entanglement entropy in 2d free fermion CFT. This constant turns out to be $\rho_0 = \frac{n+1}{24n}\frac{\pi}{\epsilon}$. For a single interval $B = [Y_2, Y_1]$, the entanglement entropy according to the quasiparticle picture is

$$\begin{aligned} S_B(t) &= \int_{x\in B}\rho_L(x,t) + \int_{x\in B}\rho_R(x,t) \\ &= \sum_{i=L,R}\mathrm{mod}[x_{0,i}(Y_1,t) - x_{0,i}(Y_2,t), L] \end{aligned} \quad \text{(D7)}$$

where the integral was carried out by a simple change of variables from x to the initial position $x_{0,i}(x,t)$ and the modulo operation takes the periodicity of the system into account. This result simply states that the quasiparticles in the interval $[x_{0,i}(X_2,t), x_{0,i}(X_1,t)]$ flow to $[X_2, X_1]$ at time t.

Mutual Information. The MI is obtained by the same integral. The only difference comes from the initial quasiparticle density in (D6). This is because the MI between subsystems B and A of $\mathcal{H}_1$ and $\mathcal{H}_2$ measures the correlations between subsystems A and B and hence only receives contributions from Bell pairs one quasiparticle in subsystem A and the other in subsystem B. Since the quasiparticles in the second Hilbert space are immobile, only the quasiparticles that are initially in subsystem A can potentially contribute to the MI. Therefore, for the computation of mutual information, the initial quasiparticle density is

$$\rho_i(x,0) = \rho_0\theta(x \in A) \quad \text{(D8)}$$

where $\rho_0 = \frac{N+1}{12N}\frac{\pi}{\epsilon}$ is a constant that is fixed by equating the initial MI for two symmetric intervals $A = B$ with that of the 2d free fermion CFT. If B is the union of m disjoint $[Y_{2j}, Y_{2j-1}]$ for $j = 1, \ldots, m$, the MI between two subsystems A and B at

a fixed time t is given by

$$I_{AB}^{(n)}(t) = \sum_{j=1}^{m} \sum_{i=L,R} \int_{Y_{2j}}^{Y_{2j-1}} dx \rho_i(x_{0,i}(x,t),0) \frac{\partial x_{0,i}(x,t)}{\partial x}$$
$$= \rho_0 \sum_{j=1}^{m} \sum_{i=L,R} \text{length of } [x_{0,i}(Y_{2j},t), x_{0,i}(Y_{2j-1},t)] \cap A. \tag{D9}$$

The second equality comes from the usual change of variables from x to $x_{0,i}$ where t is held fixed so that $x_{0,i}$ is viewed as a function of a single variable x. The final expression has a simple interpretation; the quasiparticles located in $[x_{0,i}(Y_2,t), x_{0,i}(Y_1,t)]$ are the only ones that can be in subsystem B at time t. Out of these quasiparticles, only the ones that were also simultaneously in A can contribute to the mutual information between A and B.

b. System 2 and 3

System 2 and 3 correspond to time evolutions where two different unitaries are applied one after the other. The overall time evolution corresponds to a product of two unitary evolutions for durations t and T that sends a quasiparticle with an initial spacetime position

$$(0, x_0) \to (t, x) \to (t+T, y). \tag{D10}$$

Under each unitary, the quasiparticle density evolves according to (D6), so the final quasiparticle density can be related to the initial density by the chain rule

$$\rho_i(y, T+t) = \rho_i(x_0(x(y,T),t),0) \frac{\partial x_0}{\partial y}. \tag{D11}$$

The entanglement entropy is given by

$$S_B = \sum_{i=L,R} \int_{Y_2}^{Y_1} dy \frac{n+1}{24n} \frac{\pi}{\epsilon} \frac{\partial x_0}{\partial y}$$
$$= \frac{n+1}{24n} \frac{\pi}{\epsilon} \sum_{i=L,R} \text{mod}[x_0(x(Y_1,T),t) - x_0(x(Y_2,T),t), L] \tag{D12}$$

where the final equality comes from the exact same reasoning as in the Möbius/SSD case. Just as in System 1, this result simply says that the entanglement entropy of a subsystem at a particular instant in time is given by the number of quasiparticles that end up in the subsystem at that time. The mutual information as predicted by quasiparticles is similar to the entanglement entropy except for the initial quasiparticle density. If the subsystem B is a union of m disjoint intervals $[Y_{2j}, Y_{2j-1}]$, $j = 1, \ldots, m$, the mutual information is

$$I_{AB}^{(n)}(t) = \frac{n+1}{12n} \frac{\pi}{\epsilon} \sum_{i=L,R} \sum_{j=1}^{m} \int_{Y_{2j}}^{Y_{2j-1}} dy \frac{\partial x_{i,0}}{\partial y} \theta(x_{i,0} \in A)$$
$$= \frac{n+1}{12n} \frac{\pi}{\epsilon} \sum_{i=L,R} \sum_{j=1}^{m} \text{length of } [x_0(x(Y_{2j},T),t),$$
$$x_0(x(Y_{2j-1},T),t)] \cap A \tag{D13}$$

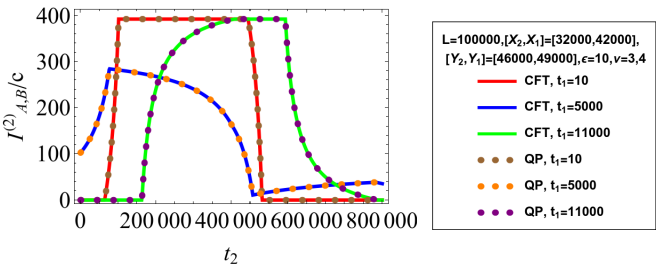

FIG. 22. Plots of the operator mutual information when the system is first acted upon by the SSD evolution for a duration of t_1 followed by a time evolution of t_2 under the CSD Hamiltonian. The solid lines are the 2d free fermion CFT results while the dots are the predictions by the quasiparticle picture.

where a change of variables from the final spatial coordinate y to the initial position $x_{i,0}$ was made to carry out the integral. The physical meaning of this result is identical to that in the Möbius/SSD case.

3. Summary of results for nonchaotic systems

Using the formulas outlined in the previous subsections, the entanglement entropy and MI can be computed in 2d free fermion CFTs and quasiparticle pictures. For the various subsystems and unitary time evolutions, the entanglement for the two physical spin structures $\nu = 3$ and $\nu = 4$ are found to be identical. Furthermore, the global TMI for 2d free fermion CFT vanishes in all the cases considered. This is because the entanglement entropy and MI for the 2d free fermion CFT agree with the quasiparticle picture to leading order in $1/\epsilon$ [111]. The agreement with the quasiparticle picture describes the key differences between 2d free fermion and holographic CFTs. Firstly, for finite values of θ, the quasiparticle distributions are periodic with a period of $L\cosh 2\theta$, so that the MI will possess the same periodicity. Secondly, the MI is separately carried by the right-moving and left-moving quasiparticles, which travel independently of one another, as opposed to the holographic theory where the MI is nonzero only when the subsystem contains both the left and the right-moving B.H.-like excitations. Lastly, the TMI is observed to vanish for the 2d free fermion CFTs but that is not always the case for the holographic theories.

In Fig. 22, we show a representative plot comparing the 2d free fermion CFT MI with the quasiparticle prediction. In this setup, we first evolve the system with the SSD Hamiltonian before evolving it with the CSD Hamiltonian, which is essentially the SSD Hamiltonian but with the envelope function vanishing at X_f^2 instead. The holographic results for this kind of evolution are discussed in Appendix C. The subsystems in Fig. 22 are placed away from both fixed points X_f^1 and X_f^2. The quasiparticles will pass through B, giving rise to a nonzero BMI. However, since the subsystem does not contain the CSD fixed point, these quasiparticles will eventually leave B although they take a long time to do so for the subsystem in Fig. 22 because B is located close to the CSD fixed point X_f^2 where the quasiparticle speed is small. This figure also highlights the key difference between the dynamics of BMI

in the free fermion CFT as well as the holographic CFTs. The BMI vanishes for this choice of subsystems in the latter but not the former for large values of t_1. This is because BMI is nonzero in the holographic theory when both chiral and antichiral B.H.-like excitations are simultaneously present in B, which does not occur when B does not contain any of the fixed points and when the SSD evolution time t_1 is large, which causes the B.H.-like excitation to be sharply peaked. By contrast, BMI is separately carried by the left- and right-moving quasiparticles so as long as either one of them is present in B, BMI is nonzero. For this choice of subsystems, the left-moving quasiparticles travel leftwards around the spatial circle and approach the CSD fixed point X_f^2 from the side opposite to subsystem B and hence do not contribute to the BMI. When the SSD quench time is $t_1 = 5000$, there are already right-moving quasiparticles in the output subsystem, so the initial value of BMI is nonzero. Some right-moving quasiparticles start off at $t_2 = 0$ at positions infinitesimally close to the CSD fixed point X_f^2 and take a long time to go around the spatial circle leading to a long tail in the BMI. When $t_1 = 11000$, the right-moving quasiparticles start off at $t_2 = 0$ to the right of the CSD fixed point at X_f^2 and eventually circle around back to subsystem A giving rise to a bump in the BMI.

APPENDIX E: THE GRAVITY DUAL OF THE SYSTEMS

Here, we report the gravity dual of the systems considered in this paper.

1. The dual geometries

The dual geometries of $\rho_{\mathcal{H}_1}$ considered in this paper are given by

$$
\begin{aligned}
ds^2_{\alpha=1,2} = R^2\Bigg[\frac{dr^2}{r^2-r_0^2} + \left(\frac{L}{\pi}\right)^4\Bigg\{&\left(r^2 f^1_{\alpha=1,2;XX} + r_0^2 f^2_{XX}\right)dX^2 + \sum_{j=0,1}\left(r^2 f^1_{\alpha=1,2;t_jt_j} + r_0^2 f^2_{\alpha=1,2;t_jt_j}\right)dt_j dt_j \\
&+ 2\left(r^2 f^1_{t_0t_1} + r_0^2 f^2_{t_0t_1}\right)dt_0 dt_1 + 2\sum_{j=0,1}\left(r^2 f^1_{\alpha=1,2;Xt_j} + r_0^2 f^2_{\alpha=1,2;Xt_j}\right)dX dt_j\Bigg\}\Bigg], \\
ds^2_{\alpha=3} = R^2\Bigg[\frac{dr^2}{r^2-r_0^2} + \left(\frac{L}{\pi}\right)^4\Bigg\{&\left(r^2 f^1_{\alpha=3;XX} + r_0^2 f^2_{\alpha=3;XX}\right)dX^2 + \sum_{j=1,2}\left(r^2 f^1_{\alpha=3;t_jt_j} + r_0^2 f^2_{\alpha=3;t_jt_j}\right)dt_j dt_j \\
&+ 2\left(r^2 f^1_{\alpha=3;t_1t_2} + r_0^2 f^2_{\alpha=3;t_1t_2}\right)dt_1 dt_2 + 2\sum_{j=1,2}\left(r^2 f^1_{\alpha=3;Xt_j} + r_0^2 f^2_{\alpha=3;Xt_j}\right)dX dt_j\Bigg\}\Bigg],
\end{aligned}
\tag{E1}
$$

where R is the AdS radius and the details of metric are summarized in Appendix E 3.

In the expression in (E1), the components such as $dt_j dt_{i\neq j}$ exist. However, in the time evolution considered, one of them should be constant. In the case of the system 1, this system is evolved with H^1 from $t_0 = 0$ to $t_0 = t_{0,\text{const.}}$, and then it is evolved with H^1_{SSD} from $t_1 = 0$. Therefore, we should take t_0 to be constant and consider the t_1 dependence of the geometry. In this procedure, let us rewrite the radial direction as $r' = (\frac{L^2}{\pi^2})\sqrt{f^1_{\alpha=1;XX}}r$ that guarantees that the asymptotic geometry near the boundary, $r' \to \infty$, is given by the SSD AdS_3 geometry,

$$
ds^2_{\alpha=1} \approx R^2\left[\frac{dr'^2}{r'^2} + r'^2 dX^2 + r'^2\frac{f^1_{\alpha=1;t_1t_1}}{f^1_{\alpha=1;XX}}dt_1 dt_1\right] = R^2\left[\frac{dr'^2}{r'^2} + r'^2 dX^2 - 4\sin^4\left(\frac{\pi X}{L}\right)r'^2 dt_1 dt_1\right],
\tag{E2}
$$

where the time-component of the metric depends on X.

In the case of the systems 2 and 3, the system is evolved with H^1_{SSD} from $t_1 = 0$ to $t_1 = t_{1,\text{const.}}$, and then it is evolved with H^1 from $t_0 = 0$ or H^1_{CSD} from $t_2 = 0$. Therefore, we should take t_1 to be constant and consider the geometries. Rewrite the radial coordinate as $r'_{\alpha=2,3} = (\frac{L^2}{\pi^2})\sqrt{f^1_{\alpha=2,3;XX}}r$, and then the metric near the boundary, $r'_{i=2,3} \to \infty$, is given by the global AdS_3 for $\alpha = 2$ and the CSD AdS_3 for $\alpha = 3$,

$$
ds^2_{\alpha=3} \approx R^2\left[\frac{dr'_{\alpha=3}}{r'^2_{\alpha=3}} + r'^2_{\alpha=3}dX^2 - 4\cos^4\left(\frac{\pi X}{L}\right)r'^2_{\alpha=3}dt_2 dt_2\right].
\tag{E3}
$$

As a consequence, the location of the black hole horizon in $r'_{\alpha=2,3}$ coordinate is given by

$$
r'_{\alpha=2,3:\text{Horizon}} = r_0\left(\frac{L^2}{\pi^2}\right)\sqrt{f^1_{\alpha=2,3:XX}}.
\tag{E4}
$$

Thus, $r'_{\alpha=2:\text{Horizon}}$ depends on X, t_0 and t_1, while $r'_{\alpha=3:\text{Horizon}}$ depends on X, t_1, and t_2.

a. The temporal and spatial dependence of the inhomogeneous horizon

Let us focus on the temporal and spatial dependence of the black hole horizon of the black hole geometries dual to the system 2 and 3.

Asymptotic behavior of horizon with small t_1. Let us begin by looking closely at the temporal and spatial dependence of inhomogeneous black hole horizon in the small t_1 region. At the second order of the small t_1 expansion, the t_0 dependence of $r'_{\alpha=2;\mathrm{Horizon}}$ and the t_2 dependence of $r'_{\alpha=3;\mathrm{Horizon}}$ are given by

$$\begin{aligned} r'_{\alpha=2:\mathrm{Horizon}} &\approx r_0\left(\frac{\pi^2}{L^2}+2\frac{\pi^3 t_1}{L^3}\sin\left[\frac{2\pi t_0}{L}\right]\cos\left[\frac{2\pi X}{L}\right]\right), \\ r'_{\alpha=3:\mathrm{Horizon}} &\approx r_0\Bigg[\frac{\pi^2}{\sqrt{L^4+2\pi^2t_2^2\left(2\left(L^2+2\pi^2t_2^2\right)\cos\left(\frac{2\pi X}{L}\right)+\left(L^2+\pi^2t_2^2\right)\cos\left(\frac{4\pi X}{L}\right)\right)+2\pi^2L^2t_2^2+6\pi^4t_2^4}} \\ &\quad+\frac{8\pi^4t_1t_2\cos^2\left(\frac{\pi X}{L}\right)\left(\left(L^2+2\pi^2t_2^2\right)\cos\left(\frac{2\pi X}{L}\right)+2\pi^2t_2^2\right)}{\left(L^4+2\pi^2t_2^2\left(2\left(L^2+2\pi^2t_2^2\right)\cos\left(\frac{2\pi X}{L}\right)+\left(L^2+\pi^2t_2^2\right)\cos\left(\frac{4\pi X}{L}\right)\right)+2\pi^2L^2t_2^2+6\pi^4t_2^4\right)^{3/2}}\Bigg] \end{aligned} \tag{E5}$$

where $r'_{\alpha=2:\mathrm{Horizon}}$ at $X=0,\frac{L}{2}$ is independent of t_0, and $r'_{\alpha=3:\mathrm{Horizon}}$ at $X=\frac{L}{2}$ is independent of t_1.

Asymptotic behavior of horizon in $t_1\to\infty$. Now, turn to the temporal and spatial dependence of inhomogeneous black hole horizon in the large-t_1 regime. In the large-t_1 regime excluding $t_0\approx X+nL$ and $t_0\approx -X+nL$, the asymptotic time dependence of $r'_{i=2,\mathrm{Horizon}}$ is approximated by

$$r'_{\alpha=2,\mathrm{Horizon}}\approx\frac{r_0}{4t_1^2\left|\sin\left(\frac{\pi(t_0-X)}{L}\right)\sin\left(\frac{\pi(t_0+X)}{L}\right)\right|}, \tag{E6}$$

where n is and integer number, and $t_0=\pm X+nL$ are the trajectories of the right- and left-moving B.H.-like excitations. This suggests the black hole horizon far from the B.H.-like excitations is proportional to t_1^{-2}.

Extremes of $r'_{\alpha=2,Horizon}$. Let us analyze the spatial extremes of $r'_{\alpha=2,\mathrm{Horizon}}$. These spatial extremes are determined by $\partial_X r'_{\alpha=2,\mathrm{Horizon}}=0$, and these solutions are given by

$$X=0,\frac{L}{2},\cos\left(\frac{2\pi X_{j=L,R}}{L}\right)=\frac{L^2+2\pi^2t_1^2}{2\pi t_1\left(L^2+\pi^2t_1^2\right)}\left(L\sin\left(\frac{2\pi t_0}{L}\right)+\pi t_1\cos\left(\frac{2\pi t_0}{L}\right)\right). \tag{E7}$$

For $X_{j=L,R}$, $r'_{\alpha=2,\mathrm{Horizon}}$ is given by

$$r'_{\alpha=2,\mathrm{Horizon}}=\frac{r_0\sqrt{L^2+\pi^2t_1^2}}{\left|L\cos\left(\frac{2\pi t_0}{L}\right)-\pi t_1\sin\left(\frac{2\pi t_0}{L}\right)\right|} \tag{E8}$$

In the large-t_1 limit, $X_{i=L,R}$ are approximated by

$$X_{j=L,R}+mL=\pm t_0, \tag{E9}$$

where m is an integer number. By using the physical interpretation discussed in Sec. V B 1, $X+mL=\pm t_0$ are interpreted as the trajectories at t_0 of the right- and left-moving B.H.-like excitations, respectively. In other words, the spatial extremes for the large t_1 are determined by the trajectories at t_0 of the right- and left-moving B.H.-like excitations. As a consequence, the asymptotic behavior of $r'_{\alpha=2,\mathrm{Horizon}}$ for the large t_1 is given by

$$r'_{\alpha=2,\mathrm{Horizon}}\approx\begin{cases}\frac{r_0}{\left|\sin\left(\frac{2\pi t_0}{L}\right)\right|} & \text{for } t_0\neq\frac{nL}{2}\\ \frac{\pi r_0 t_1}{L} & \text{for } t_0=\frac{nL}{2}\end{cases}, \tag{E10}$$

where n is an integer number. Thus, if the B.H.-like excitations are at $X\neq X^f_{i=1,2}$, then $r'_{\alpha=2,\mathrm{Horizon}}$ depends on only t_0, while if these excitations are at $X=X^f_{i=1,2}$, then $r'_{\alpha=2,\mathrm{Horizon}}$ depends on only t_1, and it linearly increases with t_1. Note that the asymptotic form of the black hole horizon for $t_0\neq\frac{nL}{2}$ is invalid in the t_0 regimes where $t_0\approx\frac{nL}{2}$. In these t_0 regimes, we need more detailed calculations.

Extremes of $r'_{\alpha=3,Horizon}$. Now, let us turn to the analysis of the spatial extremes of $r'_{\alpha=3,\mathrm{Horizon}}$. The spatial extremes are determined by $\partial_X r'_{\alpha=3,\mathrm{Horizon}}=0$, and the solutions of this equation are given by

$$X=0,\frac{L}{2},\cos\left(\frac{2\pi X_{j=L,R}}{L}\right)=-\frac{\left(L^4+2\pi^2L^2(t_1-t_2)^2+8\pi^4t_1^2t_2^2\right)\left(4\pi^2t_1^2t_2^2-L^2(t_1-t_2)^2\right)}{2\left(L^4+\pi^2L^2(t_1-t_2)^2+4\pi^4t_1^2t_2^2\right)\left(4\pi^2t_1^2t_2^2+L^2(t_1-t_2)^2\right)}. \tag{E11}$$

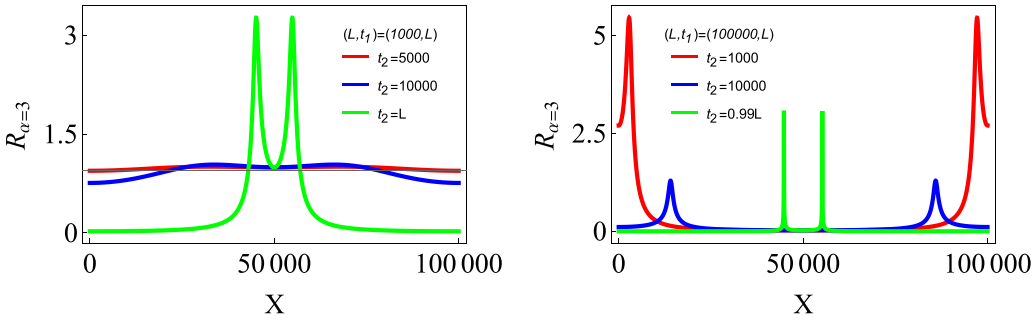

(a) Small t_1-regime. (b) Large t_1-regime.

FIG. 23. The spatial dependence of the black hole horizon for various t_1 and t_2 as a function of X. Here, $R_{\alpha=3}$ is defined by $r_{\alpha=3,\text{Horizon}}/r_0$. For the large t_1, the spatial locations where the peaks of $R_{\alpha=3}$ emerge are approximately equal to the locations of the B.H.-like excitations.

In the large-t_1 limit, $X_{j=L,R}$ are determined by

$$\cos\left(\frac{2\pi X_{j=L,R}}{L}\right) \approx -\frac{\left(4\pi^2 t_2^2 - L^2\right)}{\left(4\pi^2 t_2^2 + L^2\right)}. \tag{E12}$$

This is the same as the trajectories of the left- and right-moving B.H.-like excitations emerging at $x = X_1^f$ at time $t_2 = 0$. Under the evolution by H^1_{CSD}, these excitations moves at the velocities, $v_{j=L,R} = \pm 2\cos^2\left(\frac{\pi x}{L}\right)$, to the X_2^f. The extremes of the black hole horizon for $x = X_{j=L,R}$ are given by

$$r'_{\alpha=3,\text{Horizon}} = \frac{r_0\sqrt{\left(L^2(t_1-t_2)^2 + 4\pi^2 t_1^2 t_2^2\right)\left(L^4 + \pi^2 L^2 (t_1-t_2)^2 + 4\pi^4 t_1^2 t_2^2\right)}}{\left|L^3(t_2-t_1) + 4\pi^2 L t_1^2 t_2\right|}. \tag{E13}$$

In the large-t_1 limit for $t_2 > 0$, the extremes of $r'_{\alpha=3,\text{Horizon}}$ are given by

$$r'_{\alpha=3,\text{Horizon}} \approx \frac{r_0\left(L^2 + 4\pi^2 t_2^2\right)}{4\pi L t_2}. \tag{E14}$$

Furthermore, take the large-t_2 limit, and then these extremes are given by

$$r'_{\alpha=3,\text{Horizon}} \approx \frac{\pi r_0 t_2}{L}. \tag{E15}$$

Thus, these extremes linear grow with t_2. In Fig. 23, we depict $r'_{\alpha=3,\text{Horizon}}$ for various t_1 and t_2 as a function of X.

2. Geodesic length in the static BTZ black hole

Here, we present the nonuniversal piece of (59). It is given by

$$G(X_1, Y_1) = 2\log\left(\frac{2\epsilon}{\pi}\right) + \text{Min}[S_1, S_2, S_3], \tag{E16}$$

where $S_{i=1,2,3}$ are defined as

$$S_1 = \log\left[\left|\sin\left[\frac{\pi}{2\epsilon}\left(w^{\text{New},\alpha}_{Y_1,\epsilon} - w_{X_1}\right)\right]\right|^2\right], \quad S_2 = \log\left[\left|\sin\left[\frac{\pi}{2\epsilon}\left(iL - \left(w^{\text{New},\alpha}_{Y_1,\epsilon} - w_{X_1}\right)\right)\right]\right|^2\right],$$
$$S_3 = \log\left[\left|\sin\left[\frac{\pi}{2\epsilon}\left(-iL - \left(w^{\text{New},\alpha}_{Y_1,\epsilon} - w_{X_1}\right)\right)\right]\right|^2\right]. \tag{E17}$$

3. The metric of the inhomogeneous black holes

Here, we present the inhomogeneous black hole geometries. The dual geometries of $\rho_{\mathcal{H}_1}$ considered in this paper are given by (E1) and the components are given as follows. For $\alpha = 1$,

$$f^1_{\alpha=1;XX} = \frac{\pi^4}{D_{\alpha=1}}, \quad f^2_{\alpha=1;XX} = \frac{4\pi^6 L^2 t_1^2 \sin^2\left(\frac{2\pi X}{L}\right)}{(D_{\alpha=1})^2}, \quad f^1_{\alpha=1;t_0t_0} = -1, \quad f^2_{\alpha=1;t_0t_0} = 1,$$
$$f^1_{\alpha=1;t_1t_1} = -\frac{4\pi^4 \sin^4\left(\frac{\pi X}{L}\right)}{D_{\alpha=1}}, \quad f^2_{\alpha=1;t_1t_1} = \frac{4\pi^4 \sin^4\left(\frac{\pi X}{L}\right)\left[L^2 - 2\pi^2 t_1^2 \cos\left(\frac{2\pi X}{L}\right) + 2\pi^2 t_1^2\right]^2}{(D_{\alpha=1})^2},$$

$$
\begin{aligned}
f^1_{\alpha=1;t_0t_1} &= f^2_{\alpha=1;t_0t_1} = -\frac{2\pi^2 \sin^2\left(\frac{\pi X}{L}\right)\left[L^2 + 4\pi^2 t_1^2 \sin^2\left(\frac{\pi X}{L}\right)\right]}{D_{\alpha=1}},\\
f^1_{\alpha=1;Xt_0} &= -f^2_{\alpha=1;Xt_0} = -\frac{2\pi^3 L t_1 \sin\left(\frac{2\pi X}{L}\right)}{D_{\alpha=1}}, \quad f^1_{\alpha=1;Xt_1} = 0,\\
f^2_{\alpha=1;Xt_1} &= \frac{8\pi^5 L t_1 \sin^3\left(\frac{\pi X}{L}\right)\cos\left(\frac{\pi X}{L}\right)\left[L^2 - 2\pi^2 t_1^2 \cos\left(\frac{2\pi X}{L}\right) + 2\pi^2 t_1^2\right]}{(D_{\alpha=1})^2},\\
D_{\alpha=1} &= \left[L^2 + 4\pi^2 t_1^2 \sin^2\left(\frac{\pi X}{L}\right)\right]^2 - 4\pi^2 L^2 t_1^2 \sin^2\left(\frac{2\pi X}{L}\right).
\end{aligned} \tag{E18}
$$

For $\alpha = 2$,

$$
\begin{aligned}
f^1_{\alpha=2;XX} &= \frac{\pi^4}{D_{\alpha=2}}, \quad f^2_{\alpha=2;XX} = \frac{4\pi^6 t_1^2 \sin^2\left(\frac{2\pi X}{L}\right)\left[L\cos\left(\frac{2\pi t_0}{L}\right) - \pi t_1 \sin\left(\frac{2\pi t_0}{L}\right)\right]^2}{(D_{\alpha=2})^2}, \quad f^1_{\alpha=2;t_0t_0} = -\frac{\pi^4}{D_{\alpha=2}},\\
f^2_{\alpha=2;t_0t_0} &= \frac{\pi^4}{(D_{\alpha=2})^2}\left(L^2 - \pi t_1\left\{\pi t_1\left[\cos\left(\frac{2\pi(t_0 - X)}{L}\right) + \cos\left(\frac{2\pi(t_0 + X)}{L}\right)\right]\right.\right.\\
&\quad \left.\left. + L\left[\sin\left(\frac{2\pi(t_0 - X)}{L}\right) + \sin\left(\frac{2\pi(t_0 + X)}{L}\right)\right]\right\} + 2\pi^2 t_1^2\right)^2,\\
f^1_{\alpha=2;t_1t_1} &= -\frac{4\pi^4 \sin^2\left(\frac{\pi(t_0 - X)}{L}\right)\sin^2\left(\frac{\pi(t_0 + X)}{L}\right)}{D_{\alpha=2}},\\
f^2_{\alpha=2;t_1t_1} &= \pi^4\left[\frac{\sin^2\left(\frac{\pi(t_0 + X)}{L}\right)}{d_{\alpha=2;p}} + \frac{\sin^2\left(\frac{\pi(t_0 - X)}{L}\right)}{d_{\alpha=2;m}}\right]^2\\
&\quad + \frac{\sin^2\left(\frac{\pi(t_0 - X)}{L}\right)}{(d_{\alpha=2;m})^2}\left(\frac{2\sin^2\left(\frac{\pi(t_0 + X)}{L}\right)d_{\alpha=2;m} + \sin^2\left(\frac{\pi(t_0 - X)}{L}\right)d_{\alpha=2;p}}{d_{\alpha=2;p}}\right),\\
f^1_{\alpha=2;t_0t_1} &= -\frac{\pi^4\left[\sin^2\left(\frac{\pi(t_0 - X)}{L}\right) + \sin^2\left(\frac{\pi(t_0 + X)}{L}\right)\right]}{D_{\alpha=2}},\\
f^2_{\alpha=2;t_0t_1} &= \frac{1}{2}\pi^4\left[\frac{\sin^2\left(\frac{\pi(t_0 - X)}{L}\right)}{(d_{\alpha=2;m})^2} + \frac{\sin^2\left(\frac{\pi(t_0 - X)}{L}\right) + \sin^2\left(\frac{\pi(t_0 + X)}{L}\right)}{D_{\alpha=2}} + \frac{\sin^2\left(\frac{\pi(t_0 + X)}{L}\right)}{(d_{\alpha=2;p})^2}\right],\\
D_{\alpha=2} &= d_{\alpha=2;p} \times d_{\alpha=2;m},\\
d_{\alpha=2;m} &= \left\{L^2 - 2\pi t_1\left[\pi t_1 \cos\left(\frac{2\pi(t_0 - X)}{L}\right) + L\sin\left(\frac{2\pi(t_0 - X)}{L}\right)\right] + 2\pi^2 t_1^2\right\},\\
d_{\alpha=2;p} &= \left\{L^2 - 2\pi t_1\left[\pi t_1 \cos\left(\frac{2\pi(t_0 + X)}{L}\right) + L\sin\left(\frac{2\pi(t_0 + X)}{L}\right)\right] + 2\pi^2 t_1^2\right\},\\
f^1_{\alpha=2;Xt_0} &= 0, \quad f^2_{Xt_0} = \frac{1}{4}\pi^4\left[\frac{1}{\left(d_{\alpha=2;p}\right)^2} - \frac{1}{(d_{\alpha=2;m})^2}\right],\\
f^1_{\alpha=2;Xt_1} &= \frac{\pi^4\left[\sin^2\left(\frac{\pi(t_0 + X)}{L}\right) - \sin^2\left(\frac{\pi(t_0 - X)}{L}\right)\right]}{D_{\alpha=2}},\\
f^2_{\alpha=2;Xt_1} &= -\frac{\pi^5 t_1}{(D_{\alpha=2})^2}\left[\sin^2\left(\frac{\pi(t_0 - X)}{L}\right)d_{\alpha=2,p} + \sin^2\left(\frac{\pi(t_0 + X)}{L}\right)d_{\alpha=2,m}\right]\left\{\pi t_1\left[\cos\left(\frac{2\pi(t_0 - X)}{L}\right) - \cos\left(\frac{2\pi(t_0 + X)}{L}\right)\right]\right.\\
&\quad \left. + L\left[\sin\left(\frac{2\pi(t_0 - X)}{L}\right) - \sin\left(\frac{2\pi(t_0 + X)}{L}\right)\right]\right\}.
\end{aligned} \tag{E19}
$$

For $\alpha = 3$,

$$
\begin{aligned}
f^1_{\alpha=3;XX} &= \frac{\pi^4 L^4}{d^1_{XX}}, \quad f^2_{XX} = \frac{4\pi^6 L^6\left[L^2(t_2-t_1)+4\pi^2 t_1^2 t_2\right]^2 \sin^2\left(\frac{2\pi X}{L}\right)}{d^2_{XX}},\\
f^1_{t_1t_1} &= -\frac{\pi^4\left[-\left(L^2+4\pi^2 t_2^2\right)\cos\left(\frac{2\pi X}{L}\right)+L^2-4\pi^2 t_2^2\right]^2}{d^1_{t_1t_1}},\\
f^2_{\alpha=3;t_1t_1} &= \frac{\pi^4}{d^2_{t_1t_1}}\Bigg\{L^6+\pi^2L^4\left(3t_1^2+2t_1t_2+t_2^2\right)+4\pi^4L^2t_2^2\left(-2t_1^2-6t_1t_2+3t_2^2\right)\\
&\quad+\pi^2\left[L^4\left(t_1^2-2t_1t_2+3t_2^2\right)+4\pi^2L^2t_2^2\left(2t_1^2-2t_1t_2+t_2^2\right)+16\pi^4t_1^2t_2^4\right]\cos\left(\frac{4\pi X}{L}\right)\\
&\quad-\left[L^6+4\pi^2L^4(t_1-t_2)(t_1+t_2)+16\pi^4L^2t_2^3(2t_1-t_2)-64\pi^6t_1^2t_2^4\right]\cos\left(\frac{2\pi X}{L}\right)+48\pi^6t_1^2t_2^4\Bigg\}^2,\\
f^1_{\alpha=3;t_2t_2} &= -\frac{4\pi^4L^4\cos^4\left(\frac{\pi X}{L}\right)}{d^1_{t_2t_2}},\\
f^2_{\alpha=3;t_2t_2} &= \frac{4\pi^4L^4\cos^4\left(\frac{\pi X}{L}\right)}{d^2_{t_2t_2}}\left\{L^4+2\pi^2\left[L^2\left(-t_1^2-2t_1t_2+t_2^2\right)+4\pi^2t_1^2t_2^2\right]\cos\left(\frac{2\pi X}{L}\right)+2\pi^2L^2(t_1-t_2)^2+8\pi^4t_1^2t_2^2\right\}^2,\\
f^1_{\alpha=3;Xt_1} &= \frac{4\pi^5L^3t_2\sin\left(\frac{2\pi X}{L}\right)}{d^1_{Xt_1}},\\
f^2_{\alpha=3;Xt_1} &= -\frac{2\pi^5L^3\left[L^2(t_2-t_1)+4\pi^2t_1^2t_2\right]\sin\left(\frac{2\pi X}{L}\right)}{d^2_{Xt_1}}\Bigg\{L^6+\pi^2L^4\left(3t_1^2+2t_1t_2+t_2^2\right)\\
&\quad+4\pi^4L^2t_2^2\left(-2t_1^2-6t_1t_2+3t_2^2\right)+\pi^2\left[L^4\left(t_1^2-2t_1t_2+3t_2^2\right)+4\pi^2L^2t_2^2\right.\\
&\quad\left.\times\left(2t_1^2-2t_1t_2+t_2^2\right)+16\pi^4t_1^2t_2^4\right]\cos\left(\frac{4\pi X}{L}\right)-\left[L^6+4\pi^2L^4(t_1-t_2)(t_1+t_2)\right.\\
&\quad\left.+16\pi^4L^2t_2^3(2t_1-t_2)-64\pi^6t_1^2t_2^4\right]\cos\left(\frac{2\pi X}{L}\right)+48\pi^6t_1^2t_2^4\Bigg\},\\
f^1_{\alpha=3;Xt_2} &= 0, \quad f^2_{Xt_2} = \frac{1}{2}\pi^4L^4\cos^2\left(\frac{\pi X}{L}\right)\left(\frac{1}{d^{2,a}_{Xt_2}}-\frac{1}{d^{2,b}_{Xt_2}}\right),\\
f^1_{\alpha=3;t_1t_2} &= -\frac{2\pi^4L^2\cos^2\left(\frac{\pi X}{L}\right)\left[-\left(L^2-4\pi^2t_2^2\right)\cos\left(\frac{2\pi X}{L}\right)+L^2+4\pi^2t_2^2\right]}{d^1_{t_1t_2}},\\
f^2_{\alpha=3;t_1t_2} &= \frac{N_{t_1t_2}}{d^2_{t_1t_2}}.
\end{aligned}
\tag{E20}
$$

In the above equations, we used the following notations:

$$
\begin{aligned}
d^1_{XX} &= \left(L^4+2\pi\left\{\pi\left[L^2\left(-t_1^2-2t_1t_2+t_2^2\right)+4\pi^2t_1^2t_2^2\right]\cos\left(\frac{2\pi X}{L}\right)\right.\right.\\
&\quad\left.\left.+L\left[L^2(t_1-t_2)-4\pi^2t_1^2t_2\right]\sin\left(\frac{2\pi X}{L}\right)\right\}+2\pi^2L^2(t_1-t_2)^2+8\pi^4t_1^2t_2^2\right)\\
&\quad\times\left(L^4+2\pi\left\{\pi\left[L^2\left(-t_1^2-2t_1t_2+t_2^2\right)+4\pi^2t_1^2t_2^2\right]\cos\left(\frac{2\pi X}{L}\right)\right.\right.\\
&\quad\left.\left.+L\left[L^2(t_2-t_1)+4\pi^2t_1^2t_2\right]\sin\left(\frac{2\pi X}{L}\right)\right\}+2\pi^2L^2(t_1-t_2)^2+8\pi^4t_1^2t_2^2\right),\\
d^2_{XX} &= \left(L^4+2\pi\left\{\pi\left[L^2\left(-t_1^2-2t_1t_2+t_2^2\right)+4\pi^2t_1^2t_2^2\right]\cos\left(\frac{2\pi X}{L}\right)\right.\right.\\
&\quad\left.\left.+L\left[L^2(t_1-t_2)-4\pi^2t_1^2t_2\right]\sin\left(\frac{2\pi X}{L}\right)\right\}+2\pi^2L^2(t_1-t_2)^2+8\pi^4t_1^2t_2^2\right)^2
\end{aligned}
$$

$$
\begin{aligned}
&\times \left(L^4 + 2\pi\left\{\pi\left[L^2\left(-t_1^2 - 2t_1t_2 + t_2^2\right) + 4\pi^2 t_1^2 t_2^2\right]\cos\left(\frac{2\pi X}{L}\right)\right.\right.\\
&\left.\left. + L\left[L^2(t_2 - t_1) + 4\pi^2 t_1^2 t_2\right]\sin\left(\frac{2\pi X}{L}\right)\right\} + 2\pi^2 L^2 (t_1 - t_2)^2 + 8\pi^4 t_1^2 t_2^2\right)^2,\\
d^1_{t_1t_1} &= \left(L^4 + 2\pi\left\{\pi\left[L^2\left(-t_1^2 - 2t_1t_2 + t_2^2\right) + 4\pi^2 t_1^2 t_2^2\right]\cos\left(\frac{2\pi X}{L}\right)\right.\right.\\
&\left.\left. + L\left[L^2(t_1 - t_2) - 4\pi^2 t_1^2 t_2\right]\sin\left(\frac{2\pi X}{L}\right)\right\} + 2\pi^2 L^2 (t_1 - t_2)^2 + 8\pi^4 t_1^2 t_2^2\right)\\
&\times \left(L^4 + 2\pi\left\{\pi\left[L^2\left(-t_1^2 - 2t_1t_2 + t_2^2\right) + 4\pi^2 t_1^2 t_2^2\right]\cos\left(\frac{2\pi X}{L}\right)\right.\right.\\
&\left.\left. + L\left[L^2(t_2 - t_1) + 4\pi^2 t_1^2 t_2\right]\sin\left(\frac{2\pi X}{L}\right)\right\} + 2\pi^2 L^2 (t_1 - t_2)^2 + 8\pi^4 t_1^2 t_2^2\right),\\
d^2_{t_1t_1} &= \left(L^4 + 2\pi\left\{\pi\left[L^2\left(-t_1^2 - 2t_1t_2 + t_2^2\right) + 4\pi^2 t_1^2 t_2^2\right]\cos\left(\frac{2\pi X}{L}\right)\right.\right.\\
&\left.\left. + L\left[L^2(t_1 - t_2) - 4\pi^2 t_1^2 t_2\right]\sin\left(\frac{2\pi X}{L}\right)\right\} + 2\pi^2 L^2 (t_1 - t_2)^2 + 8\pi^4 t_1^2 t_2^2\right)^2\\
&\times \left(L^4 + 2\pi\left\{\pi\left[L^2\left(-t_1^2 - 2t_1t_2 + t_2^2\right) + 4\pi^2 t_1^2 t_2^2\right]\cos\left(\frac{2\pi X}{L}\right)\right.\right.\\
&\left.\left. + L\left[L^2(t_2 - t_1) + 4\pi^2 t_1^2 t_2\right]\sin\left(\frac{2\pi X}{L}\right)\right\} + 2\pi^2 L^2 (t_1 - t_2)^2 + 8\pi^4 t_1^2 t_2^2\right]^2, \qquad \text{(E21)}\\
d^1_{t_2t_2} &= \left(L^4 + 2\pi\left\{\pi\left[L^2\left(-t_1^2 - 2t_1t_2 + t_2^2\right) + 4\pi^2 t_1^2 t_2^2\right]\cos\left(\frac{2\pi X}{L}\right)\right.\right.\\
&\left.\left. + L\left[L^2(t_1 - t_2) - 4\pi^2 t_1^2 t_2\right]\sin\left(\frac{2\pi X}{L}\right)\right\} + 2\pi^2 L^2 (t_1 - t_2)^2 + 8\pi^4 t_1^2 t_2^2\right)\\
&\times \left\{L^4 + 2\pi\left(\pi\left[L^2\left(-t_1^2 - 2t_1t_2 + t_2^2\right) + 4\pi^2 t_1^2 t_2^2\right]\cos\left(\frac{2\pi X}{L}\right)\right.\right.\\
&\left.\left. + L\left[L^2(t_2 - t_1) + 4\pi^2 t_1^2 t_2\right]\sin\left(\frac{2\pi X}{L}\right)\right\} + 2\pi^2 L^2 (t_1 - t_2)^2 + 8\pi^4 t_1^2 t_2^2\right),\\
d^2_{t_2t_2} &= \left(L^4 + 2\pi\left\{\pi\left[L^2\left(-t_1^2 - 2t_1t_2 + t_2^2\right) + 4\pi^2 t_1^2 t_2^2\right]\cos\left(\frac{2\pi X}{L}\right)\right.\right.\\
&\left.\left. + L\left[L^2(t_1 - t_2) - 4\pi^2 t_1^2 t_2\right]\sin\left(\frac{2\pi X}{L}\right)\right\} + 2\pi^2 L^2 (t_1 - t_2)^2 + 8\pi^4 t_1^2 t_2^2\right)^2\\
&\times \left(L^4 + 2\pi\left\{\pi\left[L^2\left(-t_1^2 - 2t_1t_2 + t_2^2\right) + 4\pi^2 t_1^2 t_2^2\right]\cos\left(\frac{2\pi X}{L}\right)\right.\right.\\
&\left.\left. + L\left[L^2(t_2 - t_1) + 4\pi^2 t_1^2 t_2\right]\sin\left(\frac{2\pi X}{L}\right)\right\} + 2\pi^2 L^2 (t_1 - t_2)^2 + 8\pi^4 t_1^2 t_2^2\right)^2,\\
d^1_{Xt_1} &= \left(L^4 + 2\pi\left\{\pi\left[L^2\left(-t_1^2 - 2t_1t_2 + t_2^2\right) + 4\pi^2 t_1^2 t_2^2\right]\cos\left(\frac{2\pi X}{L}\right)\right.\right.\\
&\left.\left. + L\left[L^2(t_1 - t_2) - 4\pi^2 t_1^2 t_2\right]\sin\left(\frac{2\pi X}{L}\right)\right\} + 2\pi^2 L^2 (t_1 - t_2)^2 + 8\pi^4 t_1^2 t_2^2\right)\\
&\times \left(L^4 + 2\pi\left\{\pi\left[L^2\left(-t_1^2 - 2t_1t_2 + t_2^2\right) + 4\pi^2 t_1^2 t_2^2\right]\cos\left(\frac{2\pi X}{L}\right)\right.\right.\\
&\left.\left. + L\left[L^2(t_2 - t_1) + 4\pi^2 t_1^2 t_2\right]\sin\left(\frac{2\pi X}{L}\right)\right\} + 2\pi^2 L^2 (t_1 - t_2)^2 + 8\pi^4 t_1^2 t_2^2\right),
\end{aligned}
$$

$$
\begin{aligned}
d^2_{Xt_1} = &\left(L^4 + 2\pi\left\{\pi\left[L^2\left(-t_1^2 - 2t_1t_2 + t_2^2\right) + 4\pi^2 t_1^2 t_2^2\right]\cos\left(\frac{2\pi X}{L}\right)\right.\right.\\
&\left.\left. + L\left[L^2(t_1 - t_2) - 4\pi^2 t_1^2 t_2\right]\sin\left(\frac{2\pi X}{L}\right)\right\} + 2\pi^2 L^2 (t_1 - t_2)^2 + 8\pi^4 t_1^2 t_2^2\right)^2\\
&\times\left(L^4 + 2\pi\left\{\pi\left[L^2\left(-t_1^2 - 2t_1t_2 + t_2^2\right) + 4\pi^2 t_1^2 t_2^2\right]\cos\left(\frac{2\pi X}{L}\right)\right.\right.\\
&\left.\left. + L\left[L^2(t_2 - t_1) + 4\pi^2 t_1^2 t_2\right]\sin\left(\frac{2\pi X}{L}\right)\right\} + 2\pi^2 L^2 (t_1 - t_2)^2 + 8\pi^4 t_1^2 t_2^2\right)^2, \qquad \text{(E22)}
\end{aligned}
$$

$$
\begin{aligned}
d^{2,a}_{Xt_2} = &\left(L^4 + 2\pi\left\{\pi\left[L^2\left(-t_1^2 - 2t_1t_2 + t_2^2\right) + 4\pi^2 t_1^2 t_2^2\right]\cos\left(\frac{2\pi X}{L}\right)\right.\right.\\
&\left.\left. + L\left[L^2(t_2 - t_1) + 4\pi^2 t_1^2 t_2\right]\sin\left(\frac{2\pi X}{L}\right)\right\} + 2\pi^2 L^2 (t_1 - t_2)^2 + 8\pi^4 t_1^2 t_2^2\right)^2,\\
d^{2,b}_{Xt_2} = &\left(L^4 + 2\pi\left\{\pi\left[L^2\left(-t_1^2 - 2t_1t_2 + t_2^2\right) + 4\pi^2 t_1^2 t_2^2\right]\cos\left(\frac{2\pi X}{L}\right)\right.\right.\\
&\left.\left. + L\left[L^2(t_1 - t_2) - 4\pi^2 t_1^2 t_2\right]\sin\left(\frac{2\pi X}{L}\right)\right\} + 2\pi^2 L^2 (t_1 - t_2)^2 + 8\pi^4 t_1^2 t_2^2\right)^2,\\
d^1_{t_1t_2} = &\left\{L^4 + 2\pi^2\left[L^2\left(-t_1^2 - 2t_1t_2 + t_2^2\right) + 4\pi^2 t_1^2 t_2^2\right]\cos\left(\frac{2\pi X}{L}\right) - 2\pi L\left[L^2(t_2 - t_1) + 4\pi^2 t_1^2 t_2\right]\times\sin\left(\frac{2\pi X}{L}\right)\right.\\
&\left. + 2\pi^2 L^2 t_1^2 - 4\pi^2 L^2 t_1 t_2 + 2\pi^2 L^2 t_2^2 + 8\pi^4 t_1^2 t_2^2\right\}\left\{L^4 + 2\pi^2\left[L^2\left(-t_1^2 - 2t_1t_2 + t_2^2\right) + 4\pi^2 t_1^2 t_2^2\right]\cos\left(\frac{2\pi X}{L}\right)\right.\\
&\left. + 2\pi L\left[L^2(t_2 - t_1) + 4\pi^2 t_1^2 t_2\right]\sin\left(\frac{2\pi X}{L}\right) + 2\pi^2 L^2 t_1^2 - 4\pi^2 L^2 t_1 t_2 + 2\pi^2 L^2 t_2^2 + 8\pi^4 t_1^2 t_2^2\right\},\\
d^2_{t_1t_2} = &\,2\left(L^4 + 2\pi^2 (t_1 - t_2)^2 L^2 + 8\pi^4 t_1^2 t_2^2 + 2\pi\left\{\pi\left[\left(-t_1^2 - 2t_2t_1 + t_2^2\right)L^2 + 4\pi^2 t_1^2 t_2^2\right]\cos\left(\frac{2\pi X}{L}\right)\right.\right.\\
&\left.\left. + L\left[L^2(t_1 - t_2) - 4\pi^2 t_1^2 t_2\right]\sin\left(\frac{2\pi X}{L}\right)\right\}\right)^2\left(L^4 + 2\pi^2 (t_1 - t_2)^2 L^2 + 8\pi^4 t_1^2 t_2^2\right.\\
&\left. + 2\pi\left\{\pi\left[\left(-t_1^2 - 2t_2t_1 + t_2^2\right)L^2 + 4\pi^2 t_1^2 t_2^2\right]\cos\left(\frac{2\pi X}{L}\right) + L\left[(t_2 - t_1)L^2 + 4\pi^2 t_1^2 t_2\right]\sin\left(\frac{2\pi X}{L}\right)\right\}\right)^2\\
N_{t_1t_2} = &\,\frac{1}{L^2\pi^4}\left[N^{(0)}_{t_1t_2} + \cos\frac{2\pi X}{L}N^{(1)}_{t_1t_2} + \cos\frac{4\pi X}{L}N^{(2)}_{t_1t_2} + \cos\frac{6\pi X}{L}N^{(3)}_{t_1t_2} + \cos\frac{8\pi X}{L}N^{(4)}_{t_1t_2}\right],\\
N^{(0)}_{t_1t_2} = &\,L^{10} + 4\pi^2\left(t_1^2 + 2t_2^2\right)L^8 + \pi^4\left(5t_1^4 - 26t_2^2t_1^2 - 120t_2^3t_1 + 65t_2^4\right)L^6 + 4\pi^6 t_2^2\left(-3t_1^4 + 20t_2t_1^3 + 200t_2^2t_1^2 - 140t_2^3t_1 + 35t_2^4\right)L^4\\
&- 80\pi^8 t_1^2 t_2^4\left(t_1^2 + 28t_2t_1 - 14t_2^2\right)L^2 + 2240\pi^{10} t_1^4 t_2^6,\\
N^{(1)}_{t_1t_2} = &\,2\pi^2\left[-\left(t_1^2 - 7t_2^2\right)L^8 - 2\pi^2\left(t_1^4 + 4t_2^2t_1^2 + 52t_2^3t_1 - 27t_2^4\right)L^6 + 16\pi^4 t_2^3\left(2t_1^3 + 41t_2t_1^2 - 28t_2^2t_1 + 7t_2^3\right)L^4\right.\\
&\left. - 32\pi^6 t_1^2 t_2^4\left(t_1^2 + 56t_2t_1 - 28t_2^2\right)L^2 + 1792\pi^8 t_1^4 t_2^6\right],\\
N^{(2)}_{t_1t_2} = &\,-L^{10} - 4\pi^2\left(t_1^2 - 2t_2^2\right)L^8 - 4\pi^4\left(t_1^4 - 6t_2^2t_1^2 + 32t_2^3t_1 - 15t_2^4\right)L^6 + 16\pi^6 t_2^2\left(t_1^4 - 4t_2t_1^3 + 44t_2^2t_1^2 - 28t_2^3t_1 + 7t_2^4\right)L^4\\
&+ 64\pi^8 t_1^2 t_2^4\left(t_1^2 - 28t_2t_1 + 14t_2^2\right)L^2 + 1792\pi^{10} t_1^4 t_2^6,\\
N^{(3)}_{t_1t_2} = &\,2\pi^2\left[\left(t_1^2 + t_2^2\right)L^8 + 2\pi^2\left(t_1^4 + 4t_2^2t_1^2 - 12t_2^3t_1 + 5t_2^4\right)L^6 + 16\pi^4 t_2^3\left(-2t_1^3 + 7t_2t_1^2 - 4t_2^2t_1 + t_2^3\right)L^4\right.\\
&\left. + 32\pi^6 t_1^2 t_2^4\left(t_1^2 - 8t_2t_1 + 4t_2^2\right)L^2 + 256\pi^8 t_1^4 t_2^6\right],\\
N^{(4)}_{t_1t_2} = &\,\pi^4\left\{\left[\left(-t_1^2 - 2t_2t_1 + t_2^2\right)L^2 + 4\pi^2 t_1^2 t_2^2\right]\left[\left(t_1^2 - 2t_2t_1 + 3t_2^2\right)L^4 + 4\pi^2 t_2^2\left(2t_1^2 - 2t_2t_1 + t_2^2\right)L^2 + 16\pi^4 t_1^2 t_2^4\right]\right\}. \qquad \text{(E23)}
\end{aligned}
$$

[1] J. M. Deutsch, Quantum statistical mechanics in a closed system, Phys. Rev. A **43**, 2046 (1991).

[2] M. Srednicki, Chaos and quantum thermalization, Phys. Rev. E **50**, 888 (1994).

[3] M. Rigol, V. Dunjko, and M. Olshanii, Thermalization and its mechanism for generic isolated quantum systems, Nature (London) **452**, 854 (2008).

[4] A. Polkovnikov, K. Sengupta, A. Silva, and M. Vengalattore, Colloquium: Nonequilibrium dynamics of closed interacting quantum systems, Rev. Mod. Phys. **83**, 863 (2011).

[5] P. Calabrese and J. Cardy, Evolution of entanglement entropy in one-dimensional systems, J. Stat. Mech. (2005) P04010.

[6] K. A. Landsman, C. Figgatt, T. Schuster, N. M. Linke, B. Yoshida, N. Y. Yao, and C. Monroe, Verified quantum information scrambling, Nature (London) **567**, 61 (2019).

[7] M. K. Joshi, A. Elben, B. Vermersch, T. Brydges, C. Maier, P. Zoller, R. Blatt, and C. F. Roos, Quantum information scrambling in a trapped-ion quantum simulator with tunable range interactions, Phys. Rev. Lett. **124**, 240505 (2020).

[8] M. S. Blok, V. V. Ramasesh, T. Schuster, K. O'Brien, J. M. Kreikebaum, D. Dahlen, A. Morvan, B. Yoshida, N. Y. Yao, and I. Siddiqi, Quantum information scrambling on a superconducting qutrit processor, Phys. Rev. X **11**, 021010 (2021).

[9] B. Swingle, G. Bentsen, M. Schleier-Smith, and P. Hayden, Measuring the scrambling of quantum information, Phys. Rev. A **94**, 040302(R) (2016).

[10] G. Zhu, M. Hafezi, and T. Grover, Measurement of many-body chaos using a quantum clock, Phys. Rev. A **94**, 062329 (2016).

[11] N. Y. Yao, F. Grusdt, B. Swingle, M. D. Lukin, D. M. Stamper-Kurn, J. E. Moore, and E. A. Demler, Interferometric approach to probing fast scrambling, arXiv:1607.01801.

[12] N. Yunger Halpern, Jarzynski-like equality for the out-of-time-ordered correlator, Phys. Rev. A **95**, 012120 (2017).

[13] N. Yunger Halpern, B. Swingle, and J. Dressel, Quasiprobability behind the out-of-time-ordered correlator, Phys. Rev. A **97**, 042105 (2018).

[14] M. Campisi and J. Goold, Thermodynamics of quantum information scrambling, Phys. Rev. E **95**, 062127 (2017).

[15] B. Yoshida and A. Kitaev, Efficient decoding for the Hayden-Preskill protocol, arXiv:1710.03363.

[16] M. Gärttner, J. G. Bohnet, A. Safavi-Naini, M. L. Wall, J. J. Bollinger, and A. M. Rey, Measuring out-of-time-order correlations and multiple quantum spectra in a trapped-ion quantum magnet, Nat. Phys. **13**, 781 (2017).

[17] K. X. Wei, C. Ramanathan, and P. Cappellaro, Exploring localization in nuclear spin chains, Phys. Rev. Lett. **120**, 070501 (2018).

[18] J. Li, R. Fan, H. Wang, B. Ye, B. Zeng, H. Zhai, X. Peng, and J. Du, Measuring out-of-time-order correlators on a nuclear magnetic resonance quantum simulator, Phys. Rev. X **7**, 031011 (2017).

[19] E. J. Meier, J. Ang'ong'a, F. A. An, and B. Gadway, Exploring quantum signatures of chaos on a Floquet synthetic lattice, Phys. Rev. A **100**, 013623 (2019).

[20] P. Calabrese and J. Cardy, Quantum quenches in 1+1 dimensional conformal field theories, J. Stat. Mech. (2016) 064003.

[21] P. Calabrese and J. Cardy, Entanglement and correlation functions following a local quench: A conformal field theory approach, J. Stat. Mech. (2007) P10004.

[22] M. Nozaki, T. Numasawa, and T. Takayanagi, Holographic local quenches and entanglement density, J. High Energy Phys. 05 (2013) 080.

[23] J. Cardy, Thermalization and revivals after a quantum quench in conformal field theory, Phys. Rev. Lett. **112**, 220401 (2014).

[24] M. Nozaki, T. Numasawa, and T. Takayanagi, Quantum entanglement of local operators in conformal field theories, Phys. Rev. Lett. **112**, 111602 (2014).

[25] S. He, T. Numasawa, T. Takayanagi, and K. Watanabe, Quantum dimension as entanglement entropy in two dimensional conformal field theories, Phys. Rev. D **90**, 041701(R) (2014).

[26] P. Caputa, M. Nozaki, and T. Takayanagi, Entanglement of local operators in large-N conformal field theories, Prog. Theor. Expt. Phys. **2014**, 093B06 (2014).

[27] C. T. Asplund, A. Bernamonti, F. Galli, and T. Hartman, Holographic entanglement entropy from 2d CFT: Heavy states and local quenches, J. High Energy Phys. 02 (2015) 171.

[28] C. T. Asplund, A. Bernamonti, F. Galli, and T. Hartman, Entanglement scrambling in 2d conformal field theory, J. High Energy Phys. 09 (2015) 110.

[29] X. Wen and J.-Q. Wu, Quantum dynamics in sine-square deformed conformal field theory: Quench from uniform to nonuniform conformal field theory, Phys. Rev. B **97**, 184309 (2018).

[30] I. MacCormack, A. Liu, M. Nozaki, and S. Ryu, Holographic duals of inhomogeneous systems: The rainbow chain and the sine-square deformation model, J. Phys. A: Math. Theor. **52**, 505401 (2019).

[31] K. Goto, M. Nozaki, K. Tamaoka, M. T. Tan, and S. Ryu, Non-equilibrating a black hole with inhomogeneous quantum quench, arXiv:2112.14388.

[32] W. Berdanier, M. Kolodrubetz, R. Vasseur, and J. E. Moore, Floquet dynamics of boundary-driven systems at criticality, Phys. Rev. Lett. **118**, 260602 (2017).

[33] X. Wen and J.-Q. Wu, Floquet conformal field theory, arXiv:1805.00031.

[34] R. Fan, Y. Gu, A. Vishwanath, and X. Wen, Emergent spatial structure and entanglement localization in Floquet conformal field theory, Phys. Rev. X **10**, 031036 (2020).

[35] B. Han and X. Wen, Classification of SL_2 deformed Floquet conformal field theories, Phys. Rev. B **102**, 205125 (2020).

[36] X. Wen, R. Fan, A. Vishwanath, and Y. Gu, Periodically, quasiperiodically, and randomly driven conformal field theories, Phys. Rev. Res. **3**, 023044 (2021).

[37] R. Fan, Y. Gu, A. Vishwanath, and X. Wen, Floquet conformal field theories with generally deformed Hamiltonians, SciPost Phys. **10**, 049 (2021).

[38] X. Wen, Y. Gu, A. Vishwanath, and R. Fan, Periodically, quasiperiodically, and randomly driven conformal field theories (II): Furstenberg's theorem and exceptions to heating phases, SciPost Phys. **13**, 082 (2022).

[39] B. Lapierre and P. Moosavi, Geometric approach to inhomogeneous Floquet systems, Phys. Rev. B **103**, 224303 (2021).

[40] B. Lapierre, K. Choo, C. Tauber, A. Tiwari, T. Neupert, and R. Chitra, Emergent black hole dynamics in critical Floquet systems, Phys. Rev. Res. **2**, 023085 (2020).

[41] P. Moosavi, Inhomogeneous conformal field theory out of equilibrium, Ann. Henri Poincaré **25**, 1083 (2024).

[42] E. Langmann and P. Moosavi, Diffusive heat waves in random conformal field theory, Phys. Rev. Lett. **122**, 020201 (2019).

[43] J. Dubail, J.-M. Stéphan, and P. Calabrese, Emergence of curved light-cones in a class of inhomogeneous Luttinger liquids, SciPost Phys. **3**, 019 (2017).

[44] K. Gawędzki, E. Langmann, and P. Moosavi, Finite-time universality in nonequilibrium CFT, J. Stat. Phys. **172**, 353 (2018).

[45] J. Dubail, J.-M. Stéphan, J. Viti, and P. Calabrese, Conformal field theory for inhomogeneous one-dimensional quantum systems: The example of non-interacting Fermi gases, SciPost Phys. **2**, 002 (2017).

[46] M. P. Zaletel, A. M. Kaufman, D. M. Stamper-Kurn, and N. Y. Yao, Preparation of low entropy correlated many-body states via conformal cooling quenches, Phys. Rev. Lett. **126**, 103401 (2021).

[47] S. Roy, J. T. Chalker, I. V. Gornyi, and Y. Gefen, Measurement-induced steering of quantum systems, Phys. Rev. Res. **2**, 033347 (2020).

[48] T. Hartman and J. Maldacena, Time evolution of entanglement entropy from black hole interiors, J. High Energy Phys. 05 (2013) 014.

[49] K. Agarwal, R. N. Bhatt, and S. L. Sondhi, Fast preparation of critical ground states using superluminal fronts, Phys. Rev. Lett. **120**, 210604 (2018).

[50] P. Mitra, M. Ippoliti, R. N. Bhatt, S. L. Sondhi, and K. Agarwal, Cooling arbitrary near-critical systems using hyperbolic quenches, Phys. Rev. B **99**, 104308 (2019).

[51] X. Wen, R. Fan, and A. Vishwanath, Floquet's refrigerator: Conformal cooling in driven quantum critical systems, arXiv:2211.00040.

[52] We, however, note that the dynamics of mutual information was studied in [31]. Out-of-time-order correlators during the Floquet dynamics using Möbius Hamiltonians were also studied in [112].

[53] P. Hosur, X.-L. Qi, D. A. Roberts, and B. Yoshida, Chaos in quantum channels, J. High Energy Phys. 02 (2016) 004.

[54] L. Nie, M. Nozaki, S. Ryu, and M. T. Tan, Signature of quantum chaos in operator entanglement in 2d CFTs, J. Stat. Mech. (2019) 093107.

[55] P. Hayden and J. Preskill, Black holes as mirrors: Quantum information in random subsystems, J. High Energy Phys. 09 (2007) 120.

[56] Y. Nakata, E. Wakakuwa, and M. Koashi, Black holes as clouded mirrors: The Hayden-Preskill protocol with symmetry, Quantum **7**, 928 (2023).

[57] H. Tajima and K. Saito, Universal limitation of quantum information recovery: Symmetry versus coherence arXiv:2103.01876.

[58] T. Hikihara and T. Nishino, Connecting distant ends of one-dimensional critical systems by a sine-square deformation, Phys. Rev. B **83**, 060414(R) (2011).

[59] I. Maruyama, H. Katsura, and T. Hikihara, Sine-square deformation of free fermion systems in one and higher dimensions, Phys. Rev. B **84**, 165132 (2011).

[60] H. Katsura, Sine-square deformation of solvable spin chains and conformal field theories, J. Phys. A: Math. Theor. **45**, 115003 (2012).

[61] A. Gendiar, R. Krcmar, and T. Nishino, Spherical deformation for one-dimensional quantum systems, Prog. Theor. Phys. **122**, 953 (2009).

[62] A. Gendiar, M. Daniška, Y. Lee, and T. Nishino, Suppression of finite-size effects in one-dimensional correlated systems, Phys. Rev. A **83**, 052118 (2011).

[63] N. Shibata and C. Hotta, Boundary effects in the density-matrix renormalization group calculation, Phys. Rev. B **84**, 115116 (2011).

[64] H. Katsura, Exact ground state of the sine-square deformed XY spin chain, J. Phys. A: Math. Theor. **44**, 252001 (2011).

[65] C. Hotta and N. Shibata, Grand canonical finite-size numerical approaches: A route to measuring bulk properties in an applied field, Phys. Rev. B **86**, 041108(R) (2012).

[66] C. Hotta, S. Nishimoto, and N. Shibata, Grand canonical finite size numerical approaches in one and two dimensions: Real space energy renormalization and edge state generation, Phys. Rev. B **87**, 115128 (2013).

[67] N. Ishibashi and T. Tada, Infinite circumference limit of conformal field theory, J. Phys. A: Math. Theor. **48**, 315402 (2015).

[68] N. Ishibashi and T. Tada, Dipolar quantization and the infinite circumference limit of two-dimensional conformal field theories, Int. J. Mod. Phys. A **31**, 1650170 (2016).

[69] K. Okunishi, Sine-square deformation and Mobius quantization of two-dimensional conformal field theory, Prog. Theor. Exp. Phys. **2016**, 063A02 (2016).

[70] X. Wen, S. Ryu, and A. W. W. Ludwig, Evolution operators in conformal field theories and conformal mappings: Entanglement Hamiltonian, the sine-square deformation, and others, Phys. Rev. B **93**, 235119 (2016).

[71] S. Tamura and H. Katsura, Zero-energy states in conformal field theory with sine-square deformation, Prog. Theor. Exp. Phys. **2017**, 113A01 (2017).

[72] T. Tada, Conformal quantum mechanics and sine-square deformation, Prog. Theor. Exp. Phys. **2018**, 061B01 (2018).

[73] J. Maldacena and X.-L. Qi, Eternal traversable wormhole arXiv:1804.00491 [hep-th].

[74] W. Cottrell, B. Freivogel, D. M. Hofman, and S. F. Lokhande, How to build the thermofield double state, J. High Energy Phys. 02 (2019) 058.

[75] M. A. Nielsen and I. L. Chuang, *Quantum Computation and Quantum Information: 10th Anniversary Edition* (Cambridge University Press, Cambridge, 2010).

[76] The definition of dual state is not unique.

[77] J. Kudler-Flam, M. Nozaki, S. Ryu, and M. T. Tan, Quantum vs. classical information: Operator negativity as a probe of scrambling, J. High Energy Phys. 01 (2020) 031.

[78] J. Kudler-Flam, L. Nie, and S. Ryu, Conformal field theory and the web of quantum chaos diagnostics, J. High Energy Phys. 01 (2020) 175.

[79] J. Kudler-Flam, M. Nozaki, S. Ryu, and M. T. Tan, Entanglement of local operators and the butterfly effect, Phys. Rev. Res. **3**, 033182 (2021).

[80] E. Mascot, M. Nozaki, and M. Tezuka, Local operator entanglement in spin chains, SciPost Phys. Core **6**, 070 (2023).

[81] I. MacCormack, M. T. Tan, J. Kudler-Flam, and S. Ryu, Operator and entanglement growth in nonthermalizing systems: Many-body localization and the random singlet phase, Phys. Rev. B **104**, 214202 (2021).

[82] J. Kudler-Flam, R. Sohal, and L. Nie, Information scrambling with conservation laws, SciPost Phys. **12**, 117 (2022).

[83] K. Goto, A. Mollabashi, M. Nozaki, K. Tamaoka, and M. T. Tan, Information scrambling versus quantum revival through the lens of operator entanglement, J. High Energy Phys. 06 (2022) 100.

[84] P. Calabrese and J. Cardy, Entanglement entropy and quantum field theory, J. Stat. Mech. (2004) P06002.

[85] P. Calabrese and J. Cardy, Entanglement entropy and conformal field theory, J. Phys. A: Math. Theor. **42**, 504005 (2009).

[86] E. Witten, Anti-de Sitter space, thermal phase transition, and confinement in gauge theories, Adv. Theor. Math. Phys. **2**, 505 (1998).

[87] S. Ryu and T. Takayanagi, Aspects of holographic entanglement entropy, J. High Energy Phys. 08 (2006) 045.

[88] S. Ryu and T. Takayanagi, Holographic derivation of entanglement entropy from the anti–de Sitter space/conformal field theory correspondence, Phys. Rev. Lett. **96**, 181602 (2006).

[89] D. N. Page, Average entropy of a subsystem, Phys. Rev. Lett. **71**, 1291 (1993).

[90] S. Sen, Average entropy of a quantum subsystem, Phys. Rev. Lett. **77**, 1 (1996).

[91] M. Nozaki, Notes on quantum entanglement of local operators, J. High Energy Phys. 10 (2014) 147.

[92] C. Jonay, D. A. Huse, and A. Nahum, Coarse-grained dynamics of operator and state entanglement, arXiv:1803.00089.

[93] A. Nahum, J. Ruhman, S. Vijay, and J. Haah, Quantum entanglement growth under random unitary dynamics, Phys. Rev. X **7**, 031016 (2017).

[94] M. Mezei, Membrane theory of entanglement dynamics from holography, Phys. Rev. D **98**, 106025 (2018).

[95] T. Rakovszky, F. Pollmann, and C. W. von Keyserlingk, Diffusive hydrodynamics of out-of-time-ordered correlators with charge conservation, Phys. Rev. X **8**, 031058 (2018).

[96] C. W. von Keyserlingk, T. Rakovszky, F. Pollmann, and S. L. Sondhi, Operator hydrodynamics, OTOCs, and entanglement growth in systems without conservation laws, Phys. Rev. X **8**, 021013 (2018).

[97] We add an extra 2π factor in front of t. This comes from the 2π difference between H_{SSD} and the Poincaré Hamiltonian H_P (44).

[98] M. Bañados, Three-dimensional quantum geometry and black holes, AIP Conf. Proc. **484**, 147 (1999).

[99] M. M. Roberts, Time evolution of entanglement entropy from a pulse, J. High Energy Phys. 12 (2012) 027.

[100] C. J. Turner, A. A. Michailidis, D. A. Abanin, M. Serbyn, and Z. Papić, Quantum scarred eigenstates in a Rydberg atom chain: Entanglement, breakdown of thermalization, and stability to perturbations, Phys. Rev. B **98**, 155134 (2018).

[101] S. Moudgalya, N. Regnault, and B. A. Bernevig, Entanglement of exact excited states of Affleck-Kennedy-Lieb-Tasaki models: Exact results, many-body scars, and violation of the strong eigenstate thermalization hypothesis, Phys. Rev. B **98**, 235156 (2018).

[102] C.-J. Lin and O. I. Motrunich, Exact quantum many-body scar states in the Rydberg-blockaded atom chain, Phys. Rev. Lett. **122**, 173401 (2019).

[103] W. W. Ho, S. Choi, H. Pichler, and M. D. Lukin, Periodic orbits, entanglement and quantum many-body scars in constrained models: Matrix product state approach, Phys. Rev. Lett. **122**, 040603 (2019).

[104] C. J. Turner, A. A. Michailidis, D. A. Abanin, M. Serbyn, Papić, and Z., Weak ergodicity breaking from quantum many-body scars, Nat. Phys. **14**, 745 (2018).

[105] Z. Papić, Weak ergodicity breaking through the lens of quantum entanglement, in Entanglement in Spin Chains: From Theory to Quantum Technology Applications (Springer, New York, 2021).

[106] M. Dodelson and A. Zhiboedov, Gravitational orbits, double-twist mirage, and many-body scars, J. High Energy Phys. 12 (2022) 163.

[107] P. Caputa and D. Ge, Entanglement and geometry from subalgebras of the Virasoro algebra, J. High Energy Phys. 06 (2023) 159.

[108] D. Liska, V. Gritsev, W. Vleeshouwers, and J. Minář, Holographic quantum scars, SciPost Phys. **15**, 106 (2023).

[109] C. P. Herzog and T. Nishioka, Entanglement entropy of a massive fermion on a torus, J. High Energy Phys. 03 (2013) 077.

[110] C. F. Clement and A. M. Lane, Solutions of the continuity equation, Proc. R. Soc. London A **364**, 107 (1978).

[111] As mentioned in [31], the quasiparticle prediction for the operator entanglement entropy deviates away from the 2d free fermion CFT when the entanglement entropy is small, such as in the case where the entanglement entropy approaches the vacuum value.

[112] S. Das, B. Ezhuthachan, A. Kundu, S. Porey, B. Roy, and K. Sengupta, Out-of-time-order correlators in driven conformal field theories, J. High Energy Phys. 08 (2022) 221.